INFORMATION TO USERS

This manuscript has been reproduced from the microfilm master. UMI films the text directly from the original or copy submitted. Thus, some thesis and dissertation copies are in typewriter face, while others may be from any type of computer printer.

The quality of this reproduction is dependent upon the quality of the copy submitted. Broken or indistinct print, colored or poor quality illustrations and photographs, print bleedthrough, substandard margins, and improper alignment can adversely affect reproduction.

In the unlikely event that the author did not send UMI a complete manuscript and there are missing pages, these will be noted. Also, if unauthorized copyright material had to be removed, a note will indicate the deletion.

Oversize materials (e.g., maps, drawings, charts) are reproduced by sectioning the original, beginning at the upper left-hand corner and continuing from left to right in equal sections with small overlaps. Each original is also photographed in one exposure and is included in reduced form at the back of the book.

Photographs included in the original manuscript have been reproduced xerographically in this copy. Higher quality 6" x 9" black and white photographic prints are available for any photographs or illustrations appearing in this copy for an additional charge. Contact UMI directly to order.

UMI

University Microfilms International
A Bell & Howell Information Company
300 North Zeeb Road, Ann Arbor, MI 48106-1346 USA
313/761-4700 800/521-0600

Order Number 9426559

Dissociation, relaxation, and oxidation of highly vibrationally excited gas-phase metal carbonyl and cluster anions

Cooper, Brian Thomas, Ph.D.

The University of Arizona, 1994

U·M·I
300 N. Zeeb Rd.
Ann Arbor, MI 48106

DISSOCIATION, RELAXATION, AND OXIDATION OF HIGHLY VIBRATIONALLY EXCITED GAS-PHASE METAL CARBONYL AND CLUSTER ANIONS

by

Brian Thomas Cooper

A Dissertation Submitted to the Faculty of the

DEPARTMENT OF CHEMISTRY

In Partial Fulfillment of the Requirements
For the Degree of

DOCTOR OF PHILOSOPHY

In the Graduate College

THE UNIVERSITY OF ARIZONA

1994

THE UNIVERSITY OF ARIZONA
GRADUATE COLLEGE

As members of the Final Examination Committee, we certify that we have read the dissertation prepared by Brian Thomas Cooper entitled Dissociation, Relaxation, and Oxidation of Highly Vibrationally Excited Gas-Phase Metal Carbonyl and Cluster Anions and recommend that it be accepted as fulfilling the dissertation requirement for the Degree of Doctor of Philosophy

	1 Feb 94 Date
	6 Jan 94 Date
	1-6-94 Date
	6 Jan 94 Date
	6 JAN 94 Date

Final approval and acceptance of this dissertation is contingent upon the candidate's submission of the final copy of the dissertation to the Graduate College.

I hereby certify that I have read this dissertation prepared under my direction and recommend that it be accepted as fulfilling the dissertation requirement.

Dissertation Director	1 Feb 94 Date

STATEMENT BY AUTHOR

This dissertation has been submitted in partial fulfillment of requirements for an advanced degree at the University of Arizona and is deposited in the University Library to be made available to users under rules of the Library.

Brief quotations from this dissertation are allowable without special permission, provided that accurate acknowledgment of source is made. Requests for permission for extended quotation from any reproduction of this manuscript in whole or in part may be granted by the head of the major department or the Dean of the Graduate College when in his or her judgement the proposed use of the material is in the interests of scholarship. In all other instances, however, permission must be obtained from the author.

SIGNED: Brian Cooper

ACKNOWLEDGMENTS

A single page is a hopelessly inadequate space to express my gratitude to all the people who were by far the richest part of my graduate experience. I have been blessed with excellent teachers: my Father sparked my interest in chemistry with his practical knowledge as a chemical engineer; Mr. Ronald Pallack, twice my high school chemistry teacher, solidified this interest into a career goal; Prof. Dale Margerum, my undergraduate research advisor, taught me the essentials of scientific research; and Dr. Steve Buckner, my graduate advisor, immeasurable broadened my perspective of chemistry with his unique combination of knowledge, perception, and intellectual adventurousness. On the practical side of my graduate education, I thank Charlie Amling in the glass shop, Bob Smith in the machine shop, and Larry Cook and especially Ted Weigt in the electronics shop. It is no exaggeration that I have learned more from Ted than from any other single person at Arizona save my advisor. Last, no acknowledgment of my teachers would be complete if I did not also recognize those I have had the pleasure of teaching myself: my students.

Next, I thank my family for all their love and support. I enjoyed being within an easy drive of my Grandma, and I will miss her. My Dad has been very supportive of my education, and I particularly cherish the time we spent together in the mountains and canyons of this beautiful state. I am looking forward to being geographically and personally closer to my siblings Sean, Heather, and Darren; four and a half years is too long a time to be apart! Finally, I especially enjoyed the two months I lived in Virginia with my Aunt Andrea and my cousin Michael, and I had fun hosting Michael during his visit to Arizona.

I already miss my coworkers Steve VanOrden and Marshall Pope. Steve and I taught, worked, and listened to loud music together, and he also reintroduced me to FORTRAN and in general taught me a lot about computers. Marshall not only has a wealth of practical skills (and tools) and a truly creative approach to problems, but he always manages to challenge my conventional perceptions of both science and life. Both of them share my taste for dark beer and good pizza! I also enjoyed working with, teaching with, and telling lawyer jokes to Kimber Wilson, and I wish her the best of luck in her law career. I was also happy to work (and hike) with Larson Lindholm, and I hope he has a rewarding undergraduate research experience.

At the Naval Research Laboratory last winter I was fortunate to work with Drs. Denise Parent and Steve McElvany, and I remain grateful for the opportunity they and Drs. John Callahan and Mark Ross gave me to enhance my career. At Arizona, I owe gratitude to my committee; Profs. Jeanne Pemberton, Mike Burke, Mark Smith, and Ron Salzman have been very supportive. Special thanks are also due to Dr. Scott Saavedra, without whose encouragement I would not have pursued my current postdoctoral goals. I look forward to continued interaction with all of these scientists. Of course, Dr. Steve Buckner has had the largest impact of anyone on my professional development; I will always value his perspective and advice, and I aspire to emulate many aspects of his style as an advisor.

Finally, and most importantly, I thank my fiancé Jeanette Pon ("Jai") for her patience, love, and support, and especially for her persistence in teaching me about myself. I joyfully anticipate our life together!

To George F. Cooper

(20 February 1912 to 8 November 1982)

TABLE OF CONTENTS

TABLE OF CONTENTS — *Continued*

LIST OF FIGURES

LIST OF TABLES

ABSTRACT

Fourier transform ion cyclotron resonance mass spectrometry (FT-ICR) was used to study processes occurring in highly vibrationally excited metal-containing anions. The low-pressure environment of the FT-ICR trapping cell is optimal for the intentional study of nonthermal species. Vibrationally excited anions were prepared with well-defined excess internal energies by the absorption of a single 1064 nm photon into any species requiring the absorption of two such photons to dissociate.

The effects of vibrational excitation on the oxidation reactions of $Cr(CO)_5^-$, Al_{16}^-, and Al_{18}^- were systematically investigated. All three reactions slowed down with increasing anion vibrational energy, due to the large increase in the back-dissociation rate constants with excess internal energy. The branching fractions for the oxidation of $Cr(CO)_5^-$ and Al_{16}^- also were substantially altered by excess vibrational energy. These data, along with the translationally-excited data of other workers, were used to gain insight into the mechanisms of these quite different oxidation reactions.

Radiative relaxation rate constants were also measured for $Cr(CO)_5^-$ and Al_{16}^- using the oxidation branching ratio as an ion thermometric probe. A complementary value was determined for $Cr(CO)_5^-$ with a two-pulse photodissociation experiment, and showed that the radiative relaxation rate constant for this ion is strongly energy dependent. Also, radiative relaxation of $Cr(CO)_5^-$ is about an order of magnitude faster than Al_{16}^-. All these observations were attributed to the presence of high-frequency CO stretching modes in $Cr(CO)_5^-$, and a detailed model was developed to support this interpretation.

Finally, the photodissociation and photodetachment behavior of the $M_2(CO)_n^-$ (where M = Cr, Mn, Fe, and Co; and $4 \leq n \leq 9$, depending on the metal) and Al_n^- (n = 3 to 23) was investigated at 1064 nm and, for the dinuclear complexes, from 575 to 630 nm. Apparent metal atom loss from highly coordinatively unsaturated dinuclear carbonyl anions was instead ascribed to electron detachment and subsequent scavenging by the neutral metal carbonyl background.

CHAPTER 1:

INTRODUCTION

Perhaps the most frequently-cited motivation for the study of gas-phase chemistry is to indirectly elucidate the effects of solvent molecules on the structure, physical properties, and chemical reactivity of a solute by studying the species in the absence of solvent.[1.1] An immediate and extremely important consequence of the relative isolation of gas-phase species is that any energy absorbed by or chemically evolved from these species is not promptly coupled into overall heating of the system, since there are no solvent molecules close to the excited species to effect collisional energy transfer. This is often an experimental inconvenience, since slow energy transfer rates can lead to conditions of disequilibrium between the various degrees of freedom of a system, so that the system may no longer be properly described by a temperature. On the other hand, gas-phase investigations allow the study of energetic processes that cannot be observed in condensed media, including all of the experiments in this Dissertation.

Of course, the primary motivation for the study of gas-phase ions is that they are easily manipulated in a mass spectrometer and may be detected with extremely high efficiency. Mass spectrometric techniques may be classified loosely into beam, trapping, and high pressure "swarm" methods, listed in descending order of the characteristic "energy regime" of each technique. Mass spectrometry invariably involves the study of high-energy species. For example a "mass spectrum" of an organic molecule is determined by the fragmentation mechanisms available to the molecule after it has been ionized by a

moderately high-energy electron.[1.2] The excess internal energy in the nascent molecular ion causes the species to fragment, with the relative intensities of the fragment ions depending on the relative rate constants for each dissociation channel available at the internal energy of the excited species. Even in a swarm instrument, which is expressly designed for higher pressures than most mass spectrometers so it can be used to study thermal ion-molecule reactions, it is impossible to entirely exclude the effects of excess internal energy. On the other end of the energetic scale, tandem sector instruments operate with beam energies in the tens of keV range so that high-energy collisional activation may be used to gain additional structural and mechanistic information about the ions in the beam.[1.3] Also, since an electric sector is actually a kinetic energy (and not a mass) analyzer, these instruments are also used to study translational energy distributions of metastable ion fragmentation.

Mass spectrometric techniques may also be classified by the time scale of the experiment, and it is here that trapping techniques find their primary advantage: ion trapping times may often be arbitrarily long. This allows, for example, the study of near-threshold dissociation reactions that would be far too slow to occur within the ion residence time in even a swarm instrument.[1.4] In a sector machine, the excess internal energy that must be supplied to an activated polyatomic ion to ensure that it has dissociated by the time it reaches the detector (the so-called "kinetic shift") can be quite large—as high as 2 eV.[1.5]

One common criticism of Fourier transform ion cyclotron resonance mass spectrometry (or FT-ICR, the mass spectrometric technique used in this Dissertation), is that the low-pressure conditions required for detection make it difficult or impossible to ensure that a trapped ion has been adequately thermalized.[1.6] (Also, in many instruments the (hot)

electron filament is sufficiently near the cell to raise the effective temperature of the cell by tens of degrees, so even if the ions are thermalized they are still "warm," at a temperature significantly higher than ambient.[1.7]) However, the long trapping times attainable in FT-ICR allow ions to be thermalized by an additional process, that of radiative relaxation. Spontaneous infrared emission is very inefficient and therefore only becomes important by default, at long trapping times in the absence of collisional quenching. This Dissertation reports measurements of radiative relaxation rate constants for two species, $Cr(CO)_5^-$ and Al_{16}^-.

The low-pressure environment of FT-ICR may also be exploited for the intentional study of highly excited species, besides the relaxation measurements mentioned above. For example, the study of the bimolecular reactions of internally excited species often allows additional mechanistic insight to be gained from changes in product branching ratios and overall reaction rates. This extra energetic information may even help decide between competing reaction mechanisms. FT-ICR may be used to study other phenomena that cannot readily be observed by other mass spectrometric techniques. Perhaps the best example of this is the photodissociation spectroscopy of trapped ions.[1.8] Dissociations attributable to very weak (or sequential multiphoton absorption[1.9]) often may be observed in FT-ICR simply by increasing the irradiation time (although radiative relaxation becomes important for weak sequential multiphoton absorption processes). Also, vibrationally-induced electron detachment, which in a beam instrument must be noted only as a decrease in the intensity of the transmitted beam, can be studied a little more directly by FT-ICR because the electrons remain trapped in the cell and may be scavenged and detected.[1.10] Specific cases

of vibrationally induced electron detachment were observed for some of the anions studied here. Indeed, this difficult-to-study process may be more common than previously believed.

Thus, it is seen that excess internal energy or incompletely thermalized ions are not always a detriment to the rigorous study of ion chemistry. The intentional addition of excess internal energy to molecular ions has been used throughout this Dissertation to study ion relaxation rates, ion dissociation and electron detachment, and the bimolecular reactivity of excited species. This Dissertation marks the first successful use of bimolecular reaction product branching ratios for the measurement of ion relaxation. Radiative relaxation rate constants have also been measured for the first time for a metal carbonyl species and for a metal cluster species, and the contrast between the observed relaxation rates is an excellent illustration of the nature of radiative relaxation in polyatomic species.

CHAPTER 2:

INSTRUMENTATION

All experiments in this Dissertation used Fourier transform ion cyclotron resonance mass spectrometry, abbreviated herein as FT-ICR and also known as FTMS.[2.1] This technique, although less than twenty years old, is established to the point that three separate manufacturers now offer commercial instruments supporting a wide variety of sample introduction techniques. Standard FT-ICR methods were used throughout this Dissertation research except where otherwise noted. Ion trapping and detection by FT-ICR are at first glance conceptually simple: ions formed along the central axis of the cell are confined radially by a static magnetic field and axially by a static electric field; the radial (cyclotron) motion of the ions (which has a frequency inversely proportional to mass) is excited with an r.f. pulse and the subsequent image current these ions induce on a pair of receive plates is amplified, digitized, and Fourier transformed to produce a mass spectrum. However, many details of the signal equations, including inherent nonlinearities and artifacts of the technique and various attempts to correct them, are still being worked out.[2.2] Some of these effects are discussed in more detail the Suspended Trapping Electron Ejection section of this Chapter; the rest of this subject is both irrelevant to the present work and impossibly broad for adequate coverage in this Dissertation. The interested reader is referred to several review articles on the subject.[2.3] However, it should be noted that perhaps the biggest challenge remaining for FT-ICR investigators is to understand and control space-charge effects and to overcome the dynamic range and accuracy limitations they impose on FT-ICR

measurements. Indeed, a large portion of the time spent in the laboratory during these investigations went toward establishing experimental conditions that kept the absolute number of ions trapped in the cell approximately constant, so that subtler kinetic effects could be observed and reproduced.

Most of the experiments discussed in this Dissertation were performed at the University of Arizona, and the UA instrument and all of its necessary modifications and special features are discussed in detail below. The aluminum cluster experiments, however, were performed in February and March of 1993 at the Naval Research Laboratory in Washington, D.C.. The important differences between the NRL instrument and the UA instrument are discussed in the final section of this Chapter.

University of Arizona FT-ICR Instrument

While several configurations of this instrument have been used in this laboratory, only one was used for all work in this Dissertation. The rectangular trapping cell is fashioned of 1/16th in. thick × 1.375 in. × 1.375 in. square oxygen-free high-conductivity (OFHC) copper trap plates held 2.75 in. apart by a Macor (machinable ceramic) frame. The orthogonal, 2.75 in. × 1.375 in. receive plates are also composed of 1/16th in. thick OFHC copper, but the excite "plates" are actually made of ~80% transmissive tungsten screen to allow the introduction of laser light into the cell for the study of ion photochemistry or for laser desorption-ionization. A one inch diameter flat mirror is mounted behind the back excite screen for the photochemical experiments to increase the laser light fluence through the cell.

The cell is attached to a flange containing all the necessary electrical feedthroughs and bolted onto an ultra-high vacuum chamber so that the cell is positioned directly between the pole faces of a 10 in. Varian electromagnet operating at 0.7 T. Laser light enters the front of the chamber through a 6 in. glass vacuum window. The chamber is pumped to a base pressure of $\sim 1\times10^{-9}$ Torr by an Alcatel Crystal 100 UHV diffusion pump backed by an Alcatel mechanical roughing pump; chamber pressure is measured at a nude ion gauge with a Granville-Phillips 271 gauge controller. A static pressure of any sufficiently volatile molecule may be maintained by admitting it into the chamber through any of three Varian variable leak valves. Ion-molecule calibration reactions indicate that the pressure in the cell is typically about five times lower than the pressure read on the gauge, after correction for

the relative gauge sensitivity of the measured gas. This is due to such instrumental factors as the system pumping speed and the relative position of the sample inlets, pressure gauge, ICR cell, and pump. Gasses may also be admitted to the vacuum chamber through a General Valve Series 9 pulsed valve controlled by a home-built circuit. While the transient pressure following a pulsed-valve event may be very high, allowing pulsed sample introduction or the acceleration of slow ion-molecule reactions, the chamber can be pumped back to just above its base pressure within as little as half a second, which is useful for preventing side reactions with the neutral precursor or for low-pressure, collision-free experiments. The inlet system is mechanically pumped and its pressure is monitored with a CVC thermocouple gauge.

Typical experimental parameters for the negative-ion experiments of this Dissertation include trapping potentials between -1 and -2.5 V, nominal electron beam energies under 4 eV, nominal electron beam currents of 0.5 to 5 μA, reagent pressures between 1×10^{-7} and 1×10^{-5} Torr, and ion thermalization times of at least half a second and often as long as two seconds. Broadband "chirp" excitation and broadband detection, typically at full instrumental bandwidth (2.67 MHz), were used for nearly all experiments. Most often, 16K data points were acquired, apodized with a symmetrical three-term Blackman-Harris function, zero-filled once, and magnitude-mode Fourier transformed. The mass resolving power obtained in this manner was usually sufficient for near-unit mass resolution in the spectral region of interest (up to about m/z 350). More data points were acquired when higher resolving power was needed; however, this was rarely the case for the metal carbonyls (Δm = 28 for carbonyl loss) and aluminum clusters (Δm = 27 for Al atom loss)

studied here. An effort was made to ensure that the excite parameters (amplitude and sweep rate) and ion number densities used placed the experiment in a reasonably linear regime and yielded well-behaved peak shapes.

Laser Photoexcitation Sources

Two different laser photoexcitation sources were available for these experiments: a pulsed Nd:YAG system (which can also be used for laser desorption) and a cw Ar^+-pumped dye laser system. Both systems are supported on a home-built optical table constructed of a large (8.5 ft. × 4 ft. × 0.75 in.) aluminum sheet floating on an eight-inch-deep layer of sand held in a sandbox resting on a concrete-block substructure. Mounting holes are drilled and tapped in the aluminum sheet wherever necessary. The optical layout used for these experiments is diagrammed in Figure 2.1, below. The dye laser system is simpler to interface with the FT-ICR experiment and is therefore discussed first.

Up to 1.5 W of tunable visible light was available from the Coherent dye laser system, which incorporates an Innova 70 argon ion laser (7 W all lines) pumping a CR-599 standing-wave dye laser using Rhodamine 6G, which lases from about 565 to 635 nm. Output power is measured with a Coherent power meter, and output wavelength and approximate frequency bandwidth are monitored by diverting roughly 10% of the beam into a Burleigh Wavemeter Jr. interferometer. A prism beam steering system is used to direct the light into the ICR cell; the beam is usually expanded to roughly the cell dimensions with a plano-concave lens. Light is prevented from reaching the cell during all but the photoexcitation event(s) with a Vincent and Associates Uniblitz shutter system, controlled by a user-settable +5 V trigger signal from the FTMS 2000 data station (TRIG4 was reserved for this purpose).

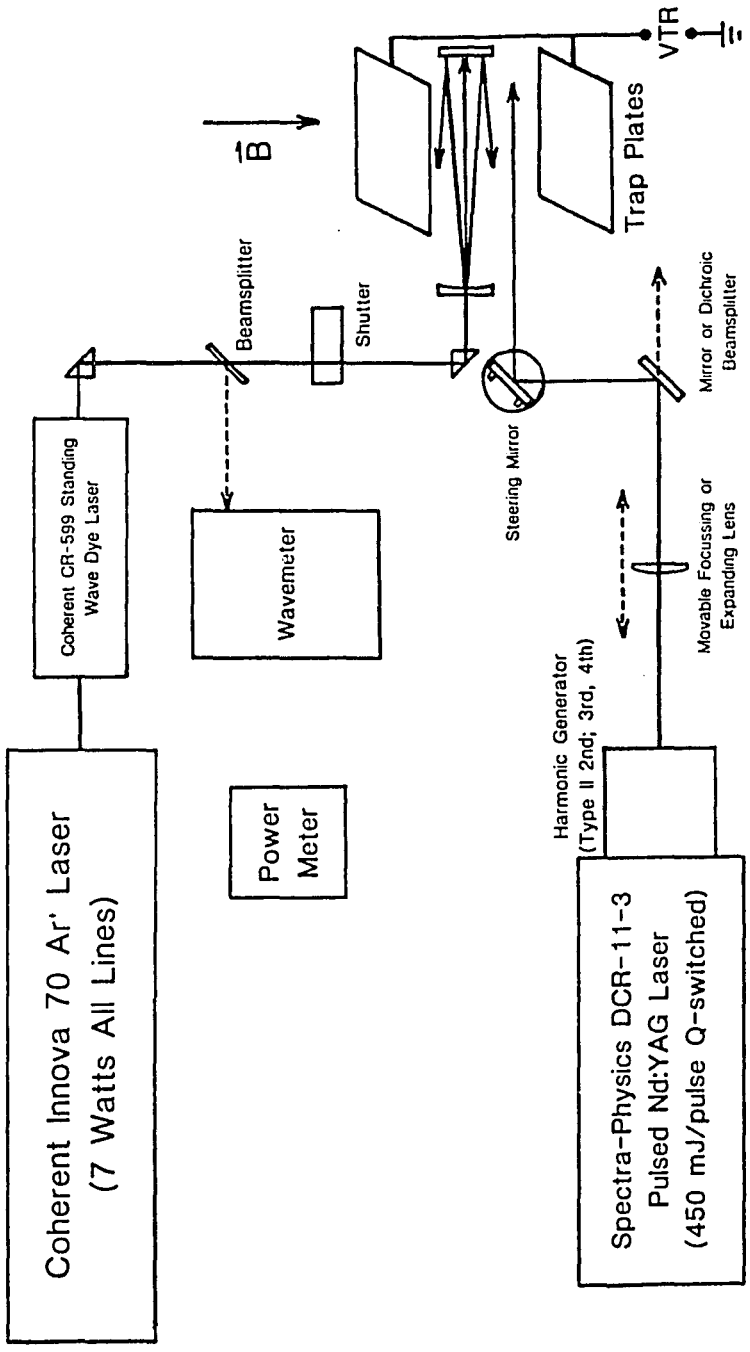

FIGURE 2.1: Optical Layout

A Spectra-Physics (Quanta-Ray) DCR-11 Nd:YAG laser with an attached harmonic generator was also available for photoexcitation or laser desorption experiments. The "Q-switched" mode is usually reserved for desorption experiments; 9 ns-wide pulses of up to 450 mJ may be obtained at 1064 nm (the fundamental); more than adequate pulse energy is still available at 532 nm (frequency-doubled) and 355 nm (tripled). The "long-pulse" mode is more desirable for most photoexcitation experiments. In this mode of operation the Q-switch is held open for the entire duration of the flashlamp pulse, spreading roughly 600 mJ of total output pulse energy (for 1064 nm output) over a 200 μs-long series of short but relatively weak pulses.

The Nd:YAG laser was considerably more difficult to interface to the data station. Since the laser is optimized to run at 10 Hz (at which rate lensing effects due to thermal expansion of the Nd:YAG rod are almost wholly corrected by the optics), and since the FTMS does not necessarily run at that or some integral fraction of that frequency, synchronizing the two can be difficult. Also, a laser pulse is usually not needed every 100 ms during a long experimental sequence, so control of both the laser's flash lamp and Q-switch are necessary. One option, running the laser "cold," can cause problems with pulse reproducibility. An indirect method of running the laser "in parallel" with the data station and synchronizing the laser output to the experimental sequence is described below. In this interface, diagrammed below in Figure 2.2.a, the computer is used solely as a "gate" for external control pulses.

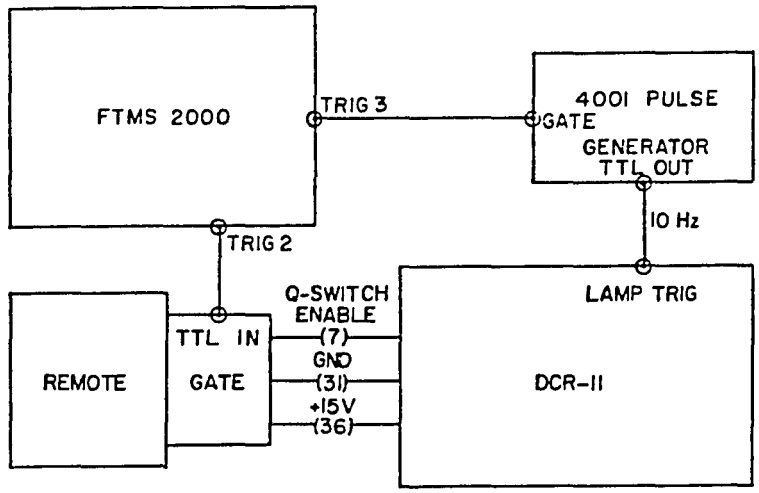

FIGURE 2.2.a: Block Diagram of Nd:YAG Laser/FT-ICR Interface

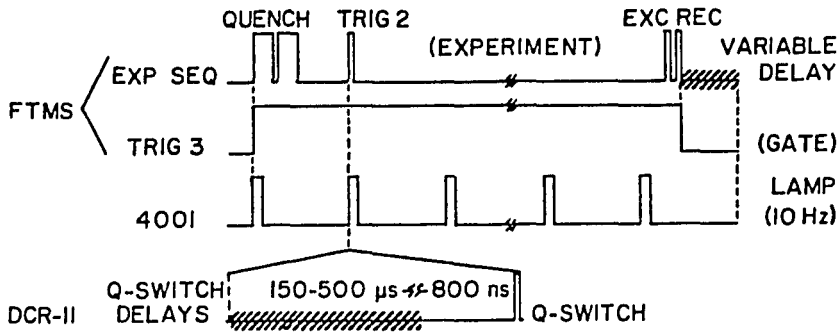

FIGURE 2.2.b: Nd:YAG Laser Synchronization Timing Diagram

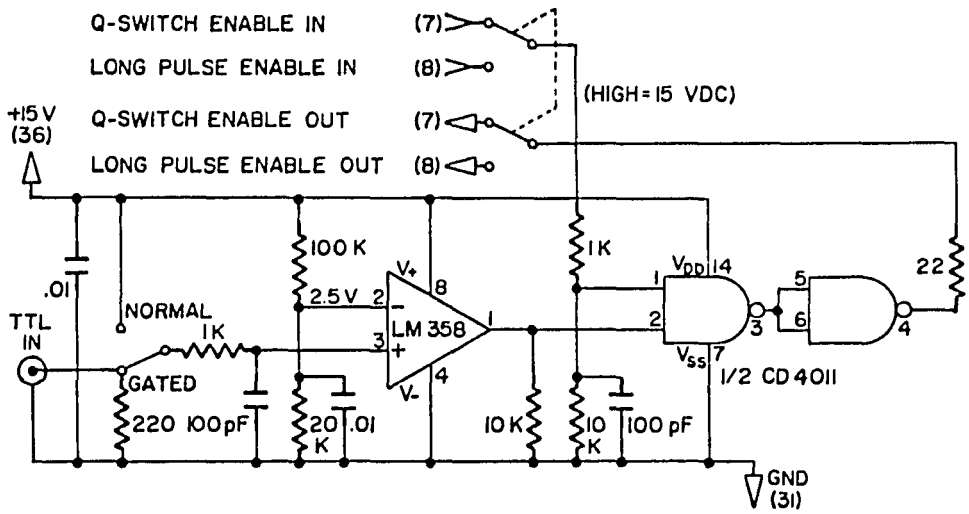

FIGURE 2.2.c: Nd:YAG Laser Interface (Enabling) Circuit

Briefly, an FTMS trigger pulse (TRIG3), left high from the beginning of the experimental sequence through the end of the receive event, is used to gate a 10 Hz pulse train from a commercial pulse generator (Global Specialties 4001) to the flash lamp trigger on the laser. The leading edge of the first flash lamp pulse is synchronized to the leading edge of the gate pulse, so that subsequent flash lamp pulses occur at every multiple of 100 ms during the experimental sequence. A variable delay is added to the experimental sequence after the receive event in order to round the total experiment time to the next integral multiple of 100 ms. The external pulse generator is turned off during this time so that the laser will have a tenth of a second to charge its flash lamp circuit, which the DCR-11 does automatically. (A laser that requires a separate external charge pulse would be somewhat more difficult to interface in this manner.) Since any additional setup time between sweeps (for graphics routines, etc.) is insignificant relative to the tenth of a second between pulses, and since the next lamp pulse comes at the very beginning of the next sweep, the flash lamp is in this manner operated with only a negligible hitch in its optimal 10 Hz pulse rate. A timing diagram for this interface is given above in Figure 2.2.b. An FTMS three-letter command was written to automatically compute the variable delay time; source code for this command is given at the end of this section.

Firing the flashlamp is a necessary but not sufficient condition for lasing to occur; in addition, the Q-switch must be *enabled* during the flashlamp pulse. Conversely, laser output will only be obtained if the flashlamp is fired during the time the laser is enabled. Once the flash lamp is synchronized to the experiment, laser output may be obtained from any desired flashlamp pulse by enabling the Q-switch for that pulse. Typically, a 5 ms-long

enable event (TRIG2) is used and the total time before this event is padded to just under the next integral multiple of 100 ms by adjusting the length of the preliminary "quench" events. TRIG2 turns on either the "Q-switch enable" (pin 7) or the "long-pulse enable" (pin 8) signal (+15 V) at a home-built circuit wired in between the laser's remote control and its main processing board. A diagram of this circuit is shown above in Figure 2.2.c. Note that it is critical to use an op-amp (or comparator) that can handle inputs near its supply voltages. The Q-switch delay is set on the laser itself; since the FTMS is used only to gate the Q-switch the relative timing of the data station to the laser is much less critical than it would be otherwise.

```
*   Source Code for the LSD (LaSer Delay) Command.

*   LSD.ASC  12 July 1990  SVO, BTC

*   Routine to compute a delay (RPD) to pad the total experimental
*   time to an integral multiple of 0.1 s.  This synchronizes the
*   experimental pulse sequence to the 10 Hz flashlamp pulse rate.

      COMMON /RPARAM/ RPA,RPB,RPC,RPD

      RPD = 0.0
      TIME = 0.0

      CALL FComNo('TIM',*999)
      CALL FCIReal('TIM',TIME,*999)

      RPD = 0.1-AMOD(TIME,0.1)
      PRINT *,'RPD=',RPD,'sec.'

  999 CALL EXIT
      END
```

Suspended Trapping Electron Ejection

One recurring problem in the study of gas phase negative ion chemistry by FT-ICR is trapped electrons.[2.4,2.5] Unlike ions, electron cyclotron motion cannot be detected since the inverse mass dependence of cyclotron frequency (Equation 2.1) guarantees for electrons typical resonant frequencies around 100 GHz—well beyond the bandwidth of the excitation and detection electronics. Typical cyclotron frequencies for ions are at least four to five orders of magnitude lower, as described approximately by

$$\omega_c \approx \frac{qB}{m} \tag{2.1}$$

in which m and q are the mass and charge of the particle in a uniform, static magnetic field of strength B. The inability of FT-ICR to excite electron cyclotron motion for the purpose of detection also necessarily precludes electron *ejection* by this means, which is the conventional method of mass-selected ion ejection from the trap.[2.6,2.7] However, the possibility of unattached electrons being present in a negative ion experiment cannot simply be ignored, as trapped electrons can severely impair the accuracy of the mass spectral measurement. Potentially deleterious manifestations of trapped electrons in such experiments include curvature in kinetic plots, the exacerbation of space charge effects such as coulombic line broadening[2.8] and peak shifting,[2.9] and the "reappearance" (by electron attachment to a background neutral) of an ejected peak.

In light of these difficulties, it is desirable in most negative ion experiments to ensure that no unattached electrons remain in the trap after the ionization period—a matter further

complicated by the lack of any direct method of electron detection. (Beauchamp[2.10] and Huntress and Simms[2.11] have directly detected electrons at their *trapping* frequency, but this technique has not found widespread use. The trapping motion will be discussed in detail below.) While any of the manifestations of trapped electrons mentioned above may in principle be used for indirect electron "detection," only peak reappearance, using an electron scavenger such as CCl_4[2.12] or SF_6,[2.13] is both experimentally convenient and easily quantifiable. Space charge effects are not selective for electrons and thus are not useful for electron quantitation, simply because the magnitude of these effects depends on the net charge contributed by all electrons and ions in the trap. Curvature in pseudo-first-order kinetic plots can occur if the rate of ion formation by trapped electron attachment to a background neutral is comparable to the rate of the ensuing ion-molecule reaction; concurrent formation and depletion of the reactant ion initially make the ion-molecule reaction appear slower. However, an ambiguity exists in the observation of a curved kinetic plot, since such curvature is also often observed in the exothermic reactions of incompletely thermalized reactant ions.[2.14] Also, even under ideal circumstances "detection" of trapped electrons by kinetic means is extremely tedious, and actual *quantitation* is even less direct. Of course, the simplest and best way to ensure that no electrons remain in the cell would be to deliberately eject them. Strategies for selective electron ejection can be understood from a brief discussion of trapped particle motion in the ICR cell.

Ideally, the motion of any charged particle in a static ICR trap can be analyzed into three fundamental periodic motions: cyclotron, magnetron, and trapping oscillations.[2.2,2.15] As discussed above, electron ejection by excitation of the cyclotron motion (rotation around

a magnetic field line) is not possible. The resonant frequency for magnetron motion (precession around an electric field line), while accessible for both electrons and ions, cannot be used for *selective* electron ejection since it is to a first approximation not mass dependent.[2.15,2.16] This leaves the trapping motion, an approximately harmonic (for cubic cells, at least)[2.17] oscillation of the particle along the *z*-axis (parallel to the magnetic field lines) in the electrostatic trapping well. Like all harmonic motions, the trapping frequency depends on the inverse square root of mass, as described by Equation 2.2:

$$\omega_T \approx \left(\frac{4q\alpha V_T}{ma^2} \right)^{1/2} \tag{2.2}$$

in which a is the edge length of the trap plates (which are assumed to be square and separated on the *z*-axis by a distance c), V_T is the applied trapping voltage (the excite and receive plates are held at ground), and α is a constant that depends on trap geometry (1.386 for a cubic trap and decreasing to 0.1856 as the aspect ratio c/a of the trap increases to 2, as was used here).[2.18,2.19] Typical trapping frequencies for electrons are in the range of a few MHz—accessible to a signal source of moderately high bandwidth. The inverse square root mass dependence easily separates electron trapping frequencies from typical ion trapping frequencies (by at least two orders of magnitude), so selective excitation is possible. Therefore, the usual method for ejecting electrons from the trap involves the temporary imposition onto the DC trapping potential of an r.f. signal tuned to ω_T and of sufficient amplitude and duration for *z*-axis ejection.[2.4,2.20-2.22] Alternately,[2.23] electrons have been ejected along the *z*-axis by applying an r.f. signal of twice the trapping frequency[2.23-2.25] to

the *excite* plates, taking advantage of the well known *z*-component of the differential r.f. excite field that is especially prominent in cells of low aspect ratio.[2.17,2.23-2.26]

The large frequency gap between electron and ion trapping oscillations suggests that only very *coarse* trapping frequency resolution is required for selective electron ejection. Indeed, all that is really needed is some sort of "high-pass mass filter" that rejects anything below some preset mass; this cutoff need not even be well determined. It will be shown here that a few-microsecond-long gated trapping event ("suspended trapping")[2.27,2.28] performs exactly this function, and is also simpler and more generally applicable to FT-ICR than resonant r.f. electron ejection.

In its original context, suspended trapping involves grounding the trap plates for some short period of time and then restoring the trapping field, at which point it is generally assumed that any ions (or electrons) still within the physical boundaries of the cell will remain trapped. With the trapping potential removed, and in the absence of collisions or excessive space charge repulsion, ions or electrons in the cell will move freely along the *z*-axis at the velocity with which they were travelling at the instant suspended trapping began. (Actually, trap-plate grounding is not quite instantaneous on the time scale of an electron trapping period, but this detail can be ignored in practice.) The *z*-axis velocity of a charged particle will depend on its mass, its instantaneous position in the (former) trapping well, and on its *z*-axis kinetic energy. Therefore, the time it takes an ion of a given mass and position to leave the cell during a suspended trapping event will depend on its kinetic energy. Indeed, outside of external source experiments, the first application of suspended trapping (called "ICR-time-of-flight")[2.29] was to measure photofragment kinetic energy distributions. *As*

named, "suspended trapping" was developed as a method of improved mass calibration[2.27] and dynamic range enhancement[2.28] by space charge reduction, especially when FT-ICR is used for accurate mass measurements in gas chromatography detection.

While the above discussion of suspended trapping relies on a time-domain description of the ion ejection criteria, suspended trapping can also be viewed as a "low-pass filter" in the frequency domain, with the "critical trapping frequency" for ion or electron ejection being roughly proportional to the inverse of the suspended trapping duration. Particles with a trapping frequency greater than the critical frequency will be ejected. The inverse square root mass dependence of trapping frequency also allows a *mass*-domain view of suspended trapping; all charged particles lighter than the mass corresponding to the critical trapping frequency will be ejected, forming a "high-pass mass filter."

It is instructive to contrast suspended trapping electron ejection to either of the resonant r.f. electron ejection techniques. Resonant ejection, whether with a signal at ω_T applied directly to the trap plates or with a $2\omega_T$ signal applied to the excite plates, requires that the electrons absorb enough energy from the r.f. excitation field to overcome the trapping potential and be ejected from the cell or collected on the trap plates. While the resolving power of both of these methods is rather low[2.21] and tuning the ejection oscillator is therefore relatively easy, strong signals may be required to effect complete electron ejection, especially for the inherently inefficient[2.23] $2\omega_T$ ejection technique. This problem becomes worse for elongated cells, since it has been shown[2.17] that even for a cell with an aspect ratio (c/a) of 1.5 the trapping potential is distinctly anharmonic and the trapping frequency depends strongly on the z-axis amplitude of the particle. In an elongated cell, an

electron that has been "gently" excited to a high *z*-amplitude, but remains trapped, will have moved out of resonance with the ejection signal tuned for the trapping frequency of an electron near the center of the trap. While resonant electron ejection is still possible in an elongated trap (Johlman and Wilkins[2.22] were able to eject electrons from a 3:1 aspect ratio trap using a 3 V peak-to-peak r.f. signal coupled to one of the -1.0 V trap plates for a few hundred microseconds), it is unclear to what extent the strong r.f. signals used perturb the motion of the ions in the cell. Certainly it is desirable to minimize the amplitude and duration of the ejection signal to reduce these effects. Proper tuning of the ejection signal helps; retuning is necessary with every significant change of the trapping voltage (although this problem can be avoided by assigning a fixed trapping voltage to the electron ejection event).

Unlike the other ejection techniques, suspended trapping does not require that the electrons absorb energy from a resonant r.f. field; instead it uses the intrinsic kinetic energy of the electrons and the *absence* of a trapping potential to allow the electrons to escape from the cell. Tuning the ejection oscillator is obviated, and the DC ejection amplitude used is ground or near ground (*vide infra*). Problems with anharmonicity in elongated cells are also avoided. As a pulsed technique, suspended trapping cannot be used for *continuous* electron ejection, but this is not a factor in most applications and, at any rate, continuous ejection with a low-level resonant r.f. signal is only reliable for square or other low-aspect-ratio cells. Finally, no external oscillator is required for suspended trapping; the inexpensive circuit described below is needed only to circumvent an unfortunate software limitation of this instrument.

Since the minimum event time allowed by the FTMS-2000 software is 100 μs, any suspended trapping event of shorter duration must be generated by external hardware edge-triggered by the data station. A simple electronic circuit, analogous to that used for surface-induced dissociation (SID) in FT-ICR,[2.30] was built to perform suspended trapping. Based on an analog multiplexer, this circuit switches the trap plates from their "normal" voltages (from the cell controller) to their "suspended trapping" voltages (from the external circuit), which can be ground or offset up to several volts from ground. The duration of the suspended trapping event can be set from 1-100 μs by varying the timing components of a monostable, which is itself triggered by the rising edge of a longer, +5 V pulse from the data station. A calibration table of output pulse length versus timing component settings was obtained using a pulse generator and an oscilloscope.

The effectiveness of suspended trapping electron ejection was tested with a simple peak reappearance experiment using $Cr(CO)_6$ as an electron scavenger. The ionization of $Cr(CO)_6$ (4×10^{-7} Torr) by dissociative electron attachment (Reaction 2.3, below) requires near-thermal electrons[2.31] and is therefore susceptible to problems with residual trapped electrons. (In fact, simple electron ejection experiments show that the majority of the signal obtained here arises from trapped electrons. The electron trapping process is facilitated by the elongated cell, as the longer electron flight path increases the probability of an inelastic electron scattering event occurring within the trapping well.) An appreciable fraction of the $Cr(CO)_5^-$ thus formed is photolyzed with a single YAG laser pulse to produce $Cr(CO)_4^-$ (Reaction 2.4). These reactions are discussed in more detail in Chapters 4 and 5.

$$e^- (\leq 2\ eV) + Cr(CO)_6 \longrightarrow Cr(CO)_5^- + CO \qquad (2.3)$$

$$Cr(CO)_5^- \xrightarrow{h\nu\ (1064\ nm)} \xrightarrow{h\nu\ (1064\ nm)} Cr(CO)_4^{-*} + CO \qquad (2.4)$$

The $Cr(CO)_5^-$ ions remaining after the photolysis step are selectively removed from the cell with an r.f. ejection pulse, and if electrons are to be ejected a suspended trapping event is added at this point as well. Any electrons remaining in the trap will eventually attach to the background $Cr(CO)_6$, causing the $Cr(CO)_5^-$ peak to reappear; sufficient time is allowed for complete attachment so that the trapped electrons can be quantitated as the $Cr(CO)_5^-$ peak intensity.

Spectra for the $Cr(CO)_4^-$ isolation, taken 100 ms after $Cr(CO)_5^-$ ejection, are shown below without electron ejection (Figure 2.3.a) and with electron ejection (Figure 2.3.b). A suspended trapping duration of 10 μs (corresponding to a trapping frequency cutoff of 100 kHz) was used. It was determined empirically that it is necessary to apply a small offset of about +0.25 V to the trap plates during the suspended trapping event to effect "complete" (>99%) electron ejection from the elongated cell. It is possible that part of this offset could represent a contact potential on the trap plates[2.27,2.28] (although the gold plating used here has been found[2.32] to prevent this); however, since a trapped electron can have nearly zero *z*-axis kinetic energy upon removal of the trapping field and would thus require a very long flight time to escape the cell, it is more probable that this offset simply represents the *accelerating* potential necessary to ensure that all electrons have left the cell by the end of the 10 μs suspended trapping period. According to a simple time-of-flight calculation (assuming the

electrons obey a Maxwell-Boltzmann velocity distribution with T_e = 350 K and ignoring space charge) a zero-offset suspended trapping event of about 40 μs is required for >99% of the electrons to have travelled at least half the distance between the trap plates. Two empirical observations support this hypothesis as well. First, if no offset is used about 90% of the electrons leave the trap during a 10 μs event, and the fraction of electrons ejected varies monotonically with suspended trapping duration. Second, the time required for complete ejection decreases as the offset potential increases, and vice versa, within reasonable limits of offset voltage and suspended trapping duration. It should also be pointed out that the use of an offset, by shortening the required ejection time, also reduces the probability of an electron-molecule collision during the electron's flight time. Of course, it is desirable to use the shortest event time and smallest offset potential possible in order to minimize any perturbation of the ions in the trap, as discussed above.

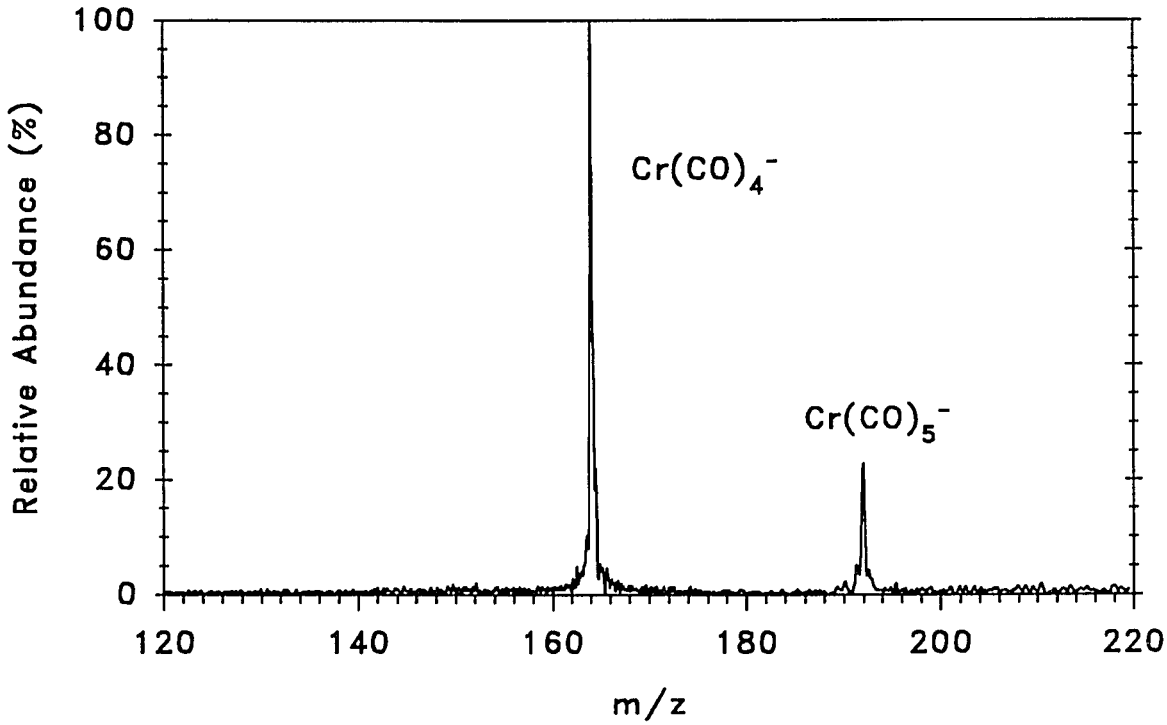

FIGURE 2.3.a: $Cr(CO)_4^-$ Isolation without Electron Ejection

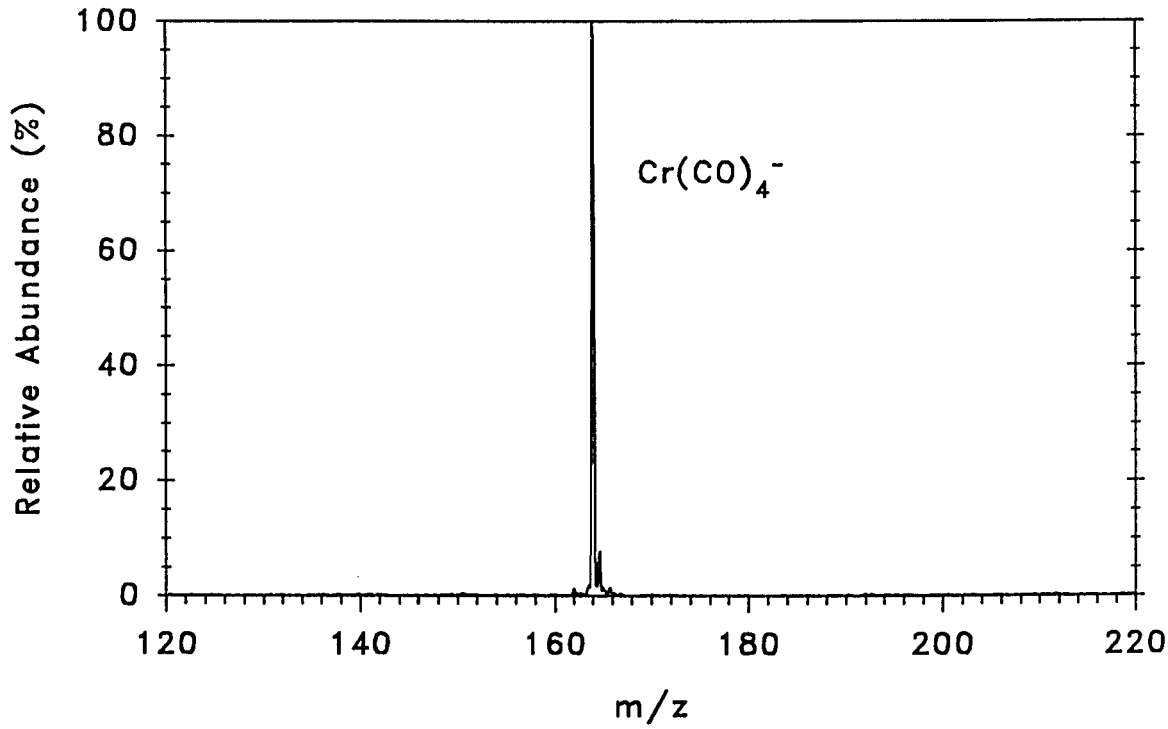

FIGURE 2.3.b: $Cr(CO)_4^-$ Isolation with Electron Ejection

Note that the parameters required for successful electron ejection by suspended trapping are *independent* of the normal trapping voltage, unlike with the resonant ejection techniques. This follows from two considerations. First, the ejection frequency for the resonant techniques varies with the square root of the trapping voltage, while the electron trapping frequency during the suspended trapping event is zero (no offset) or imaginary (positive offset), and the electrons need not absorb energy from a resonant field. Second, the suspended trapping duration and offset voltage are selected to ensure removal of those electrons with nearly zero *z*-axis kinetic energy (the most difficult to eject), which also implies that the effectiveness of this technique is not compromised by the presence of unthermalized electrons. (The maximum *z*-axis kinetic energy of an electron in the trap varies directly with the magnitude of the normal trapping voltage; the minimum—zero—does not.) On the other hand, the difficulty of ejecting a near-thermal electron with a resonant method varies directly with the depth of the trapping well, as the electron must absorb more energy to overcome the higher potential barrier. Electrons that begin with higher *z*-amplitude are somewhat off resonance and thus are still difficult to eject. Last, suspended trapping electron ejection can be made insensitive to the formation of contact potentials on the trap plates by allowing a small safety margin in the ejection parameters; the resonant ejection analogue to this is to use somewhat higher r.f. power than is minimally necessary.

Finally, it can be seen in this experiment that electron ejection has reduced the space charge in the cell; the $Cr(CO)_4^-$ peak intensity (area) in Figure 2.3.b is contained in a significantly more narrow peak than in Figure 2.3.a, and the signal-to-noise ratio has improved as a result. Also, while it is not discernable in the Figure, the $Cr(CO)_4^-$ peak in the

spectrum taken without electron ejection is shifted to ~80 Hz below that of the spectrum taken with electron ejection.

Suspended trapping electron ejection is used in Chapter 4 of this Dissertation to identify electron photodetachment processes for several dinuclear metal carbonyl anions. It is anticipated that the field of negative ion reaction chemistry will benefit from the ready applicability of this technique. Aside from photodetachment and kinetic measurements, suspended trapping electron ejection might also be used to minimize the formation of interfering reactant ions for low-pressure, negative-ion mass-selected chemical ionization.[2.33]

Naval Research Laboratory FT-ICR Instrument

The FT-ICR instrument at the Naval Research Laboratory was used for the aluminum cluster experiments discussed in Chapter 6. The most significant difference between the NRL and Arizona FT-ICR instruments is that a 3.0 T superconducting solenoid magnet is used at NRL. While in an electromagnet-based instrument light is admitted to the cell along the x- or y-axis (perpendicular to the magnetic field lines), for a superconducting magnet-based instrument light must be admitted along the z-axis (parallel to the magnetic field lines). The trap "plates" are made of metal screen to allow light into the cell. The superconducting geometry holds a major advantage over the electromagnet geometry for cluster formation by direct laser desorption, in that nascent desorbed ions are confined radially by the magnetic field into a relatively tight, axialized ion packet which better overlaps the desorbed plume of neutrals and thus enhances cluster formation.

The other significant difference between the Arizona and NRL instruments was the data station. The NRL instrument uses the newer, Sun workstation-based Extrel Odyssey system. While this computer and software are considerably more modern than the Extrel FTMS 2000 (based on the Nicolet 1280 computer, which uses a 20-bit word!) there are only two important differences in the capabilities of these instruments. First, the Odyssey software revision in use at the time did not allow the Nd:YAG laser (which is similar to but more powerful than the one at Arizona) to be completely synchronized to the experimental sequence. While it was possible to fire the laser at a known time within the sequence, it was not possible to prevent a "hitch" in the 10 Hz laser flashlamp firing rate at the end of each

sweep. This was because the time between sweeps was both unpredictable and occasionally very long—up to several seconds. This amply illustrates a major problem with using a multi-tasking, networked computer to control a real-time instrument. (In future revisions of the software it should be possible to allow the laser flashlamp to fire at its optimal 10 Hz rate and "strobe" (initiate) the experiment with the laser, so that the sequence starts on the next available flashlamp pulse after the computer indicates it is ready.) Since in some experiments both the 532 nm Q-switched output (for desorption) and the 1064 nm long-pulse output (for photoexcitation) were used in the same sequence, a simple electromechanical shutter, triggered by the data station, was used to stop the residual Q-switched 1064 nm beam during desorption events. The 532 nm beam was not shuttered since the energy in a 532 nm long pulse is insignificantly small.

The other important difference between the NRL and Arizona instruments is that the NRL instrument has SWIFT ("Stored-Waveform Inverse Fourier Transform")[2,34] excitation capabilities. SWIFT allows very precise, narrow-band excitations to be performed with minimal "leakage" of excitation power into neighboring masses. This proved to be critical for the aluminum cluster oxidation kinetics experiments since the reactive cross sections appear to be strongly sensitive to translational excitation.

CHAPTER 3:

VIBRATIONAL PROCESSES IN HIGHLY EXCITED ANIONS

Since all subsequent chapters of this Dissertation have in common the study of highly vibrationally excited anions, it will be instructive to discuss first in a general sense the various energetic processes available to such species. Each section of this Chapter concerns a different effect, defining it and outlining the circumstances under which it is important. The overall goal of this Chapter is to provide the reader with some framework for understanding or even predicting the fate of any excess internal energy found in a vibrationally excited polyatomic anion. The remaining chapters in this Dissertation provide several illustrative examples of the processes discussed here and will rely on this Chapter to unify the interpretation and discussion of the results.

One point of nomenclature should be clarified. Throughout this Dissertation the terms "molecule," "molecular (an)ion," "polyatomic (an)ion," and "(an)ion," will be used interchangeably. Practically, ions are studied because of the ease with which they may be manipulated in a mass spectrometer, as a consequence of having a net charge. However, this net charge does not alter the conclusions made in this Dissertation regarding the collisionless (radiative) relaxation of highly vibrationally excited species. Likewise, while the present Chapter is concerned only with polyatomic anions, the following discussion also applies to cations and neutrals, with one important exception: electron detachment (in this energy regime) can occur only for anions. Otherwise, the discussion in this Chapter is wholly general.

Internal Conversion

All vibrationally excited species investigated in this Dissertation were prepared photochemically, by the absorption of light. This technique has one very important advantage over other methods of imparting internal excitation to a molecule in that the amount of excess internal energy (which for a one-photon absorption equals the photon energy) is very well defined. The light sources used here range in photon energy from about 1.1 to 2.3 eV, which means that all absorptions are electronic in nature. In order to absorb a photon a molecule must possess a practicably strong electronic transition centered near the photon energy. This potentially limiting condition was only rarely restricting, as most of the metal-containing species investigated here have a high density of low-lying electronic states and therefore absorb quite broadly.

While absorption in this spectral region is strictly electronic, for a sufficiently large (several atoms or more) polyatomic molecule this electronic excitation ordinarily is promptly converted to vibrational energy. The "internal conversion" process occurs at an intersection between the excited electronic state and ground state potential surfaces (a "curve crossing"). The rate of this process depends on the nature of the curve crossing and is proportional to the density of vibrational states at the total molecular internal energy. This density of states can be calculated with the well-known Beyer-Swinehart state counting algorithm (see Appendix B), and increases very sharply with internal energy and with the number of vibrational modes. For example, at 1.5 eV of total internal energy, $Cr(CO)_5^-$ (11 atoms; 27 vibrational modes) may access nearly 10^{17} different vibrational microstates, increasing in

this energy region by roughly 10^{14} states per wavenumber. This internal energy corresponds to the average expected for a previously-thermal (at 300 K) $Cr(CO)_5^-$ ion that has absorbed one 1064 nm photon. While there is only one way (or at most, there are a few ways) to partition the excess internal energy into electronic states, there are for this example almost 10^{17} different ways to partition this energy vibrationally. Therefore, the equilibrium between electronic and vibrational excitation lies far to the vibrational side, and the reverse process is almost always unimportant. (A notable exception to this is vibrationally-induced electron detachment, which is discussed later in this Chapter.)

Internal conversion is extremely rapid, with a time scale (for a typical polyatomic ion) on the order of picoseconds. For this reason internal conversion is the dominant process available to electronically excited polyatomic ions; however, other possible fates for this excess internal energy need also be considered. The most important of these is (electronic) fluorescence, or re-emission of a visible photon of comparable to somewhat lower energy. Fluorescence only rarely competes with internal conversion since typical fluorescence lifetimes are in the tens of nanoseconds range—orders of magnitude slower. The conventional association of molecular rigidity with high fluorescence quantum yield is in fact a derived from density-of-states arguments; a "floppy" molecule contains more low-frequency vibrational modes and internal rotors and therefore internally converts more rapidly, preventing efficient fluorescence.

One final possibility, intersystem crossing to a long-lived isolated electronic state of different total spin, may also occur if both fluorescence and internal conversion are inefficient. This is rare for gas-phase polyatomics and will not be discussed further.

Dissociation and Predissociation

Any molecule that absorbs more energy than the strength of its weakest bond may dissociate. Conventionally, for photoinduced dissociation processes a distinction is made between *direct* dissociation and *pre*dissociation. A direct dissociation involves a $\sigma \rightarrow \sigma^*$ electronic transition that promptly cleaves the corresponding bond; the excited electronic state is not bound. Predissociation, on the other hand, is a two-step process involving a vibrationally excited intermediate. After absorption and internal conversion the molecule is only metastable (pseudo-bound); in the absence of any energy quenching process (see below) it will eventually dissociate. The rate of this dissociation depends strongly on both the size of the molecule and the amount of internal energy in excess of the dissociation threshold, since dissociation requires that sufficient energy be "in the right place at the right time." In other words, energy flows randomly (ergodically) throughout the various internal degrees of freedom of the molecule. Eventually, enough energy appears simultaneously in a dissociative degree of freedom and the molecule falls apart. The time scale for this process can range from nanoseconds for highly-excited, small molecules to hundreds of milliseconds for large molecules excited just above threshold. Such slow processes have actually been observed directly in the time domain by FT-ICR.[3.1]

Vibrationally-Induced Electron Detachment

Occasionally, the lowest bond dissociation energy of a molecular anion is comparable to or higher than the electron affinity of its corresponding neutral. It is therefore thermodynamically possible to detach the electron by vibrationally exciting the anion, either collisionally or by the absorption of one or more photons. Such a processes is not expected to occur for neutrals or cations because the required ionization energy is almost always much larger than the lowest bond dissociation energy. The following discussion of electron detachment from molecular anions will assume one-photon excitation so that an analogy may be invoked between photodetachment and the distinct photodissociation processes defined above.

One-photon electron detachment may occur by either of two mechanisms. In the "photoelectric" mechanism the absorbed photon excites the electron directly into a continuum of unbound electronic states. Using classical arguments (the optical frequency is much greater than the mechanical vibrational frequencies of the molecule), it is assumed that the molecular geometry does not change during the transition. The threshold detachment energy in this case is called the "vertical" electron affinity of the molecule, and any photon energy in excess of this vertical electron affinity goes into relative translation of the detached electron and the nascent neutral.

Analogous to the distinction between *pre-* and *direct* photodissociation, one-photon vibrationally-induced electron detachment is distinguished from the direct photoelectric detachment mechanism described above by the interposition of a vibrationally excited

intermediate. In fact, this process is occasionally referred to as "vibrational predissociation of an electron." Like its direct counterpart, vibrationally-induced detachment requires the pre-detaching anion to have absorbed energy in excess of the electron affinity of its corresponding neutral. In this mechanism, however, the absorbed photon excites the electron into a bound electronic state. Subsequent internal conversion leaves the anion in a highly vibrationally excited ground electronic state, which eventually detaches at a curve crossing between the anion and neutral potential surfaces. The geometry of the anion at the time of absorption and of the detaching transition state need not be the same; therefore, the amount of internal energy required to effect detachment by this mechanism is at least as great as the "adiabatic" electron affinity (the energy difference between the equilibrium geometries of the neutral and the anion) but is less than the vertical electron affinity of the photoelectric mechanism. This curve crossing is of course entirely inaccessible at anion internal energies below the adiabatic electron affinity of the neutral.

There are three practical (measurable) differences between direct and vibrationally-induced electron detachment that should be mentioned explicitly. First, the time scale for vibrational detachment may be much longer than that for direct detachment, for the same "dimensional" considerations discussed above for predissociation (sufficient energy must appear in the correct degree of freedom—out of many—within a short time). Second, the curve-crossing model for vibrationally-induced detachment predicts that low electron kinetic energies are strongly favored.[3.2] The detachment rate decreases for higher-energy electrons because the relevant nuclei must undergo a prohibitively large change in kinetic energy and momentum upon crossing to the neutral potential surface. This is in contrast to the direct

mechanism, in which the detached electrons may possess rather high kinetic energies. Finally, vibrationally-induced electron detachment should be spatially isotropic, whereas direct photoelectric detachment occurs only along the plane of polarization of the incident photon.

While the above discussion was intentionally limited to one-photon excitation, vibrationally-induced electron detachment has also been observed for other excitation processes. The original observation of this effect was for the infrared multiphoton excitation (using a CO_2 laser) of SF_6^- trapped in an ICR cell.[3.3] More recently, collisionally-induced electron detachment has been invoked to interpret transmission losses in the low-energy collision-induced dissociation (CID) of a number of mononuclear metal carbonyl anions in a triple-quadrupole mass spectrometer.[3.4] Sequential two-photon detachment (which is necessarily vibrational) was also observed for the 1064-nm excitation of the Al_6^- and Al_7^- cluster anions, and is discussed in Chapter 6. Finally, candidate observations of one-photon vibrationally-induced detachment from coordinatively unsaturated dinuclear metal carbonyl anions are described in Chapter 4. Indeed, the possibility of electron detachment is something that must always be considered in the study of highly-excited anions, especially for unusual species with unknown electron affinities.

Effects of Vibrational Excitation on Bimolecular Reactions

Both predissociation and vibrationally-induced electron detachment are examples of unimolecular reactions of highly vibrationally excited species, but often it is possible to prepare a highly vibrationally excited molecular ion that does not possess enough internal energy to dissociate or, if it is an anion, to detach. In this Dissertation, such species are prepared with well-defined excess internal energies by the absorption of a single photon into an anion that would require the absorption of two photons to dissociate. (See Appendix A for a detailed discussion of sequential two-photon processes, especially for a method of estimating the fraction of the ion population that has absorbed a single photon.) This excess internal energy may manifest itself by modulating the bimolecular reactivity of the excited ion. While such changes in reactivity are more profitably considered on a case-by-case basis, some useful generalizations can be made and will be discussed here.

The collision rate constants for all ion-molecule reactions studied in this Dissertation are given by the Langevin model:

$$k_L = 2\pi q \sqrt{\frac{\alpha}{\mu}} \tag{3.1}$$

in which k_L is the Langevin collision rate constant, q is the absolute ionic charge, α is the molecular polarizability, and μ is the reduced mass of the collision complex, all in *cgs* units (see the beginning of Chapter 7 for a brief discussion of the *cgs* system). Typical ion-molecule collision rates are two orders of magnitude higher than comparable neutral-neutral collision rates, due to the attraction between the ion and the dipole it induces in a polarizable

neutral. The Langevin model accounts for this increase in the collision rate and is valid for any molecule without a permanent dipole (which collide even faster).

Many bimolecular ion-molecule reactions can be successfully treated as unimolecular reactions once the ion-molecule collision complex has formed. It is therefore mandatory to understand the effects of vibrational excitation on unimolecular reactions. While all unimolecular rate constants increase as a function of internal energy, they do not necessarily increase with the same rate. Since the rate constant for a unimolecular reaction channel is proportional to the density of states at its transition state, the relative importance of a given channel depends on how rapidly its density of states increases with internal energy compared to the other accessible channels. The density of states for a "tight" (geometrically constrained) transition state does not increase as rapidly with internal energy as that of a "loose" (unconstrained) transition state, so the branching ratio between two such reactions shifts toward the loose channel at increasing internal energy. (Strictly speaking, a transition state is only considered "tight" if there is an accompanying decrease in the number of internal molecular rotors along that channel;[3,5] however, the terms "tight" and "loose" are often used in a relative sense and not just in the absolute sense of this strict definition.)

In general, there are two ways that vibrational excitation can manifest itself in a bimolecular reaction: by changing the overall reaction rate or by changing the branching behavior of the reaction (perhaps even opening a previously-inaccessible reaction channel). Branching behavior for a bimolecular ion-molecule reaction is governed by the same factors discussed above for unimolecular reactions. The efficiency of a bimolecular reaction is usually expressed as a fraction of the collision rate (or rate constant), and is equal to the sum

of the rate constants for all forward reactions out of the collision complex divided by the rate constant for back-dissociation out of the complex. This is simply a branching fraction, so the effects of internal energy on the overall reaction rate therefore can be understood on the same basis as unimolecular branching ratios. It is not unusual to see a ion-molecule reaction slow down with increasing ion internal energy, since the density of states for the (loose) back dissociation is typically quite large.

Collisional Quenching

The final two sections of this Chapter concern mechanisms for energy disposal from vibrationally excited species. The first of these, collisional quenching, is predominant at higher pressures and involves energy transfer between the excited species and anything it collides with. (Energy "disposal" and "removal" are used throughout this Dissertation; implicit in this terminology is the definition of the excited molecule as the "system" and its collision partners as part of the "surroundings.") The familiar macroscopic analogue to this process is heat transfer. It should at this point be emphasized that it is only for gas-phase species that the effects of vibrational excitation can be separately and explicitly considered. In condensed media, energy transfer between a nascent, internally converted species and its environment is extremely rapid because of the close proximity of the molecules; in other words, an irradiated condensed-phase system heats up.

A simple rate law can be written for collisional energy disposal:

$$-\frac{dE}{dt} = k_{coll}[M]\cdot E = ek_L[M]\cdot E \qquad (3.2)$$

In words, the rate dE/dt at which energy is collisionally removed from a vibrationally excited molecule is directly proportional to its (excess) internal energy E by a proportionality constant (a first-order rate constant) equal to the collisional quenching rate constant k_{coll} times the number density of the collision partner [M]. As mentioned above, Langevin collision theory is applicable to all ion-molecule collisions discussed in this Dissertation, so k_{coll} can in turn be written as the collisional quenching efficiency e times the Langevin

collision rate constant k_L. Note that Equation 3.2 assumes that the collisional quenching rate constant is independent of energy; it is more accurate to write it as $k_{coll}(E)$ or $e(E) \cdot k_L$.

Obviously, the rate constant for collisional quenching can be no greater than the collisional (in this case, Langevin) rate constant. There are two contributions to the potential decrease is quenching efficiency represented by the e factor in Equation 3.2. First, different collisions may remove different amounts of internal energy from the excited molecule. Second, it is possible that some collisions may not remove any energy at all. Therefore, e scales with the average amount of internal energy removed per collision. While a detailed discussion of the various mechanisms for collisional energy transfer is beyond the scope of this Dissertation (as is a discussion as to why the quenching rate might be proportional to the excess internal energy), these mechanisms can be classified by the type of energy taken up by the collision partner.[3.6] In general, vibrational-translational (V-T) and vibrational-rotational (V-R) energy transfer are far less efficient than vibrational-vibrational (V-V) energy transfer when the frequencies of the collision partner strongly overlap those of the energy-containing modes of the excited molecule. It is therefore expected that a polyatomic molecule such as SF_6 makes a much better collisional quenching partner than an atomic species such as Ar.

Radiative Relaxation

The final process that is available to a highly vibrationally excited polyatomic ion is radiative relaxation by sequential infrared fluorescence (as distinguished from the electronic fluorescence process discussed above). Radiative relaxation is discussed last because it is important only by default, under low-pressure, nearly collision-free conditions. A combined energy disposal rate law can be written that incorporates both collisional and radiative relaxation:[3.7]

$$-\frac{dE}{dt} = (k_{rad} + ek_L[M]) \cdot E \qquad (3.3)$$

Depending of course on relative magnitudes of e, k_L, and k_{rad}, radiative relaxation typically becomes significant for pressures below about 10^{-6} or 10^{-7} Torr. Again, it is more correct to write the radiative energy disposal rate constant as a function of internal energy: $k_{rad}(E)$. The circumstances under which this rate constant becomes independent of internal energy (so that the radiative energy disposal rate is directly proportional to internal energy) are discussed in detail in Chapter 7.

Three radiative rate constants were measured in this Dissertation: two for $Cr(CO)_5^-$ (Chapter 5) and one for Al_{16}^- (Chapter 6). The two $Cr(CO)_5^-$ radiative rate constants were measured with complementary techniques that give information about different energy regimes. All three radiative rate constants were measured with a maximum excess internal energy of about 1.1 eV, although the results for Al_{16}^- and one of the $Cr(CO)_5^-$ measurements

represent a broader, more averaged internal energy range. An exhaustively-detailed interpretation of these results is given in Chapter 7.

CHAPTER 4:

PHOTODISSOCIATION AND PHOTOINDUCED ELECTRON DETACHMENT IN DINUCLEAR METAL CARBONYL ANIONS

The photochemistry and reactivity of gas-phase metal carbonyl neutrals,[4.1] cations,[4.2] and anions[4.3,4.4] have been investigated extensively for their potential relevance to condensed-phase organometallic photochemistry,[4.5] catalysis,[4.6] and synthesis.[4.7] Among the most intriguing results of these studies have been the reports of neutral metal atom loss upon low-energy (roughly 1-20 eV center-of-mass) collisional activation of the highly coordinatively unsaturated dinuclear metal carbonyl anions $Cr_2(CO)_5^-$ and $Fe_2(CO)_4^-$.[4.3,4.8] This is a provocative observation because it suggests that these anions exist as completely asymmetrically coordinated dimers in which one of the metal atoms behaves like a ligand.

This Chapter reports on the visible (575-630 nm) and near-infrared (1064 nm) photochemistry of the dinuclear metal carbonyl anions $M_2(CO)_n^-$, where M = Cr, Mn, Fe, and Co; and $4 \leq n \leq 9$, depending on the metal. Nearly every species generated absorbs in the spectral regions studied. Both continuous ejection experiments and the dependence of the observed photoproduct signal on the laser fluence are used to establish whether a given process requires the absorption of a single photon or the sequential absorption of two photons. The absorption bands are typically broad and featureless (for example, see Figure 4.1, below), so it should not be concluded when only a single wavelength is shown for a photoactivated reaction that the observed behavior occurs only at that wavelength. Instead, the given wavelengths are those for which the photon dependence of each reaction was

explicitly determined. Absorption cross sections for these species range from 5×10^{-19} to 1×10^{-17} cm^2, and are speculatively but reasonably assigned as ligand field bands. The majority of these species photodissociate, losing one carbonyl ligand per photon absorbed; specific exceptions to this are discussed for each individual metal. The observed photodissociation behavior occasionally places both upper and lower limits on metal-carbonyl or metal-metal bond strengths. While these determinations are complicated by the broad (order of 10 kcal/mol wide) thermal internal energy distributions expected for these large polyatomic ions and the unknown ion internal temperatures, approximate limits are based on the average internal energy expected from estimated frequencies and a 325 K vibrational partition function. Bond strengths estimated in this manner are discussed only when they are novel.

Analogous to the previous collisional activation experiments mentioned above, apparent neutral metal atom loss is observed upon photoactivation of $Cr_2(CO)_5^-$, $Fe_2(CO)_4^-$, and also $Co_2(CO)_4^-$. However, electron ejection and scavenging experiments are used to establish that the "neutral metal atom loss" observed for these "terminal dinuclear anions" is attributable to photoinduced electron detachment followed by dissociative attachment to the neutral metal carbonyl background gas. Since the electron detachment process appears to be vibrationally driven, this study provides an alternative explanation for the previous collisional activation results.

$Cr_2(CO)_n^-$

As there is no stable neutral dichromium carbonyl precursor, the dinuclear chromium anions were formed by ion-molecule reactions, as summarized below. First, $Cr(CO)_5^-$ is generated by dissociative electron attachment to $Cr(CO)_6$, which is admitted to the reaction chamber through a pulsed valve:

$$e^- (\leq 2\ eV) + Cr(CO)_6 \longrightarrow Cr(CO)_5^- + CO \qquad (4.1)$$

The $Cr(CO)_6$ pressure wave reaches a peak of $\sim 5\times10^{-5}$ Torr and is largely pumped away within half a second of the pulsed valve opening. (However, residual $Cr(CO)_6$ remains in the chamber for at least several seconds, and can efficiently scavenge additional trapped electrons from any source.) Next, the $Cr(CO)_5^-$ is photolyzed with multiple 1064 nm laser pulses to produce $Cr(CO)_4^-$ and $Cr(CO)_3^-$, which are immediately reacted with a second pulsed-valve addition of $Cr(CO)_6$ to form a variety of dinuclear species:

$$Cr(CO)_5^- \xrightarrow{h\nu\ (1064\ nm)} \xrightarrow{h\nu\ (1064\ nm)} Cr(CO)_4^{-*} + CO \qquad (4.2)$$

$$Cr(CO)_4^{-*} \xrightarrow{h\nu\ (1064nm)} Cr(CO)_3^- + CO \qquad (4.3)$$

$$Cr(CO)_4^- \xrightarrow{h\nu\ (1064\ nm)} \xrightarrow{h\nu\ (1064\ nm)} Cr(CO)_3^- + CO \qquad (4.4)$$

$$Cr(CO)_4^- + Cr(CO)_6 \longrightarrow Cr_2(CO)_8^- + 2CO \quad (4.5.a)$$
$$\hookrightarrow Cr_2(CO)_9^- + CO \ (< 5\%) \quad (4.5.b)$$

$$Cr(CO)_3^- + Cr(CO)_6 \longrightarrow Cr_2(CO)_6^- + 3CO \quad (4.6.a)$$
$$\hookrightarrow Cr_2(CO)_7^- + 2CO \ (< 10\%) \quad (4.6.b)$$

The photolysis step (the nature of which is discussed in more detail in Chapter 5) is necessary because the 17-electron $Cr(CO)_5^-$ will not react with the background $Cr(CO)_6$.

Isolable quantities of the less-saturated dinuclear chromium species also may be produced by visible photolysis of $Cr_2(CO)_8^-$:

$$Cr_2(CO)_8^- \xrightarrow[-CO]{h\nu\ (590\ nm)} Cr_2(CO)_7^- \xrightarrow[-CO]{h\nu\ (590\ nm)} Cr_2(CO)_6^- \xrightarrow[-CO]{h\nu\ (590\ nm)} Cr_2(CO)_5^- \quad (4.7)$$

This is the preferred route to these species, since the yields are higher than with the more direct method of Equations 4.5 and 4.6. The $Cr_2(CO)_5^-$ species is called the "terminal dinuclear anion" because absorption of another visible photon causes apparent metal-atom loss:

$$Cr_2(CO)_5^- \xrightarrow{h\nu\ (590\ nm)} Cr(CO)_5^- + \text{"Cr"} \quad (4.8)$$

However, if a suspended trapping electron ejection event is applied immediately after the 590 nm laser irradiation step in Reaction 4.8, the mononuclear signal is substantially reduced, meaning that an electron detachment mechanism must be operative:

$$Cr_2(CO)_5^- \xrightarrow{h\nu\ (590\ nm)} Cr_2(CO)_5 + e^- \qquad (4.9)$$

$$e^-\ (trapped) + Cr(CO)_6 \longrightarrow Cr(CO)_5^- + CO \qquad (4.10)$$

Electron ejection never entirely eliminates the mononuclear signal, since electron attachment to the residual $Cr(CO)_6$ can occur *during* the laser and electron ejection events, which are therefore made as short as practical for these experiments. Thermal electron attachment to $Cr(CO)_6$ approaches unit efficiency.[4.9] Continuous ejection and laser fluence dependence experiments are used to verify that electron detachment occurs solely from $Cr_2(CO)_5^-$, which suggests a decrease in electron affinity with decreasing coordinative saturation for the homologous neutrals.

$Mn_2(CO)_n^-$

Unlike chromium, manganese and the rest of the metals discussed in this Chapter have stable neutral dinuclear precursors. Dinuclear species therefore may be produced directly (Reactions 4.11.c through 4.11.e, below):

$$e^- + Mn_2(CO)_{10}^- \longrightarrow Mn(CO)_5^- + Mn(CO)_5 \ (25\%\text{-}97\%) \quad (4.11.a)$$
$$\hookrightarrow Mn(CO)_4^- + CO + Mn(CO)_5 \quad (4.11.b)$$
$$\hookrightarrow Mn_2(CO)_9^- + CO \ (30\%\text{-}2\%) \quad (4.11.c)$$
$$\hookrightarrow Mn_2(CO)_8^- + 2CO \ (45\%\text{-}1\%) \quad (4.11.d)$$
$$\hookrightarrow Mn_2(CO)_7^- + 3CO \quad (4.11.e)$$

Dinuclear anion formation is favored only for near-thermal electrons and is very sensitive to the electron energy; the low-energy to high-energy branching percentages given above for Reactions 4.11.a, 4.11.c, and 4.11.d represent an ionizing electron energy span of only about 1 eV (nominal). The ease with which the Mn-Mn bond cleaves with just a slight excess of ionization energy reflects both its low (unity) bond order and the relative stability of the coordinatively saturated (18-electron) $Mn(CO)_5^-$ product. $Mn(CO)_4^-$ and $Mn_2(CO)_7^-$ are only minor products (< 0.5% each at all energies).

The following photodissociation behavior is observed for the dimanganese system:

$$Mn_2(CO)_9^- \xrightarrow[-CO]{h\nu\ (1064\ nm)} Mn_2(CO)_8^- \xrightarrow{h\nu\ (1064\ nm)} \xrightarrow[-CO]{h\nu\ (1064\ nm)} Mn_2(CO)_7^- \quad (4.12)$$

$$Mn_2(CO)_7^- \xrightarrow{h\nu\ (1064\ nm)} \xrightarrow{h\nu\ (1064\ nm)} Mn(CO)_5^- + Mn(CO)_2 \quad (4.13)$$

$$Mn_2(CO)_9^- \xrightarrow[-CO]{h\nu\ (610\ nm)} Mn_2(CO)_8^- \xrightarrow{h\nu\ (610,\ 580\ nm)} \xrightarrow{h\nu\ (610,\ 580\ nm)} Mn_2(CO)_7^- \quad (4.14)$$

$$\xrightarrow{h\nu\ (610,\ 580\ nm),\ -CO}$$

$$Mn_2(CO)_7^- \xrightarrow{h\nu\ (610,\ 580\ nm)} Mn(CO)_5^- + Mn(CO)_2 \quad (4.15)$$

Note that, unlike the other dinuclear systems discussed in this Chapter, no apparent metal-atom loss channel is observed. Instead, upon absorption of either one visible or two near-infrared photons, $Mn_2(CO)_7^-$ cleaves into $Mn(CO)_2$ and the stable, 18-electron $Mn(CO)_5^-$ species. The transition from two- to one-photon behavior with increasing photon energy places conservative limits on the metal-metal bond strength in this species: 40 kcal/mol $\leq$ D[$(CO)_2Mn$—$Mn(CO)_5^-$] $\leq$ 60 kcal/mol, assuming that an average, 325 K $Mn_2(CO)_7^-$ ion contains about 13 kcal/mol of internal energy. Although thermal broadening narrows these limits by a few kcal/mol on either side, the precise magnitude of this effect is not known. Unless this is a direct dissociation, the observed photodissociation behavior also implies that all Mn-CO bonds are stronger than the Mn-Mn bond.

$Fe_2(CO)_n^-$

Like manganese, iron exhibits a strongly energy-dependent competition between mono- and dinuclear anion formation from its neutral precursor:

$$e^- + Fe_2(CO)_9^- \longrightarrow Fe(CO)_4^- + Fe(CO)_5 \ (10\%\text{-}45\%) \quad (4.16.a)$$
$$\hookrightarrow Fe(CO)_3^- + CO + Fe(CO)_5 \quad (4.16.b)$$
$$\hookrightarrow Fe_2(CO)_7^- + 2CO \ (85\%\text{-}20\%) \quad (4.16.c)$$
$$\hookrightarrow Fe_2(CO)_6^- + 3CO \ (5\%\text{-}35\%) \quad (4.16.d)$$
$$\hookrightarrow Fe_2(CO)_5^- + 4CO \quad (4.16.e)$$

Again, dissociative electron attachment to form a dinuclear anion is more favored at low electron energies (the first of the two branching percentages given for reactions 4.16.a, 4.16.c and 4.16.d, which represent a range of about 1 eV in nominal electron energy). Reactions 4.16.b and 4.16.e only become important at still higher ionizing electron energies.

The following photodissociation reactions are observed for the dinuclear iron anions in the near infrared:

$$Fe_2(CO)_7^- \xrightarrow[-CO]{h\nu\ (1064\ nm)} Fe_2(CO)_6^- \xrightarrow[-CO]{h\nu\ (1064\ nm)} Fe_2(CO)_5^- \xrightarrow[-CO]{h\nu\ (1064\ nm)} Fe_2(CO)_4^- \quad (4.17)$$

$$Fe_2(CO)_4^- \xrightarrow{h\nu\ (1064\ nm)} Fe(CO)_4^- + \text{"Fe"} \quad (4.18)$$

Again, electron ejection experiments show that the apparent metal atom loss is due to electron detachment and subsequent scavenging by the static $Fe_2(CO)_9$ background. While it was difficult to isolate usable quantities of $Fe_2(CO)_4^-$ from $Fe_2(CO)_5^-$, if residual

$Fe_2(CO)_7^-$ and $Fe_2(CO)_6^-$ ions are carefully ejected they are seen to grow back in after laser irradiation of the $Fe_2(CO)_{5/4}^-$ mixture:

$$Fe_2(CO)_4^- \xrightarrow{h\nu\ (1064\ nm)} e^- + Fe_2(CO)_4 \qquad (4.19)$$

$$e^-\ (trapped) + Fe_2(CO)_9 \longrightarrow Fe(CO)_4^-\ (40\%) \qquad (4.20.a)$$
$$\hookrightarrow Fe(CO)_3^-\ (15\%) \qquad (4.20.b)$$
$$\hookrightarrow Fe_2(CO)_7^-\ (25\%) \qquad (4.20.c)$$
$$\hookrightarrow Fe_2(CO)_6^-\ (20\%) \qquad (4.20.d)$$

The observed dinuclear anion formation supports the electron ejection results.

Similar behavior is observed in the visible, except that one visible photon is sometimes sufficient to remove *two* carbonyls from $Fe_2(CO)_7^-$. The branching ratio for this process varies with the photon energy (as shown in Figure 4.1) suggesting that dissociation of at least the second photon (and likely both) proceeds through a vibrationally excited intermediate. The maximum absolute cross section for this process, $(6\pm3)\times10^{-18}$ cm^2 at 609 nm, is roughly what might be expected for a strong ligand-field transition.

$$Fe_2(CO)_7^- \xrightarrow[-CO]{h\nu\ (590\ nm)} Fe_2(CO)_6^- \xrightarrow[-CO]{h\nu\ (590\ nm)} Fe_2(CO)_5^- \xrightarrow[-CO]{h\nu\ (590\ nm)} Fe_2(CO)_4^- \qquad (4.21)$$
$$\hookrightarrow \quad h\nu\ (590\ nm) \quad \hookrightarrow$$

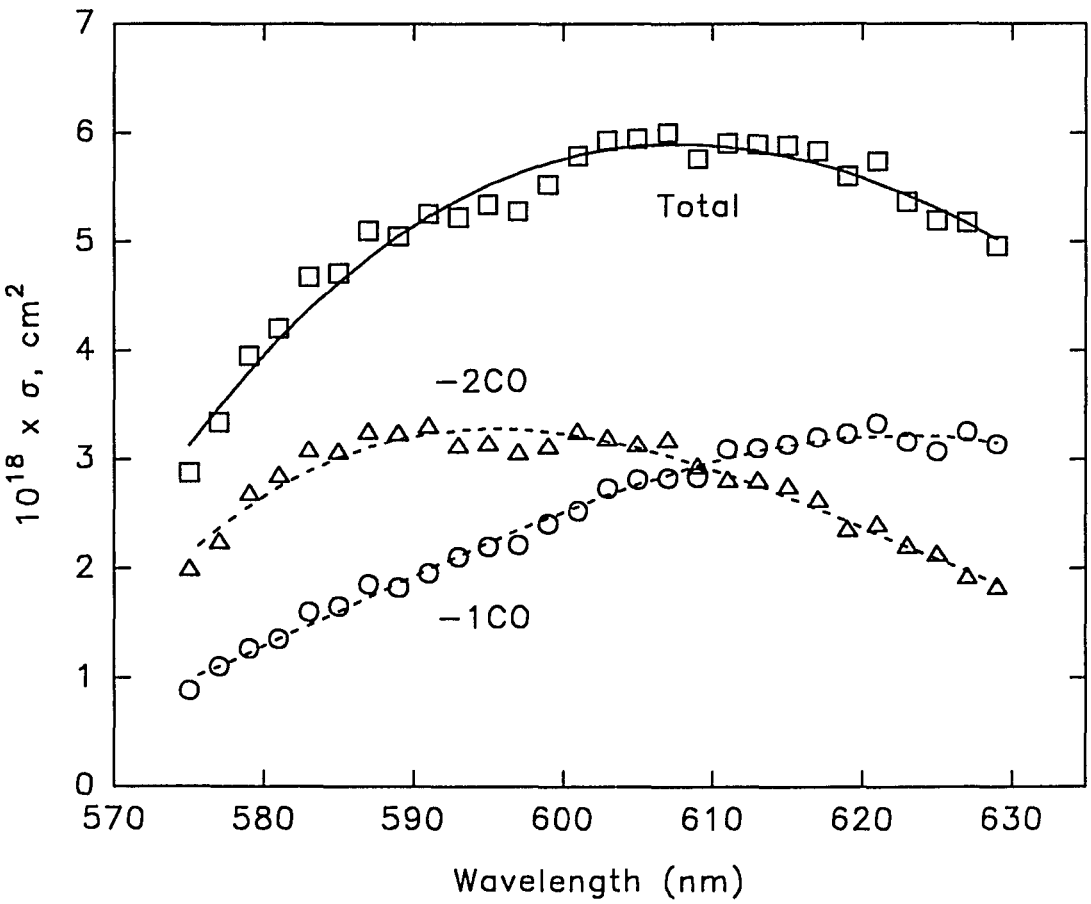

FIGURE 4.1: Primary Photoproduct Distribution for $Fe_2(CO)_7^-$
(The solid and dashed lines are just visual guides.)

A small amount of $Fe_2(CO)_3^-$ forms by competitive photodissociation of the "terminal" dinuclear anion $Fe_2(CO)_4^-$:

$$Fe_2(CO)_4^- \xrightarrow{h\nu\ (590\ nm)} Fe(CO)_4^- + \text{"Fe"}\ (90\%) \qquad (4.22.a)$$
$$\hookrightarrow Fe_2(CO)_3^- + CO\ (10\%) \qquad (4.22.b)$$

Again, electron ejection experiments indicate that electron photodetachment is the major (if not sole) source of $Fe(CO)_4^-$. Dinuclear attachment products are also observed, but to a lesser extent than in the near infrared experiments:

$$Fe_2(CO)_4^- \xrightarrow{h\nu\ (590\ nm)} e^- + Fe_2(CO)_4\ (90\%) \qquad (4.23.a)$$
$$\hookrightarrow Fe_2(CO)_3^- + CO\ (10\%) \qquad (4.23.b)$$

$$e^-\ (\text{trapped}) + Fe_2(CO)_9 \longrightarrow Fe(CO)_4^-\ (90\%) \qquad (4.24.a)$$
$$\hookrightarrow Fe(CO)_3^-\ (5\%) \qquad (4.24.b)$$
$$\hookrightarrow Fe_2(CO)_7^-\ (3\%) \qquad (4.24.c)$$
$$\hookrightarrow Fe_2(CO)_6^-\ (2\%) \qquad (4.24.d)$$

The competition between photodetachment and photodissociation shown in Reactions 4.23 suggests (if not proves) that photodetachment proceeds through a vibrationally excited intermediate. The decrease in dinuclear signal for the 590 nm experiments (relative to the dinuclear signal observed at 1064 nm) is probably due to an increase in the average detached electron energy that becomes possible with a more energetic photon. Even though the vibrationally-induced electron detachment mechanism favors low electron kinetic energies (as discussed in Chapter 3), only a small change in the average kinetic energy of the detached electrons is required to significantly alter the di- to mononuclear branching

ratio. Finally, continuous ejection and laser fluence dependence experiments confirm that electron detachment occurs solely from $Fe_2(CO)_4^-$ at all wavelengths studied; this implies that the electron affinity of $Fe_2(CO)_4$ is substantially lower than the electron affinities of its more highly coordinatively saturated homologues.

$Co_2(CO)_n^-$

While cobalt has a stable neutral dinuclear precursor, direct dinuclear anion formation is very inefficient at all nominal electron energies. The signal-to-noise ratio for the cobalt experiments is therefore the lowest of the experiments in this Chapter.

$$e^- + Co_2(CO)_8 \longrightarrow Co(CO)_4^- + Co(CO)_4 \quad (4.25.a)$$
$$\hookrightarrow Co(CO)_3^- + CO + Co(CO)_4 \ (< 2\%) \quad (4.25.b)$$
$$\hookrightarrow Co_2(CO)_6^- + 2CO \ (< 1\%) \quad (4.25.c)$$
$$\hookrightarrow Co_2(CO)_5^- + 3CO \ (< 5\%) \quad (4.25.d)$$

Beyond $Co_2(CO)_6^-$ the dicobalt anions stop absorbing 1064 nm radiation:

$$Co_2(CO)_6^- \xrightarrow[-CO]{h\nu\ (1064\ nm)} Co_2(CO)_5^- \xrightarrow{h\nu\ (1064\ nm)} N.R. \quad (4.26)$$

Apparent metal-atom loss is observed in the visible, with even stronger competition from photodissociation than for the diiron system:

$$Co_2(CO)_6^- \xrightarrow[-CO]{h\nu\ (590\ nm)} Co_2(CO)_5^- \xrightarrow{h\nu\ (590\ nm)} Co_2(CO)_4^- \quad (4.27)$$

$$Co_2(CO)_4^- \xrightarrow{h\nu\ (590\ nm)} Co(CO)_4^- + \text{"Co"} \ (70\%) \quad (4.28.a)$$
$$\hookrightarrow Co_2(CO)_3^- + CO \ (30\%) \quad (4.28.b)$$

A decrease in the mononuclear signal is again observed if electrons are ejected immediately after the laser event. The $Co_2(CO)_4^-$ anion is positively identified as the sole

detaching species. No dinuclear attachment products are observed since the branching ratio for direct dinuclear formation is so low:

$$Co_2(CO)_4^- \xrightarrow{h\nu\ (590\ nm)} \begin{cases} e^- + Co_2(CO)_4\ (70\%) & (4.29.a) \\ Co_2(CO)_3^- + CO\ (30\%) & (4.29.b) \end{cases}$$

$$e^-(trapped) + Co_2(CO)_8 \longrightarrow Co(CO)_4^- + Co(CO)_4 \qquad (4.30)$$

Again, the competition between photodetachment and photodissociation in the "terminal" dinuclear anion is partial evidence for the involvement of a common vibrationally excited intermediate.

Interpretation and Discussion

There are a few differences between these experiments and the previously-reported experiments in which apparent metal atom loss was observed,[4.3,4.8] as outlined in Reactions 4.31 through 4.34, below:

$$e^- + M(CO)_n \longrightarrow M(CO)_{n-1}^- + CO \qquad (4.31)$$

$$M(CO)_{n-1}^- \xrightarrow{CID} M^- + (n-1)CO \qquad (4.32)$$

$$M^- + M(CO)_n \longrightarrow M_2(CO)_{n-1}^- + CO \qquad (4.33)$$

$$M_2(CO)_{n-1} \xrightarrow{CID\ (1\text{-}20\ eV)} M(CO)_{n-1}^- + \text{"M"} \qquad (4.34)$$

First, these investigators used collision-induced dissociation (CID) to strip all carbonyl groups from $Cr(CO)_5^-$ or $Fe(CO)_4^-$, leaving the atomic metal anions Cr^- and Fe^-. These bare metal ions were then allowed to react with background $Cr(CO)_6$ or $Fe(CO)_5$ to form $Cr_2(CO)_5$- or $Fe_2(CO)_4^-$, respectively. In contrast, the "terminal dinuclear anions" of this Dissertation were all produced by photodissociation of more highly substituted dinuclear anions. Second, the prior investigators used direct collisional excitation of the terminal dinuclear anions, while here it is assumed that internal conversion creates the predissociative species. Finally, the center-of-mass collision energies in the previous experiments ranged from about 1-20 eV, while the photon energies used here were all under about 2 eV. The potential significance of each of these differences will be addressed separately, below.

While it is natural to assume that an asymmetrically synthesized dinuclear metal carbonyl anion might retain its asymmetry and dissociate into a nearly-saturated metal carbonyl anion fragment and a metal atom, the possibility of internuclear carbonyl transfer cannot be ignored. While it has not yet been possible to obtain temperature-dependent ^{13}C NMR spectra for a coordinatively unsaturated metal carbonyl species, a variety of carbonyl scrambling modes have been observed for much more sterically hindered, saturated dinuclear metal carbonyls.[4.10] Cyclic scrambling and pairwise and one-for-one bridge-terminal exchange have been observed; all invoke some sort of bridging carbonyl intermediate structure. It is therefore highly probable that the coordinatively unsaturated dinuclear anions studied here also are stereochemically nonrigid and that their carbonyl groups readily transfer through a bridging intermediate from one metal center to another. It is quite reasonable to assume that scrambling in these unsaturated complexes is even more facile than in the fully coordinatively saturated complexes of the NMR studies.

One possible excepting condition to internuclear carbonyl transfer could be the presence of a formal metal-metal multiple bond, since little is known about the fluxional behavior of multiply bound dinuclear complexes. (Of course, such higher-order bonding also makes it far less likely that metal atom loss is the lowest-energy dissociation pathway.) Certainly, the metal centers in the nascent terminal dinuclear anions formed by Reaction 4.33 must be singly bound; multiple bonding could not occur until at least one carbonyl had transferred to the less-saturated metal center. Carbonyl transfer thus could be driven sterically, entropically, and by the potential increase in bond order between the metal centers. Interestingly, Smalley and coworkers have reported strong spectroscopic evidence

that the neutral chromium dimer has a sextuple bond.[4.11] While direct structural data have never been obtained for gas-phase metal carbonyl anions, Wronka and Ridge[4.12] have presented convincing kinetic evidence for iron-iron double bonds in $Fe_2(CO)_n^-$ ($5 \leq n \leq 7$), and as Squires[4.3] points out, the correlation they observe between the relative rate constants and the *average* electron deficiency per metal center (assuming double bonds) suggests that these anions are symmetrically substituted. It is difficult to envision an energetic process that could cause the near-concerted transfer of all carbonyls from one metal center to another (with an accompanying decrease in bond order) and the loss of the "naked" metal atom. Finally, Leopold and Lineberger[4.13] have presented spectroscopic evidence for multiple bonding in Fe_2 and Co_2 neutrals.

The next issue to be addressed concerns the nature of the excitation process. A potential ambiguity exists in the photoactivated experiments since it cannot be known for sure whether dissociation or detachment occurs from an electronically or vibrationally excited penultimate species; no such ambiguity exists for the collisionally activated ions of the previous investigations. However, typical vibrational state densities for such species in this energy regime are at least 10^{14} per wavenumber, so internal conversion is expected to be extremely rapid. There is additional evidence for the presence of vibrationally excited intermediates in the different competitive branching processes that were observed for iron and cobalt. The branching between loss of one and two carbonyls observed for the visible photodissociation of $Fe_2(CO)_7^-$ suggests that a vibrationally excited intermediate is responsible at least for the loss of the second carbonyl, since no "direct" dissociation process (a $\sigma \rightarrow \sigma^*$ transition for an electron in a metal-carbon bond) could simultaneously remove two

carbonyls. It is probable, of course, that *both* carbonyls are lost from a vibrationally excited species, since in a direct dissociation much of the energy in excess of the first bond strength would go into relative translation of the photoproducts. Branching was also observed between carbonyl and electron loss from photoexcited $Fe_2(CO)_4^-$ and $Co_2(CO)_4^-$. While it is possible that this branching behavior could be due to two different electronic transitions (one dissociative and one "photoelectric"), it is more likely that both processes involve a common, vibrationally excited intermediate. As discussed in Chapter 3, vibrationally-induced electron detachment is a known phenomenon available to activated anions possessing a curve crossing with their corresponding neutral. It is encouraging that such a process has been invoked previously to explain transmission losses for the collision-induced dissociation of *mono*nuclear metal carbonyl anions in a triple-quadrupole mass spectrometer.

As for the difference in the energy regimes of these two sets of experiments, it is possible that different dissociation channels become thermodynamically and kinetically accessible at higher collision energies. However, the collision energies reported for the previous CID experiments represent the maximum that may be deposited; the *average* energy deposited into a polyatomic ion from a neutral collision is at most a few percent of the total available center-of-mass collision energy.[4.14] As it appears that the threshold for apparent "neutral metal atom loss" is on the order of 1 eV, the energy regimes of the CID and photoactivated experiments are quite comparable. It appears that detachment is the lowest-energy process available to these species, and as such it ought to dominate the collisional activation behavior.

In conclusion, vibrationally-induced electron detachment represents a much more palatable explanation than neutral metal atom loss from an asymmetrically-substituted dinuclear species for the activated processes observed for the "terminal" dinuclear anions $Cr_2(CO)_5^-$, $Fe_2(CO)_4^-$, and $Co_2(CO)_4^-$. It remains curious that detachment occurs only from those dinuclear anions having the same number of carbonyls as their most nearly saturated mononuclear counterparts: the 17-electron $Cr(CO)_5^-$ and $Fe(CO)_4^-$ and the 18-electron $Co(CO)_4^-$. Perhaps this is merely coincidental, but it could indicate a systematic relationship between the degree of coordinative saturation and the electron affinity of a dinuclear metal complex anion. These dinuclear complexes are not well-enough understood at this point for such effects to be predicted *a priori*. Simple structural considerations such as the metal-metal bond order and the presence or absence of bridging carbonyls have yet to be satisfactorily addressed; a discussion of the electron affinities of these species would proceed more profitably from reasonably well-known structures.

CHAPTER 5:

CHROMIUM PENTACARBONYL ANION

Over about the past twenty years, transition metal carbonyl species have been studied extensively both for their potential relevance to catalysis and toward gaining a broader understanding of the fundamental electronic structure, bonding, and reactivity of transition metal-containing species. The gas-phase research community has made some important contributions to this field, both in the study of gas phase neutrals[5.1] and in mass spectrometric studies of cations[5.2] and anions.[5.3] Of particular interest here are studies concerning the photochemistry,[5.4] thermochemistry,[5.5] and oxidation[5.6-5.9] of chromium carbonyl species—specifically chromium pentacarbonyl anion.

In a previous investigation of the visible photodecomposition behavior of $Cr(CO)_5^-$,[5.4] it found that this ion absorbs broadly for photon energies above about 2.2 eV. While absolute cross sections were not reported, they must be fairly large given that a filtered xenon-arc lamp was used as the light source. Since $D[(CO)_4^-Cr—CO]$ is somewhat lower than 2.2 eV (see below) it is likely that the observed photodecomposition behavior corresponds to the optical absorption spectrum of $Cr(CO)_5^-$, but it is also possible that this energy actually represents the onset of two-photon dissociation behavior, which would be difficult to observe without a more intense (laser) light source. The observed visible absorption band was tentatively assigned to a metal-ligand charge transfer transition.

Although $Cr(CO)_5^-$ appears to be transparent in the red, it was discovered here that it does absorb again in the near-infrared, at least at 1064 nm, with an approximate cross

section of (3±2) × 10^{-19} cm^2, found by the methods of Appendix A. Absorption in this energy region is presumably ligand-field (d-d) in nature. While the structure of the gas-phase ion is unknown, spectra of the neutral $Cr(CO)_5$ species obtained in cryogenic matrices show that the sixth coordination site is occupied even by "noncoordinating" molecules, giving the metal carbonyl a square pyramidal structure.[5.10] The gas-phase anion, however, is probably not square pyramidal, not only because there is nothing occupying a sixth coordination site ($Cr(CO)_5^-$ is already 17-electron) but also since the extent of ligand-field distortion (corresponding to *z*-axis elongation) that would be required to achieve a 1.16 eV (1064 nm) ligand-field transition is unreasonably large. Instead, it is likely that $Cr(CO)_5^-$ exists as a Jahn-Teller distorted trigonal bipyramidal $Cr(CO)_5^-$ structure; the d-d splitting accompanying this loss of degeneracy could more easily be in the 1 eV range. The power dependence of the photodissociation process indicates that it requires two photons (see Appendix A), which implies that 60.5 kcal/mol > $D[(CO)_4^-Cr—CO]$ > 33.6 kcal/mol. These limits assume that an average 325 K $Cr(CO)_5^-$ ion contains about 6.8 kcal/mol of internal energy and ignore thermal broadening—the actual limits will be somewhat narrower since "clean" one- or two-photon behavior would if thermally populated two- or one-photon dissociations are possible. This result agrees with the previously reported values of 40.6±3.5 kcal/mol obtained by Sunderlin and Squires and 44.7±3.5 kcal/mol obtained by Hop and McMahon, both based on CID threshold measurements.

Since $Cr(CO)_5^-$ requires the absorption of two 1064 nm photons to dissociate, a highly vibrationally excited species (designated $Cr(CO)_5^{-\dagger}$) may be prepared by the absorption of a single photon. Internal conversion is sufficiently rapid that sequential two-

photon absorption (from the ground electronic state) occurs readily during a 200-μs Nd:YAG laser pulse. The following scheme was used to produce $Cr(CO)_5^{-\dagger}$. Note that it is not possible to prevent dissociation from occurring within a laser pulse; Reaction 5.2.b always occurs to some extent after Reaction 5.2.a:

$$e^- (\leq 2\ eV) + Cr(CO)_6 \longrightarrow Cr(CO)_5^- + CO \qquad (5.1)$$

$$Cr(CO)_5^- \xrightarrow{h\nu\ (1064\ nm)} [Cr(CO)_5^{-*}] \xrightarrow{k_{ic}} Cr(CO)_5^{-\dagger} \qquad (5.2.a)$$

$$Cr(CO)_5^{-\dagger} \xrightarrow{h\nu\ (1064\ nm)} [Cr(CO)_5^{-\dagger *}] \xrightarrow{k'_{ic}} [Cr(CO)_5^{-\ddagger}] \xrightarrow[-CO]{k_{pd}} Cr(CO)_4^- \qquad (5.2.b)$$

In Reactions 5.2 an asterisk designates an excited electronic state, a dagger indicates a long-lived vibrationally excited species, and a double dagger indicates a predissociative species. The internal conversion rate constant k_{ic} is extremely large, and the predissociation rate constant k_{pd} should be large enough for dissociation to be complete within at most a few milliseconds. These processes were discussed in a general sense in Chapter 3. Given that $Cr(CO)_5^{-\dagger}$ is indistinguishable from $Cr(CO)_5^-$ in the mass spectrum, the excited fraction was estimated from the extent of dissociation using the methods of Appendix A.

Once $Cr(CO)_5^{-\dagger}$ is prepared the effects of this excess vibrational energy may be examined for as long as this internal energy remains in the molecule. The default mechanism for energy disposal in the absence of collisions is sequential infrared fluorescence, so the first priority is to determine the radiative "lifetime" of this species with a two-pulse photodissociation experiment, which is discussed in the following section of this

Chapter. Afterward, the effect of this excess internal excitation on the oxidation reactions of $Cr(CO)_5^-$ is examined, and the results are compared to a previous study in which unusual energetic effects on the oxidation rate and branching behavior were observed. Finally, it is shown that bimolecular reactions may also be used as internal energy probes to measure relaxation rates, and the radiative relaxation rate constant measured for $Cr(CO)_5^{-\dagger}$ by this method is compared to that determined by the more conventional two-pulse photodissociation experiments.

Radiative Relaxation Probed by Two-Pulse Photodissociation Experiments

An observation of a radiative lifetime in the millisecond regime or slower would be adequate proof that the excess internal energy in $Cr(CO)_5^{-\dagger}$ is indeed vibrational in nature. Reaction 5.3 shows the elementary processes (discussed individually in Chapter 3) assumed to occur during the two-photon dissociation of a generic polyatomic molecule A:

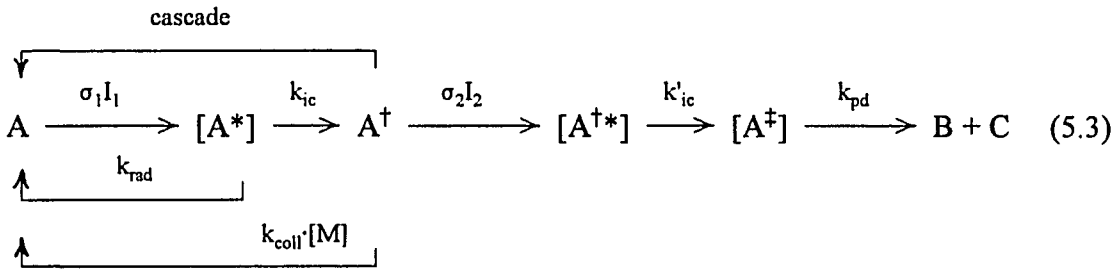

(5.3)

Freiser and Beauchamp were not only the first to observe photodissociation by sequential two-photon absorption and to correctly identify the involvement of a vibrationally excited intermediate,[5.11] but they also realized the potential that such systems afforded for the study of vibrational relaxation mechanisms.[5.12] After absorption of the first photon ($\sigma_1 I_1$) the excited electronic state can fluoresce (k_{rad}) or, more likely for a large polyatomic molecule, interconvert to a vibrationally excited ground electronic state (k_{ic}). The vibrationally excited molecule can absorb another photon ($\sigma_2 I_2$), internally convert (k'_{ic}), and predissociate; or it can collide with another species ($k_{coll}\cdot[M]$) and lose some of its vibrational excitation; or, under low pressure conditions, it can undergo sequential infrared fluorescence (cascade). Multi-step cascade kinetic models are to be distinguished from single-step "rate process" kinetic models. For example, electronic fluorescence uses a rate process model, while collisional quenching can use either a rate process or a cascade model, depending on how

much energy can be carried away by a single collision and on the amount of internal energy that must be removed for the ion to be considered "relaxed."

The two-pulse photodissociation method developed by Dunbar[5.13] was used to probe the lifetime of the intermediate $Cr(CO)_5^{-\dagger}$ species. This technique involves photoexciting the ion population with two pulses of laser light separated by a variable time delay *T*, and by measuring as a function of *T* the extent of excess dissociation due to excited-ion carryover between the laser pulses. Any ion still possessing internal energy greater than the "one-photon threshold" (the dissociation threshold energy minus the photon energy) at the end of the delay *T* will dissociate if it absorbs another photon from the second laser pulse. Dunbar and coworkers have used two-pulse photodissociation and similar two-photon techniques to measure radiative relaxation rates for several organic ions. More recently they have used an alternate method, time resolved photodissociation (TRPD),[5.14] as an ion thermometry technique to study the relaxation of a variety of species including ferrocene cation.[5.15]

Since collisional quenching can be a much more efficient relaxation mechanism than sequential infrared fluorescence, in order to measure the collision-free component of the relaxation for internally excited ions these experiments must be carried out at pressures below about 10^{-7} Torr. Therefore, $Cr(CO)_6$ is admitted to the vacuum chamber through a pulsed valve so that the cell pressure may return to near the chamber base pressure before the photoexcitation pulses. The ion-background collision rate under these conditions is estimated to be about 0.3 s^{-1}. A one-second delay is added after the ionization step to allow both ion cooling and the return to low pressure, after which the ions are irradiated with a defocused Nd:YAG laser pulse. Any ions that dissociate because of this first laser pulse are

ejected from the cell with a swept r.f. pulse. The ions are allowed to relax for a delay T after which they are irradiated with a second laser pulse. All ions are detected after this pulse. Occasionally, a one-pulse control experiment is performed so that the extent of two-photon dissociation to be expected from a single laser pulse can be determined. The extent of excited-ion carryover between the laser pulses is proportional to the amount by which the second-pulse dissociation exceeds the extent of dissociation observed for these control runs. A much more precise, mathematical description of this data analysis procedure is given in the appropriate section of Appendix A.

The results for the two-pulse photodissociation of $Cr(CO)_5^-$ are shown below in Figure 5.1. Account has been taken of the variation of the relative first and second pulse energies (measured independently by reading the output of a thermopile power meter with a digital storage oscilloscope) as a function of T. While it was not possible to measure the ion-cloud hole-burning fraction f (as discussed in Appendix A), it was assumed to be approximately 0.9. Also shown in Figure 5.1 is an attempted fit to the data with a clearly inadequate, single-exponential relaxation model. While a cascade model is definitely more appropriate, such a fit is not included at this point because the considerations discussed in Chapter 7 are necessary to develop a sufficiently sophisticated model.

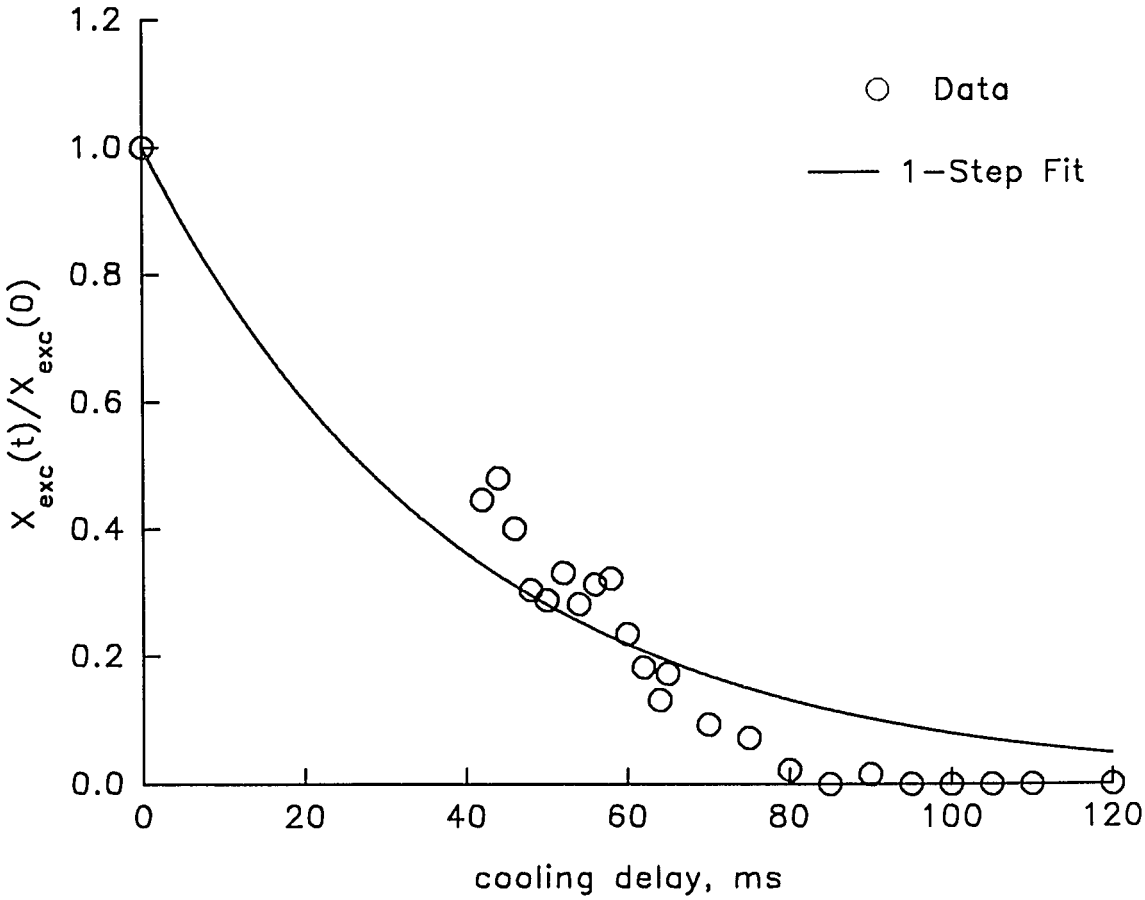

FIGURE 5.1: Two-Pulse Photodissociation of $Cr(CO)_5^-$

The radiative "lifetime" of this vibrationally excited species is roughly 45 ms. This represents the average time it takes a $Cr(CO)_5^-$ molecule to relax from roughly 33.6 kcal/mol of internal energy (6.8 kcal/mol from the thermal 325 K distribution plus the 26.8 kcal/mol photon energy) to below the one-photon threshold of roughly 17.1 kcal/mol (43.9 kcal/mol $D[Cr^-(CO)_4—CO]$ minus the photon energy)—a total energy loss of about 16.5 kcal/mol. The average energy disposal rate is therefore about 367 $kcal \cdot mol^{-1} \cdot s^{-1}$, which if taken to represent the energy disposal rate in the middle of this energy range yields a radiative rate constant of about $14.5 \pm 3.0\ s^{-1}$. This is quite fast, and likely represents the large contribution of the high-frequency CO stretching modes to the overall quenching rate. This is discussed in much more detail in Chapter 7.

Oxidation Reactions of Vibrationally Excited $Cr(CO)_5^-$

The oxidation of transition metals and their complexes is a topic of widespread importance. In response to this, a number of groups have investigated the gas-phase oxidation chemistry of transition metal ions in an effort to understand the mechanistic details of metal oxidation, determine metal-oxygen and metal oxide-ligand binding energies, and probe the reaction chemistry of metal oxide complexes. Several recent studies have focussed on the gas-phase oxidation reactions of 17-electron metal carbonyl anions.[5.6-5.9] Of primary interest here are three studies that include the oxidation chemistry of $Cr(CO)_5^-$. Initially, Squires and coworkers[5.7] used the flowing afterglow (FA) method to investigate the kinetics and branching ratios of the gas-phase reactions of metal carbonyl anion complexes with oxygen. They observed 17-electron complexes to react relatively slowly to form a range of metal carbonyl oxide and metal polyoxide anions. Subsequently, Bricker and Russell[5.8] studied the reactions of $Cr(CO)_5^-$ with oxygen under the low pressure conditions of a Fourier transform ion cyclotron resonance mass spectrometer (FT-ICR) and observed an unusual temperature dependence for the reaction. Not only did the reaction rate increase slightly with translational excitation of the $Cr(CO)_5^-$ reactant, but it also increased dramatically when the reagent inlet temperature was raised from ambient to 100° C. The latter effect was attributed to the generation of a high energy, more reactive form of $Cr(CO)_5^-$ upon ionization. The mechanisms of the primary and higher order reactions were also investigated using MS/MS and isotopic labeling techniques. Most recently, Hop and McMahon[5.9] used both high-pressure ion-molecule reactions in their external FT-ICR ion source and low-

pressure reactions in the cell to try to reconcile some of the differences from the first two studies. They also obtained bond dissociation energies for many of the metal carbonyl and metal oxide carbonyl complexes using collision induced dissociation threshold techniques. Here, the oxidation reactions of vibrationally excited $Cr(CO)_5^-$ are investigated to gain insight into the reaction mechanism and to help interpret the unusual energetic results of Bricker and Russell.

Figure 5.2 shows a plausible mechanism for the primary oxidation reactions of $Cr(CO)_5^-$.[5.6] There should be a substantial activation barrier[5.16] to the formation of the η^1-superoxide (k_s) since total electronic spin is not conserved in this reaction: dioxygen is a ground-state triplet and $Cr(CO)_5^-$ is a ground state doublet. While this chromium superoxide species is 18-electron, formation of the 17-electron η^2-peroxide species (k_f) is presumably driven thermodynamically by the formation of another chromium-oxygen bond, with the accompanying loss of a carbonyl. The primary ionic products are $Cr(CO)_3O_2^-$ (kinetically favored) and $Cr(CO)_3O^-$ (thermodynamically favored because of the formation of the stable CO_2 neutral). Formation of $Cr(CO)_3O^-$ proceeds through a geometrically-constrained, four-center transition state and is thus labeled the "tight" channel, relative to the "loose" $Cr(CO)_3O_2^-$ channel. It is not known how much more exothermic the formation of $Cr(CO)_3O^-$ is relative to the formation of $Cr(CO)_3O_2^-$. It is believed that the oxygen atoms in $Cr(CO)_3O_2^-$ are bound separately as the dioxo structure shown, both by analogy to a similar matrix-isolated dioxygen species[5.17] and since no dioxygen loss was observed upon 10-eV collisional activation of this ion.[5.9]

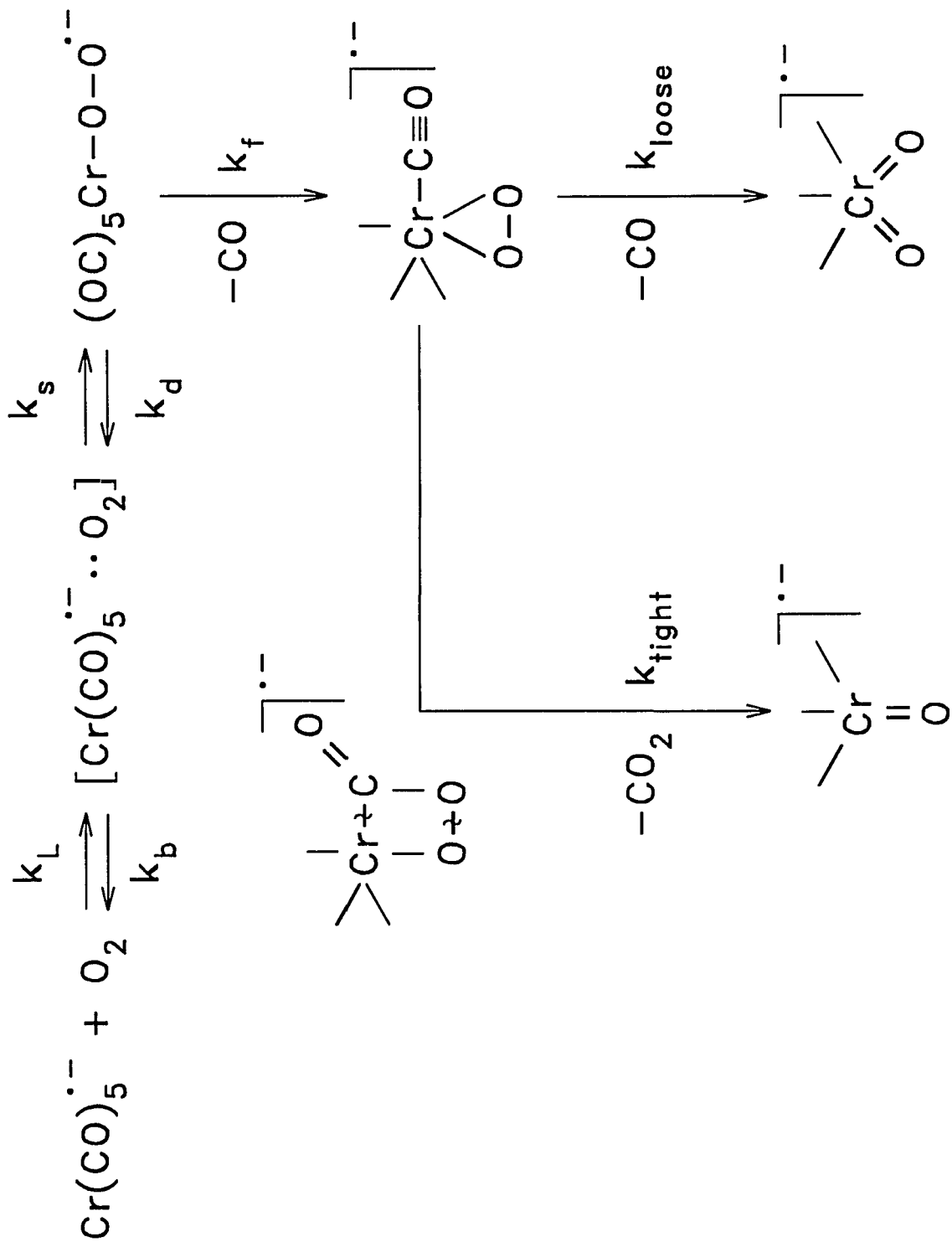

FIGURE 5.2: $Cr(CO)_5^-$ Oxidation Scheme

The overall rate constant for this reaction was measured previously at 296 K in a flowing afterglow, and is found to be 4.0×10^{-11} $cm^3 \cdot s^{-1}$, or roughly 7% of the Langevin collision rate.[5.7] This low efficiency is typical of radical-radical association reactions.[5.16] The branching fraction for the kinetic product was only 5% under these conditions. The corresponding rate constant and branching fraction measured here by FT-ICR were $(5\pm1)\times10^{-11}$ $cm^3 \cdot s^{-1}$ (9±2 % efficient) and 9±2 %, respectively. While this rate constant compares favorably to the FA number, the branching fraction is considerably higher, most likely because the effective temperature in the ICR cell is higher (due to the proximity of the electron filament) than in the FA. This is true even if the ions trapped in the ICR cell are completely thermalized, as they are believed to be here (the branching fraction was even higher in less-well-thermalized experiments). By comparison, Bricker and Russell obtain a branching fraction of roughly 10% using a similar instrument, while Hop and McMahon observe a 5% branching fraction for ions generated in their high-pressure external ion source and 12±1 % for $Cr(CO)_5^-$ ions allowed to react with oxygen in the ICR cell.

The effects of vibrational excitation on the overall rate constant and branching behavior are examined by preparing a vibrationally excited $Cr(CO)_5^{-\dagger}$ species by the methods described above. Since both excited and unexcited ions will be present (the distribution of $Cr(CO)_5^-$ internal energies is bimodal), the change in the observed parameters due solely to the excited population must be algebraically extracted from the combined signal. This is accomplished for a generic physical property P with the following equation:

$$P_{tot} = P_{exc} X_{exc} + P_{therm}(1 - X_{exc}) \qquad (5.4)$$

in which the excited fraction X_{exc} is determined by the methods of Appendix A. All subsequent discussion of vibrationally excited effects will assume that this correction has been made.

The overall oxidation rate decreases by a factor of 1.2±0.1 upon the addition of one 1064 nm photon to $Cr(CO)_5^-$ before the reaction. Even though a unimolecular reaction rate constant can only increase with added internal energy, the rate of the back reaction increases faster with internal energy than the rate of the forward reaction. The efficiency of this reaction can be expressed in terms of k_b, k_s, k_d, and k_f assuming a double-steady-state approximation in the ion-dipole complex and the η^1-superoxide:

$$e = \frac{k_f k_s}{k_b(k_d + k_f) + k_f k_s} \tag{5.5}$$

It is curious that the oxidation of highly vibrationally excited $Cr(CO)_5^-$ is only slightly less efficient than for the thermal anion. Back dissociation out of an ion-molecule complex (k_b) is considered "loose" and ought to speed up much more with increasing internal energy than the characteristically "tight" radical-radical association reaction (k_s). It is possible that vibrational-translation energy transfer in the ion-dipole collision complex is inefficient; in this case k_b and k_s would both be relatively insensitive to vibrational energy. The reaction efficiency does increase with translational excitation, most likely because the activation barrier for radical-radical association corresponds to that required to bring an oxygen atom close enough to the chromium nucleus to alter the total electronic spin. Since the chromium atom is very near the center of mass of $Cr(CO)_5^-$, the vibrational energy of this anion may not couple strongly into the association reaction coordinate.

The changes in k_f and k_d with vibrational excitation must also be considered. Both reactions might be described as "tight"—the back dissociation by microscopic reversibility and the forward reaction by the geometric constraints imposed by the formation of the η^2-peroxide. It should also be noted that the relative density of product translational states for k_d is 1.18 times higher than that for k_f—identical within experimental error to the factor by which the reaction slows down with vibrational excitation. While this is probably only a coincidence, the overall result remains the same: the reaction efficiency is relatively insensitive to vibrational excitation. (This may account for the congruence between the rate constant measured here by ICR and that measured by Squires in a flowing afterglow.) It seems more reasonable to postulate that the efficiency of each individual step (η^1-superoxide formation and η^2-peroxide formation) is relatively insensitive to energy rather than assuming that a large change in the efficiency of one step is almost exactly offset by nearly as large a change in the other.

The branching ratio for this reaction is also altered by the presence of excess internal energy. The fraction branching into $Cr(CO)_3O_2^-$ (the kinetic product) increases from 9±2 % at thermal energies to 50±10 % at the internal energy corresponding to thermal plus one 1064 nm photon. The reaction shifts away from the thermodynamic channel at higher internal energies because of the geometrical constraints imposed by the four-centered transition state leading to CO_2 loss. This geometrical constraint prevents the density of states for the thermodynamic ("tight") channel from rising as rapidly as that of the kinetic ("loose") channel with increasing internal energy in the activated intermediate.

These results for the vibrationally excited oxidation reaction may be contrasted with the unusual behavior observed by Bricker and Russell when they heated the inlets of their FT-ICR. Since the $Cr(CO)_5^-$ oxidation reaction slows down with increasing anion vibrational energy, the oxidation rate increase they observed can only be due to electronic excitation. Their reagent inlets were heated very near the 110° decomposition temperature of $Cr(CO)_6$, and decomposition to form $Cr(CO)_5$ may have been catalyzed by the stainless steel inlet walls. It is reasonable to hypothesize that electron attachment to $Cr(CO)_5$ might form the $Cr(CO)_5^-$ anion in a long-lived, high-spin, isolated electronic state having different reactive properties than the electronic ground state anion. In any event, this system is an excellent demonstration of the utility of studying reactions of vibrationally excited species toward resolving the mechanistic details of a reaction.

Radiative and Collisional Relaxation Probed with Bimolecular Reactions

The change in branching ratio with internal energy can be used as an ion thermometric technique to probe the internal energy of $Cr(CO)_5^-$ and measure its relaxation rate. The experiment is conceptually simple: $Cr(CO)_5^-$ is formed, thermalized, and then irradiated with a Nd:YAG laser pulse. After a variable cooling delay any photodissociation or oxidation products are ejected from the cell to isolate $Cr(CO)_5^-$, which is then allowed to react with O_2 for a short period to determine the initial branching ratio. In the past, Dunbar and coworkers have used the branching ratio of unimolecular reactions as ion thermometric probes,[5.18] but this is the first instance in which a bimolecular reaction was employed for this purpose.

Plots of the initial branching ratio versus cooling delay are shown below in Figures 5.3 and 5.4 for oxygen pressures of 4.0×10^{-7} and 1.2×10^{-6} Torr. In each plot an *ad hoc* exponential fit is shown as a solid line and the thermal control measurements are shown as a dashed line. Although an effort was made to measure the initial reaction rate for the same (small) extent of reaction at all oxygen pressures, it was difficult to do so precisely. Since the overall reaction is less than 10% efficient there will be many unreactive collisions for each reactive one and the measured branching behavior will be convolved with a collisional cooling component. A slightly smaller extent of reaction was used for the lower pressure experiment, so the initial branching ratio is correspondingly larger. No attempt was made to correct the relaxation measurements for this effect since other sources of uncertainty were of comparable magnitude.

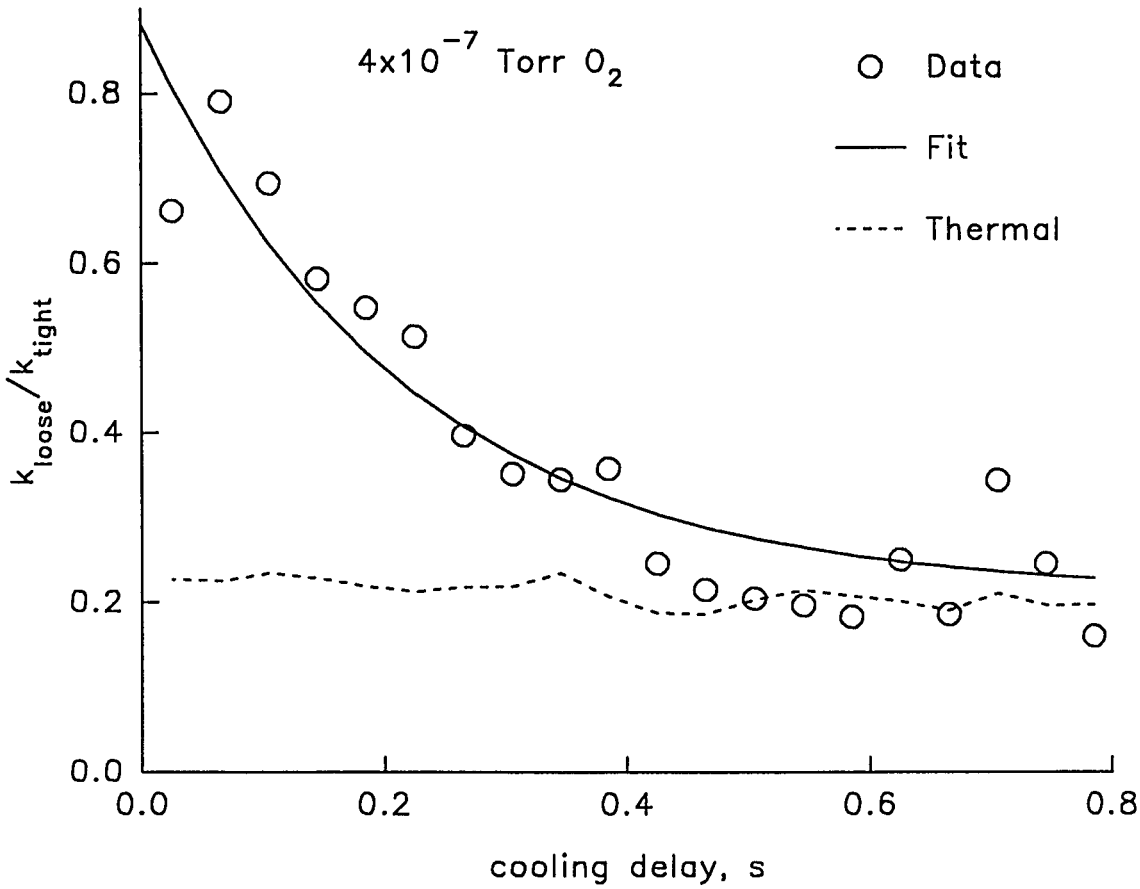

FIGURE 5.3: Relaxation of $Cr(CO)_5^{-\dagger}$ in 4.0×10^{-7} Torr O_2

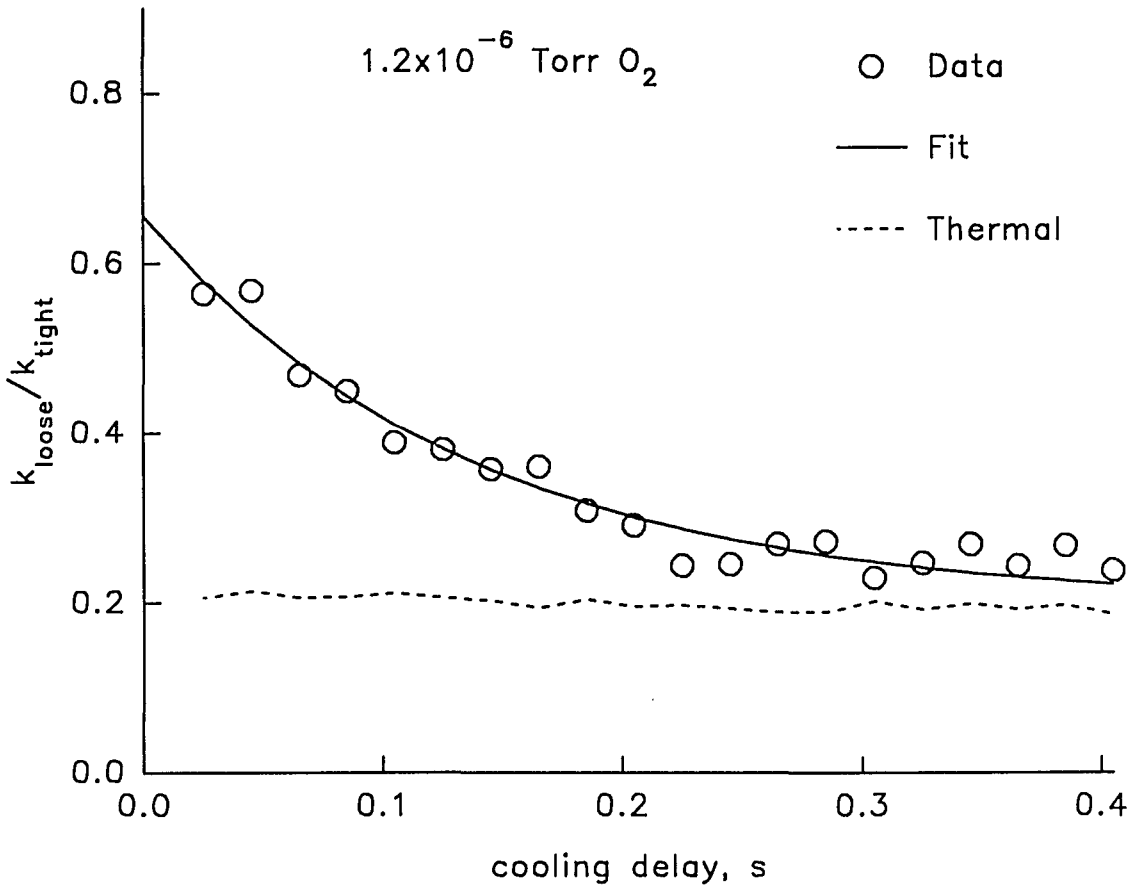

FIGURE 5.4: Relaxation of $Cr(CO)_5^{-\dagger}$ in 1.2×10^{-6} Torr O_2

This experiment was performed at three different oxygen pressures over a fairly narrow range, since at higher O_2 pressures the absolute signal diminishes too rapidly for the ions to be adequately thermalized. These data are summarized in Table 5.1 and plotted in Figure 5.5, below:

TABLE 5.1: Pressure Dependence of $Cr(CO)_5^-$ Relaxation

$p(O_2)$, Torr	k_{relax}, s^{-1}	Collisions during τ_{relax}
4×10^{-7}	4.6±0.6	1.6±0.2
1.2×10^{-6}	7.4±0.4	2.9±0.2
2×10^{-6}	11.5±2.5	3.1±0.7

The extent of reaction for the highest pressure determination was unavoidably large and its signal-to-noise ratio was substantially worse than the others, so it was not used for the radiative rate constant determination as per Equation 3.3. Fortunately, collisional quenching by oxygen is inefficient enough for the radiative component to be substantial at these pressures—the extrapolation is not too extreme. A radiative rate constant of 3.3±0.7 s^{-1} and a collisional quenching efficiency of 21±4% were found from these data. In the high pressure limit collisional quenching dominates and the number of collisions during τ_{relax} should level off, presumably to about four or five given the measured collisional quenching efficiency.

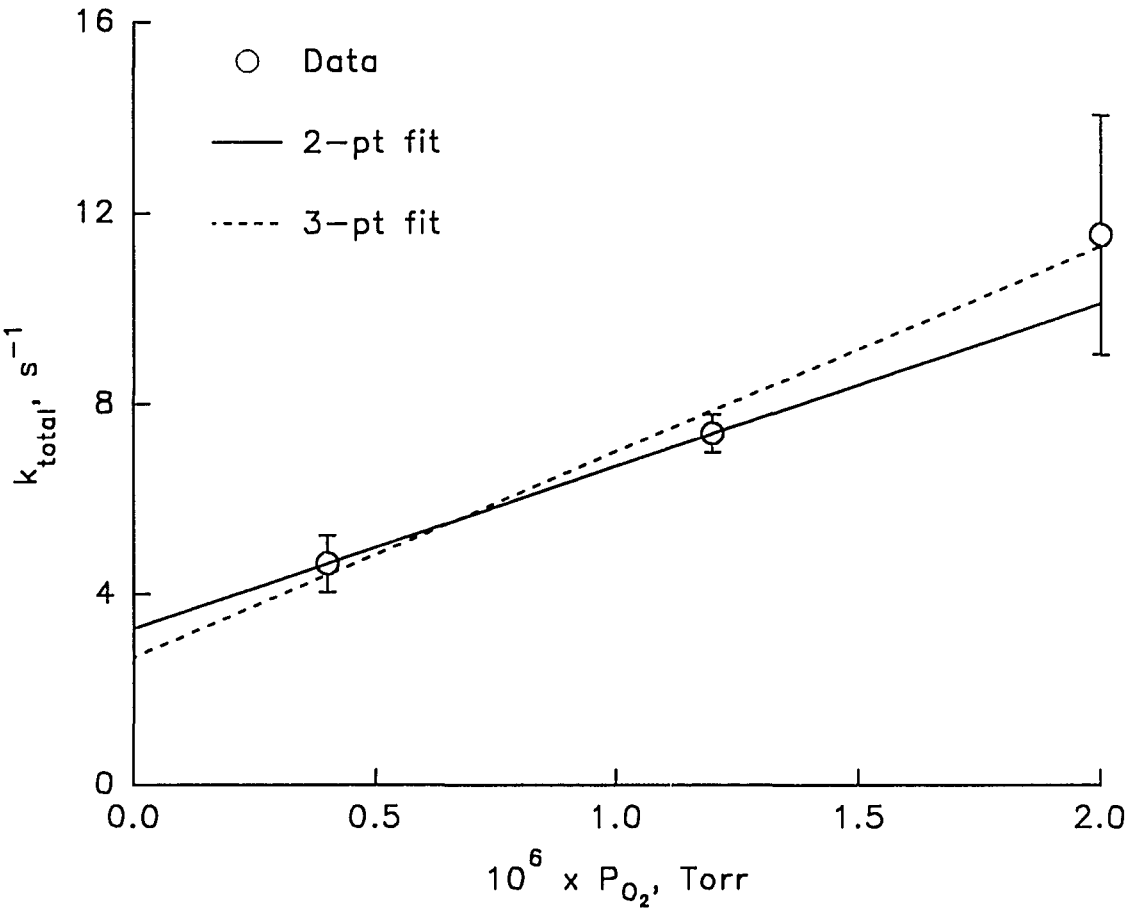

FIGURE 5.5: Pressure Dependence of k_{relax} for $Cr(CO)_5^-$

The radiative rate observed by this method is four to five times slower than that observed by the two-pulse photodissociation method. A first-order rationalization of this is that in the branching ratio experiments $Cr(CO)_5^-$ must relax much farther to appear "thermal" than in the two-pulse photodissociation experiments, in which the ions need only relax below the one-photon threshold. Radiative relaxation should slow down at lower internal energies because the strongly-radiating CO stretching modes are not as well populated. A more detailed, quantitative discussion of these measurements will be deferred until Chapter 7 so they can be discussed in a larger context by contrast to the Al_{16}^- measurements of Chapter 6.

CHAPTER 6:

ALUMINUM CLUSTER ANIONS: Al_3^- to Al_{23}^-

The primary goal of the study of small molecular clusters in the gas phase over about the past decade has been to "bridge the gap" between molecular and bulk behavior. This goal has been largely unmet, in part because the onset of truly bulk-like behavior apparently does not occur for most systems until much larger (often experimentally inaccessible) cluster sizes than were originally anticipated. However, the recent surge in fullerene research has handily demonstrated the importance of gas-phase techniques for studying clusters, as both the discovery and many important characterizations of C_{60} and other fullerene species have been carried out mass spectrometrically.[6.1,6.2]

Among the more successful cluster studies have been the investigations of the gas-phase behavior of aluminum cluster neutrals,[6.3] cations,[6.4-6.6] and anions.[6.6-6.8] While distinctly molecular behavior—the observation of "magic number" or "anomalously abundant" clusters in a mass spectrum, for example—have been observed for aluminum clusters containing up to 23 atoms, clusters in this approximate size range have been used as gas-phase models for surface reactions. Also, Jarrold points out that as relatively simple sp metals, aluminum clusters in this size range may soon be amenable to theoretical calculations.[6.9] This Chapter reports a survey of the near-infrared (1064 nm) photodissociation behavior and the oxidation reactions of aluminum cluster anions containing from 3 to 23 atoms. Additionally, the effects of vibrational excitation on the oxidation reactions of Al_{16}^- and Al_{18}^- is investigated, and radiative and collisional relaxation

rate constants are measured for Al_{16}^-. This is the first measurement of the radiative lifetime of a metal cluster.

Aluminum cluster anions were prepared in the ICR cell by direct laser vaporization from a pressed aluminum nitride pellet using the unfocussed, Q-switched, 532 nm output of the Nd:YAG laser. Photodissociation and photoexcitation experiments employed the unfocussed, long pulse, 1064 nm output of the same laser, aligned collinear to the desorption beam. The fundamental beam was shuttered during the desorption pulse to help increase the pellet lifetime and to reduce the amount of neutral desorption.

In concurrence with the results of Hettich,[6.8] especially abundant peaks were observed for Al_7^- and Al_{13}^-, and a step loss of intensity in the abundance spectrum was observed beyond Al_{23}^- (see Figure 6.1.a). Even-numbered clusters containing fewer than 13 atoms were found to be less abundant than their odd-numbered counterparts. Ejection of Al_3^- immediately after the desorption pulse showed that clusters smaller than Al_7^- were formed by ion-molecule condensation reactions involving Al_3^-; this was also supported by the decrease in intensity observed from n = 3 to 6 for Al_n^- (Figure 6.1.b). A significant fraction of the Al_7^- signal also disappeared when Al_3^- was ejected. The higher cluster anions are presumably formed by electron attachment to larger desorbed neutral clusters, so that the anomalously abundant peaks and the observed even-odd intensity alternation reflect product anion stability.

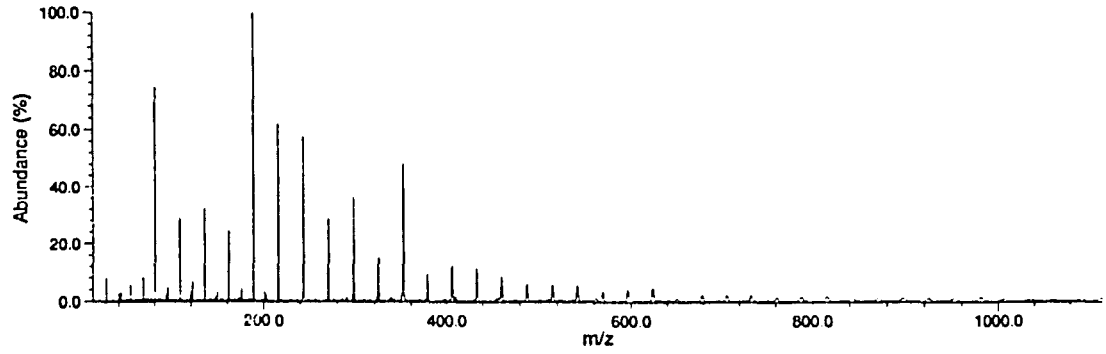

FIGURE 6.1.a: Aluminum Cluster Anion Formation without Al_3^- Ejection

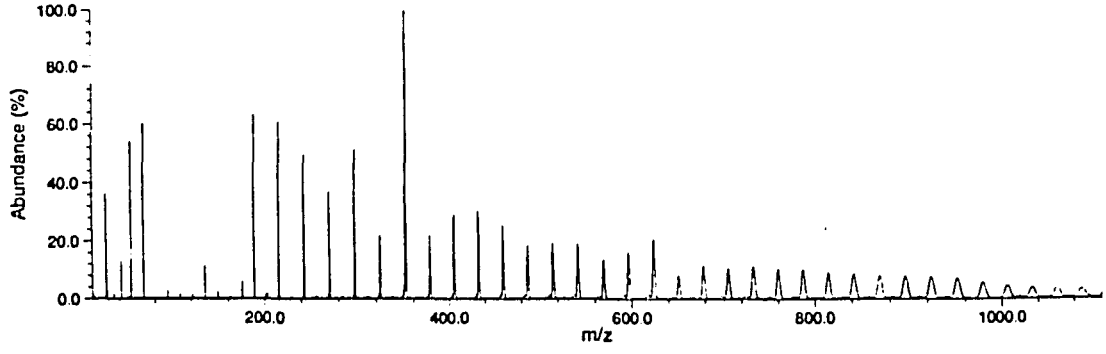

FIGURE 6.1.b: Aluminum Cluster Anion Formation with Al_3^- Ejection

Laser-desorbed neutrals proved to be excellent oxygen getters and temporarily depleted the local oxygen pressure in the cell. The magnitude of this effect was striking; a simple ion-molecule calibration reaction proved that the local oxygen pressure in the cell was depleted for several seconds after each desorption event (see Figure 6.2). This is partially a consequence of an unfortunate instrumental geometry in that the inlet gases flow right past the solids probe tip on their way to the cell, and was worked around by introducing the oxygen through a pulsed valve on the other side of the chamber. One implication of the formation of such copious quantities of neutrals is that the overall ionization efficiency must be extremely low. Assuming that one cell volume of oxygen is consumed and that the space charge limit of the trap is about 10^6 ions the approximate ratio of trapped cluster anions to desorbed aluminum atoms is computed to be 1 ppm or less! (A more accurate calculation would require knowledge of the oxygen flow rate and a reliable estimate of the absolute number of trapped ions, among other parameters.)

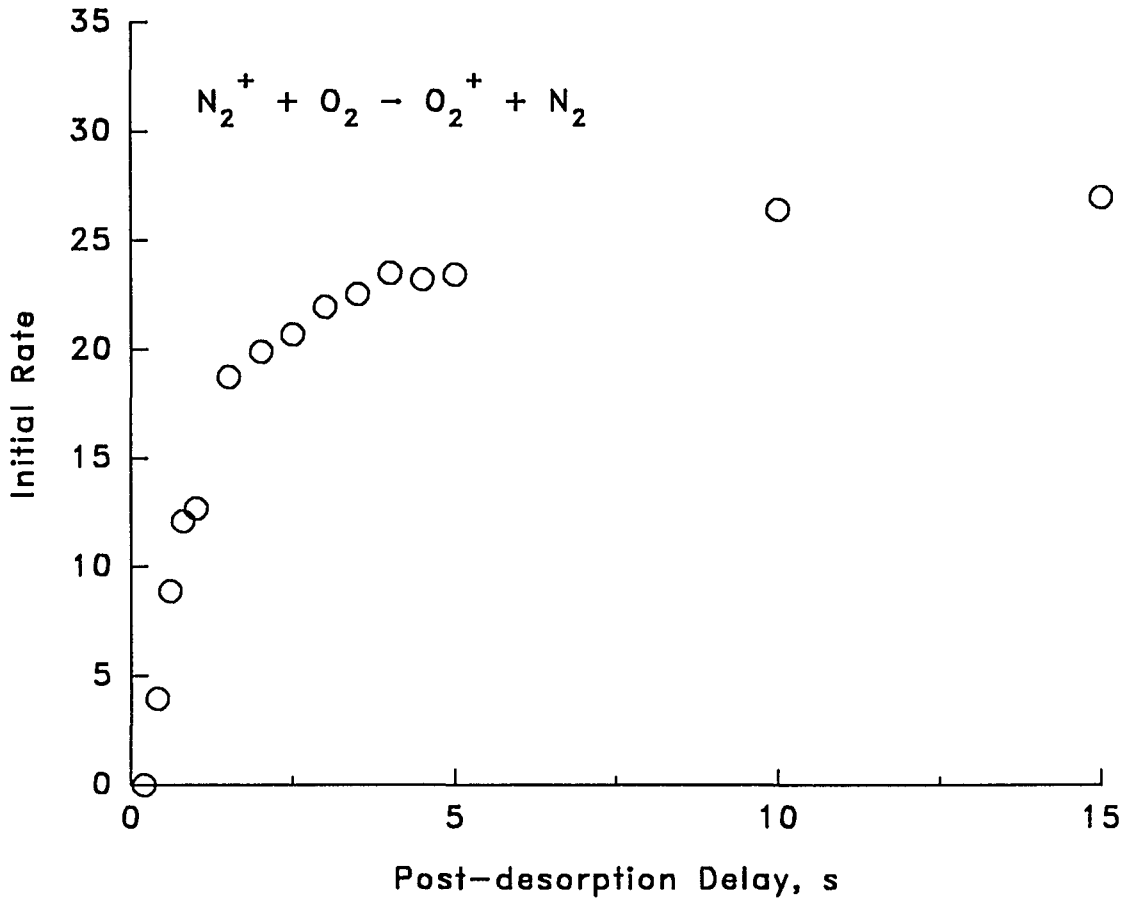

FIGURE 6.2: Oxygen Gettering Following Aluminum Cluster Desorption

Survey of Photodissociation and Oxidation Reactions

Past investigations[6.6,6.10] of the photodecomposition behavior of smaller (less than 10 atoms) aluminum cluster cations and anions have, in general, revealed broad absorption behavior in the visible region, with a transition to two-photon behavior occurring in the red.[6.10] Here these observations are extended for 3-23 atom aluminum cluster anions to the near infrared region at 1064 nm. All clusters except Al_{13}^- (which is predicted by the jellium model to be closed-shell and especially stable) absorb at 1064 nm, and aluminum atom loss predominates for most species. In general, the larger clusters (15 atoms or greater) require the absorption of two photons to dissociate and the smaller clusters require only one, the major exceptions being Al_6^- and Al_7^- which predominantly photodetach after sequential absorption of two photons, which necessitates a vibrational detachment mechanism. (Detached electrons were quantitated by scavenging with SF_6.) Detachment was also observed for Al_3^-, although experimental difficulties prevented the determination of the number of photons required (and it could well be borderline, since its electron affinity is about 1.4 to 1.5 eV—not too far above the 1.1 eV photon energy). The photodecomposition behavior of these clusters, including relative cross sections estimated by the methods of Appendix A is summarized in Table 6.1, below. Included for reference are the vertical electron affinities measured by Smalley and coworkers;[6.11] similar values were determined by Ganteför, et. al..[6.12] It should also be noted that Hettich[6.8] used charge exchange reactions to bracket the electron affinities of Al_n (n=3-13, 23) and found all but Al_3^- to have electron affinities between 1.89 and 2.30 eV (Al_3^- was less than 1.89 eV).

TABLE 6.1: 1064 nm Photodissociation Behavior of Al_n^-

n	# hν	Branching Fractions		rel. σ	E.A., eV
		n-1	e^-		
3	1 or 2	-	1	?	1.53
4	1	1	-	1	1.74
5	1	1	-	0.5	1.82
6	2	< 0.20	> 0.80	< 3.5	2.09
7	2	< 0.05	> 0.95	< 2.7	1.96
8	1	1	-	**1**	2.22
9	1 or 2	1	-	?	2.47
10	1	1	-	0.9	2.47
11	2	1	-	1.9	2.53
12	1 or 2	1	-	?	2.53
13	-	-	-	**0**	2.86
14	1	1	-	0.7	2.47
15	2	1	-	3.9	2.53
16	2	1	-	3.2	2.59
17	2	1	-	4.4	2.69
18	2	1	-	3.4	2.64
19	2	1	-	3.1	2.70
20	2	1	-	2.3	2.64
21	1 or 2	1	-	?	2.75
22	2	1	-	1.5	2.75
23	2	1	-	2	2.86

The oxidation reactions of these species were also surveyed, and were found to be in general agreement with the less detailed investigation of Hettich. A slight but significant even-odd alternation was observed in the relative reaction rates, with odd-atom clusters being slightly more stable with respect to oxidation than their even-atom counterparts. It was difficult to obtain absolute rate constants for these reactions because of the problem (described above) of oxygen gettering by desorbed aluminum neutrals. While pulsed-valve reagent introduction has been successfully used by Ridge to measure absolute rate constants, time constraints prohibited such difficult measurements here. Approximately, however, these reactions were found to be anywhere from about 3% efficient for the larger, even clusters to less than 0.5% efficient for the smaller odd clusters. This is consistent with the low sticking coefficients observed for O_2 on low-index aluminum crystal faces: 0.04 for the (111) and (110) surfaces and 0.008 for the (001) surface.

Al_n^- Oxidation Reactions

n ≤ 7:

$$Al_n^- + O_2 \longrightarrow \begin{cases} AlO_2^- \\ AlO^- \end{cases} \longrightarrow e^- \qquad \begin{matrix} (6.1.a) \\ (6.1.b) \end{matrix}$$

n = 8:

$$Al_8^- + O_2 \longrightarrow \begin{cases} Al_3^- \longrightarrow e^- \\ AlO_2^- \\ AlO^- \end{cases} \longrightarrow e^- \qquad \begin{matrix} (6.2.a) \\ (6.2.b) \\ (6.2.c) \end{matrix}$$

n ≥ 9:

$$Al_n^- + O_2 \xrightarrow{-2Al_2O} Al_{n-4}^{-*} \longrightarrow \begin{cases} Al_{n-5}^- & (6.3.a) \\ Al_{n-4}^- & (6.3.b) \\ (e^-) & (6.3.c) \\ (Al_{n-6}^-) & (6.3.d) \end{cases}$$

(Reaction 6.3.c occurs only for n = 10-12, since the Al_7^- and Al_6^- products will detach if sufficiently vibrationally excited. Reaction 6.3.d occurs only for Al_{19}^-, since its n-6 product is the especially stable Al_{13}^-.)

In summary, cluster anions with seven or fewer anions produce AlO_2^-, AlO^-, and detached electrons. Since the formation of both ions has been estimated to be from 5 to 7 eV exothermic, either may detach, and it was impossible to identify the precursor of the observed detached electrons. Clusters containing nine or more atoms (except the closed-shell Al_{13}^- and Al_{23}^- cluster anions, which were unreactive) reacted exclusively by loss of 2 Al_2O molecules from the intermediate, bound oxygen species. No oxygen-containing primary products were ever observed for these larger clusters. The resulting Al_{n-4}^- species was often left with enough residual internal energy to lose another aluminum atom (or in some cases, an electron). Jarrold has estimated that the oxidation of large aluminum cluster cations is about 7 eV exothermic.[6.15] For Al_8^-, all processes described above were observed. This behavior is summarized in the reactions shown below and in Table 6.2.

TABLE 6.2: Reactions of Al_n^- with Oxygen

n	Branching Fractions						e^- source	rel. rate
	n-4	n-5	n-6	e^-	AlO_2^-	AlO^-		
3	-	-	-	0.79	0.04	0.17	?	1
4	-	-	-	0.68	0.02	0.3	?	1.2
5	-	-	-	0.77	0.02	0.21	?	0.62
6	-	-	-	0.85	0.02	0.13	?	0.44
7	-	-	-	0.90	0.02	0.08	?	0.22
8	-	0.36	-	0.53	0.02	0.09	n-5	**1**
9	0.27	0.73	-	-	-	-	-	0.09
10	0.08	0.19	-	0.73	-	-	n-4	1.3
11	-	0.54	-	0.46	-	-	?	0.24
12	-	0.29	-	0.71	-	-	n-5	0.64
13	-	-	-	-	-	-	-	**0**
14	-	1.00	-	-	-	-	-	1.3
15	0.57	0.43	-	-	-	-	-	0.24
16	0.68	0.32	-	-	-	-	-	1.7
17	0.45	0.55	-	-	-	-	-	1.6
18	-	1.00	-	-	-	-	-	1.8
19	-	0.15	0.85	-	-	-	-	0.93
20	0.05	0.95	-	-	-	-	-	1.6
21	0.05	0.95	-	-	-	-	-	0.58
22	0.61	0.39	-	-	-	-	-	0.67
23	-	-	-	-	-	-	-	**0**

Oxidation and Relaxation of Vibrationally Excited Al_{16}^- and Al_{18}^-

The two-photon dissociation behavior observed for the larger cluster anions afforded the opportunity to study the effects of vibrational excitation on the cluster oxidation reactions. Al_{16}^- was chosen for its relatively large absorption cross section, its relatively rapid oxidation rate, and a branching ratio that should be a sensitive measure of the cluster's internal energy. Al_{18}^- was selected to verify the effects of vibrational excitation on the overall reaction rate, because of the certainty of forming the Al_{13}^- product without subsequent dissociation or detachment. (Its electron affinity is significantly higher than the electron affinities of its neighbors.) The clusters were isolated using SWIFT pulses to prevent residual translational excitement because the oxidation rates appear to be quite sensitive to the reactant kinetic energy. After a 1-2 second thermalization period in a bath of argon, a fraction of the clusters was photoexcited with a YAG laser pulse, and the observed extent of dissociation was used to estimate this excited fraction. The dissociated fragments were ejected with a SWIFT pulse and after a variable cooling delay the remaining clusters were allowed to react with a pulsed valve addition of O_2, optimized for 10-20 % product formation so that the initial branching ratio could be observed. As expected, branching into the Al_{n-5}^- product was observed to increase with excess internal energy, at the expense of Al_{n-4}^-. Relaxation curves in which the initial Al_{n-4}^- branching fraction is plotted as a function of cooling delay are shown for two different argon pressures in Figures 6.3 and 6.4, below.

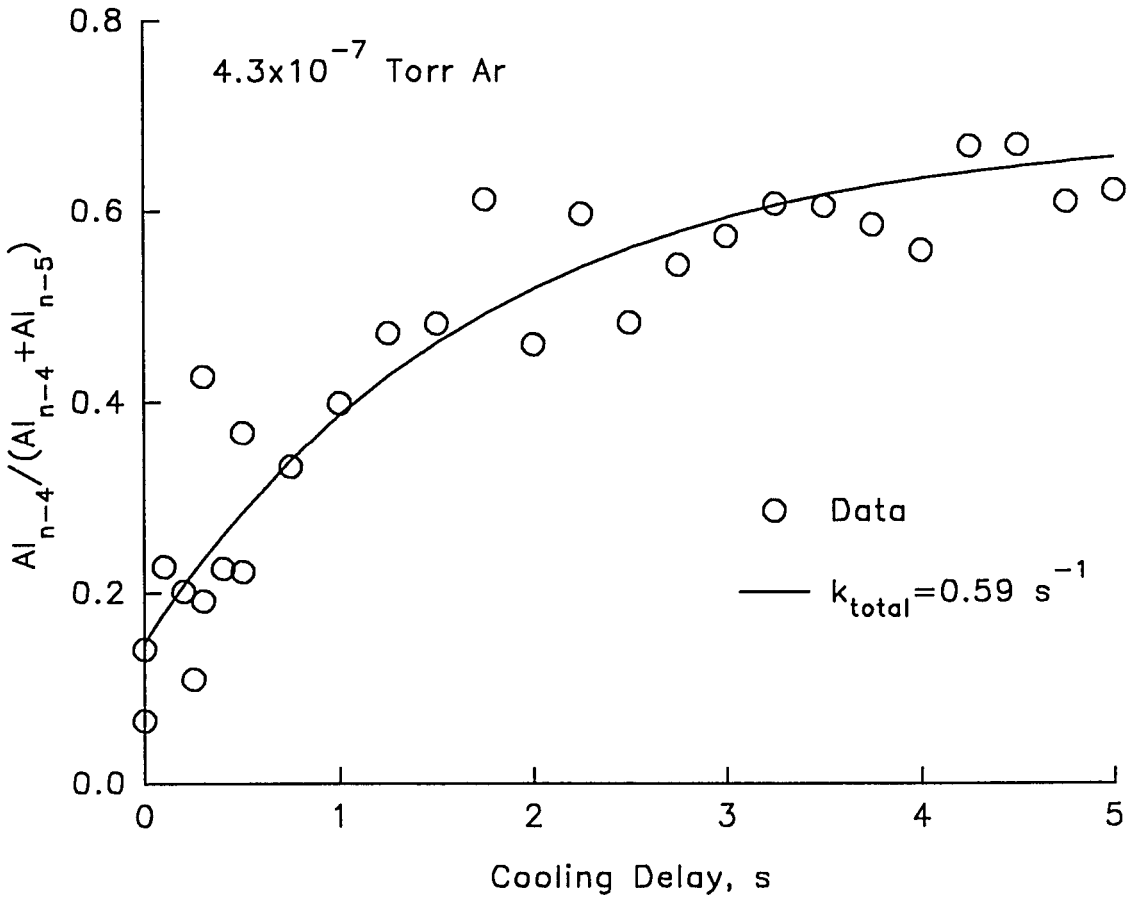

FIGURE 6.3: Oxidation Branching Relaxation Study of Al_{16}^- in 4.3×10^{-7} Torr Ar

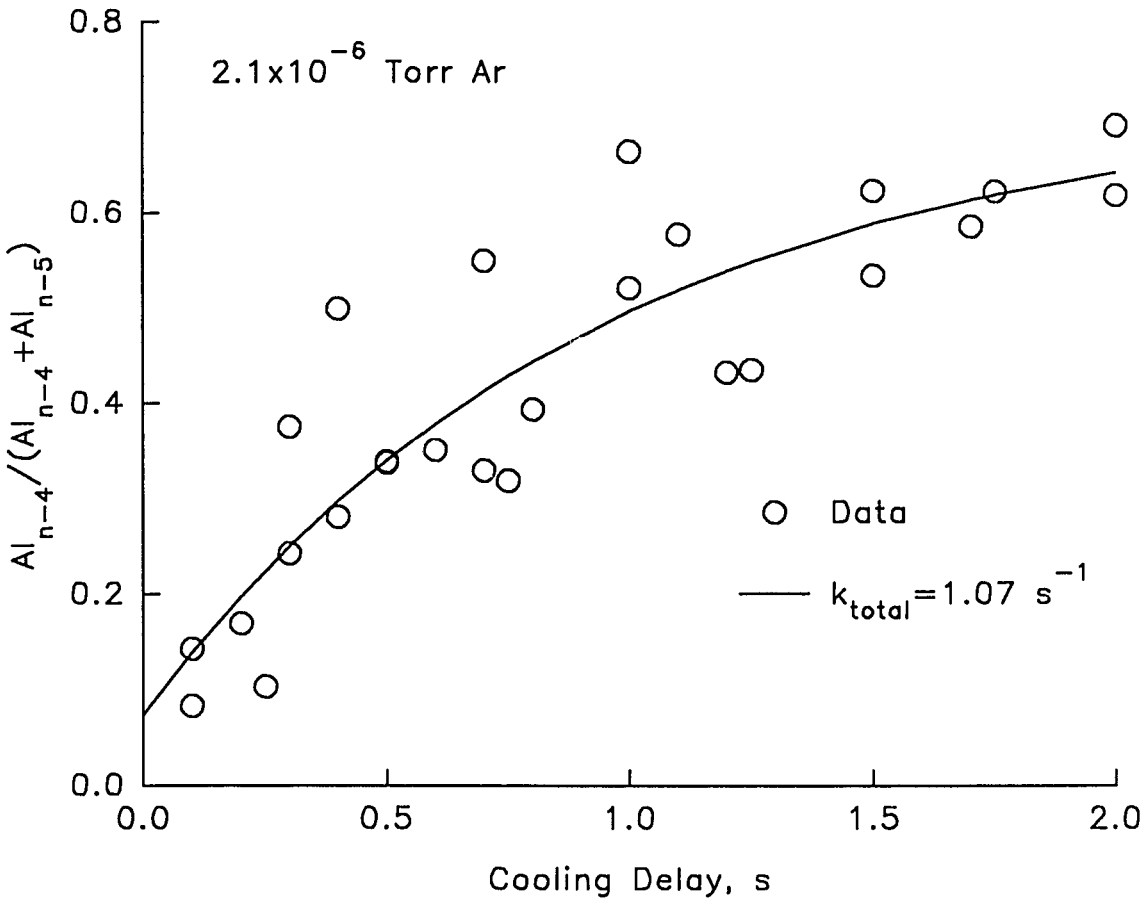

FIGURE 6.4: Oxidation Branching Relaxation Study of Al_{16}^- in 2.1×10^{-6} Torr Ar

Strictly speaking, these are not "branching" processes in the sense of competitive dissociation channels. Instead, the extent of Al_{n-5}^- formation depends on the amount of energy partitioned into the nascent Al_{n-4}^- cluster fragment after the loss of two Al_2O molecules. There are two sources of suprathermal internal energy in the Al_{n-4}^- fragment: the reaction exoergicity and any excess internal energy from the Al_n^- cluster, which will be largely and proportionately retained in the Al_{n-4}^- cluster. Loss of an additional aluminum atom can occur if the total internal energy of the Al_{n-4}^- cluster exceeds its dissociation energy. Again the exponential fit to these data is *ad hoc*; this measurement technique will be compared in Chapter 7 to those used for $Cr(CO)_5^-$.

In addition to altering the branching behavior, excess vibrational energy also decreases the overall oxidation rate. Carefully controlled experiments show that the oxidation rates of Al_{16}^- and Al_{18}^- decrease by factors of 2.5±1.0 and 5.0±2.0, respectively, upon the addition of one 1064 nm photon of excess internal energy to each. Figure 6.5, below, shows the return to the thermal rate constant as the cluster cools. This contrasts with the results obtained for the oxidation reactions of aluminum cluster cations, which were tentatively confirmed here for the anions, that the reaction rates increase with translational excitation. This nonequivalence of the effects of different forms of energy on the reaction rates means that the reactions are nonstatistical. This is explained by assuming that the vibrational energy, which is randomized throughout the cluster, does not efficiently couple into the transition state corresponding to dissociative chemisorption of the oxygen onto the cluster surface.[6.15] An activation barrier of 0.55 eV has been found from the collision energy dependence of the oxidation rate of Al_{25}^+.[6.9]

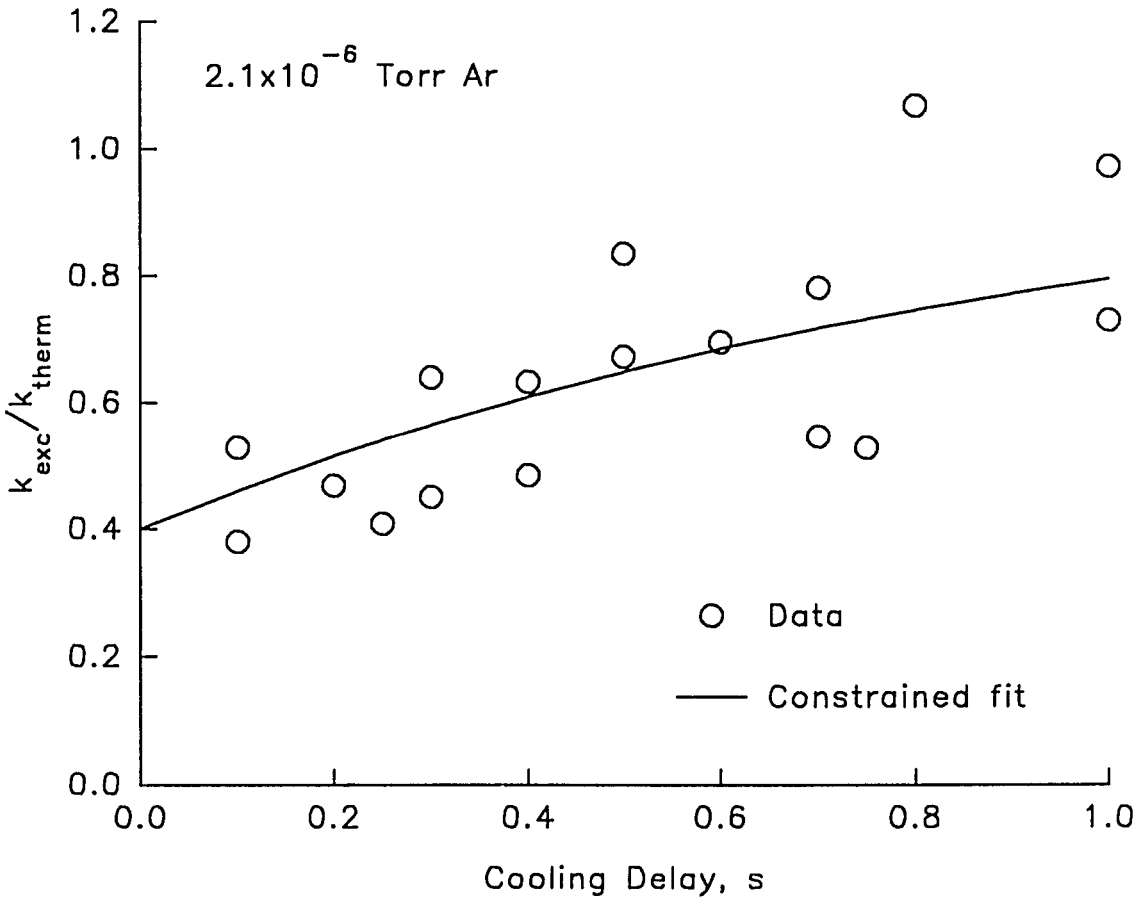

FIGURE 6.5: Initial Oxidation Rate versus Cooling Delay for Al_{16}^-

These energetic data are summarized below in Table 6.3. The radiative relaxation rate constant measured here, 0.47±0.10 s^{-1}, is among the lowest yet measured for this approximate energy regime, and probably reflects the lack of strongly-emitting, high-frequency modes in this cluster. This is discussed in more detail in the next Chapter. Also striking is the low efficiency with which Ar collisions remove vibrational energy from this cluster, which is quite at odds with the so-called "strong-collision hypothesis" for unimolecular reactions which states that species excited to a state continuum should be collisionally "deactivated" with near-unit efficiency. Even more surprising, however, are tentative results using SF_6 as a collisional quenching agent that show SF_6 to be only marginally better than Ar at collisionally quenching this cluster. The cluster frequencies must be low indeed for there to be poor overlap with the vibrational frequencies of SF_6!

TABLE 6.3: Kinetic Behavior of Vibrationally Excited Al_n^-

	$Al_n^- + O_2$			Relaxation		
	k_{therm}/k_{hot}	thermal X_{n-5}	hot X_{n-5}	k_{rad}, s^{-1}	k_{coll} (Ar), $cm^3 \cdot s^{-1}$	eff*
Al_{16}^-	2.5 ± 1.0	0.32 ± 0.04	0.90 ± 0.08	0.47 ± 0.10	(9 ± 3) × 10^{-12}	1.7 ± 0.4
Al_{18}^-	5.0 ± 2.0	1.0	1.0	-	-	-

* k_L for Al_{16}^-/Ar = 4.96×10^{-10} $cm^3 \cdot s^{-1}$.

CHAPTER 7:

RELAXATION MODELING STUDIES: COMPARISON AND CONTRAST OF THE $Cr(CO)_5^-$ AND Al_{16}^- ANIONS

This final Chapter develops a detailed model of radiative relaxation by polyatomic molecules and uses this model to rationalize the differences observed between the radiative lifetimes of $Cr(CO)_5^-$ and Al_{16}^-. An effective transition dipole moment is also computed for an "average" Al_{16}^- vibrational mode. Finally, this Chapter critically examines the techniques used for radiative lifetime measurements and outlines the conditions under which each method is most useful.

It is appropriate at this point to note that the *cgs* system of units is used throughout this Chapter, both by historical precedence and for convenience. An important difference between the *cgs* and MKSA systems involves the definition of charge. In the MKSA system charge is expressed in coulombs (C), while in the *cgs* system charge is defined in terms of Coulomb's Law and is expressed in electrostatic units (esu), which have dimensions $(m^{1/2}l^{3/2}t^{-1})$. To convert an equation given in *cgs* units to one given in MKSA units, replace every occurrence of charge q with $q\cdot(4\pi\epsilon_0)^{-1/2}$.

It should also be mentioned that the wavenumber (cm^{-1}) is used throughout this Chapter both as a unit of frequency ($\bar{\nu}$) and as a unit of energy (E). Frequency in reciprocal seconds (ν) is proportional to frequency in wavenumbers ($\bar{\nu}$) by the speed of light in a vacuum (c): ν (s^{-1}) = $\bar{\nu}$ (cm^{-1}) · c ($cm\cdot s^{-1}$). Likewise, Planck's constant can be recast (if necessary) for frequency in wavenumbers: $h = 1.99 \times 10^{-16}$ "erg·cm." (This form of Planck's

constant should not be used in the equations given below for spontaneous emission, however.) Far more useful is the conversion between energy in "wavenumbers" and in kcal/mol: there are 350. cm^{-1} in 1.00 kcal/mol. The state-counting calculations performed in this Chapter used a "grain" (see Appendix B) of 35 cm^{-1}, or 0.1 kcal/mol.

Einstein Spontaneous Emission Coefficients

The probability (rate constant) for spontaneous emission is expressed by the Einstein *A* coefficient, which for a single harmonic oscillator transition originating in level *n* and terminating in level $n' = n\text{-}1$ can be written as:[7.1]

$$A_{nn'} = \frac{64\pi^4}{3hc^3}\nu^3 |\mu_{nn'}|^2 \tag{7.1}$$

in which ν is the frequency of the oscillator and $|\mu_{nn'}|^2$ (in $esu^2 \cdot cm^2$) is the squared transition dipole matrix element for the given transition. Since one property of the harmonic oscillator model is that the $n \rightarrow n'$ transition is *n* times as intense as the $1 \rightarrow 0$ transition,[7.2] Equation 7.1 can be rewritten as (note also the conversion to frequency in wavenumbers):

$$A_{nn'} = \frac{64\pi^4}{3h}\bar{\nu}^3 n|\mu_{10}|^2 \tag{7.2}$$

Since the absolute emission intensities are not known (or else these measurements would be unnecessary), relative rate constants will be used throughout this modeling work. The rate constant for spontaneous emission from the *i*th vibrational mode of a polyatomic molecule at a particular internal energy E is proportional to three factors:

$$k_{em,i}(E) \propto \bar{\nu}_i^3 \cdot \langle n_i(E) \rangle \cdot |\mu_{10}|_i^2 \tag{7.3}$$

A complication arises for polyatomics in that emission from a given mode can only occur if that degree of freedom is occupied by one or more quanta, which is represented in Equation 7.3 by $\langle n_i(E) \rangle$ (the average number of quanta present in the *i*th mode at the given

internal energy E, which includes the possibility that the mode is not occupied). As discussed in Appendix B, a modified version of the Beyer-Swinehart state-counting algorithm can be used to compute $\langle n_i(E) \rangle$ (within the ergodic hypothesis) if the vibrational frequencies of the molecule are known. (The ergodic hypothesis states that each possible way of partitioning the internal energy of a molecule is equally probable.)

Each infrared-active vibrational mode of a polyatomic molecule can emit in parallel, so that the total rate constant for spontaneous emission at a given internal energy is a sum over all vibrational degrees of freedom of the molecule:

$$k_{em}(E) = \sum_i k_{em,i}(E) \propto \sum_i \bar{\nu}_i^3 \cdot \langle n_i(E) \rangle \cdot |\mu_{10}|_i^2 \qquad (7.4)$$

Note that $k_{em}(E)$ represents the probability that *any* photon will be emitted from the molecule; it says nothing about the amount of energy removed upon an emission event, which is of course proportional to the frequency of the emitted photon. The average emitted photon energy (the expected value of $\bar{\nu}(E)$) can be found by weighting the frequency of each mode by the normalized probability that emission will occur from that mode:

$$\langle \bar{\nu}(E) \rangle = \sum_i \frac{k_{em,i}(E)}{\sum_i k_{em,i}(E)} \bar{\nu}_i = \sum_i \frac{k_{em,i}(E)}{k_{em}(E)} \bar{\nu}_i \qquad (7.5)$$

The *rate* at which energy is removed from a given vibrational mode is equal to the spontaneous emission rate constant times the frequency (energy) of the emitted photon, yielding a fourth-power dependence on the frequency of the vibrational mode. The overall rate of energy disposal from the molecule is again a sum over all modes:

$$-\left(\frac{dE}{dt}\right) = -\sum_i \left(\frac{dE}{dt}\right)_i = \sum_i k_{em,i}(E)\cdot\bar{\nu}_i \propto \sum_i \bar{\nu}_i^4 \cdot \langle n_i(E)\rangle \cdot |\mu_{10}|_i^2 \qquad (7.6)$$

The $\bar{\nu}^3$ dependence of the spontaneous emission rate and the $\bar{\nu}^4$ dependence of the energy disposal rate guarantee that the highest frequency modes will dominate the emission spectrum and will be the primary contributors to the energy disposal rate when the molecule contains enough internal energy for these modes to be adequately occupied.[7.3] These points will be further developed and illustrated graphically in the section on relaxation efficiency matrices.

Vibrational Frequency Estimation

Before the radiative relaxation of any molecule can be modeled at the level of detail required here, a credible estimate of the vibrational frequencies must be made. Since the very low ion number densities in most gas-phase apparatus preclude their direct measurement, the usual approach is to adopt the vibrational frequencies of a similar neutral molecule. Here, the $Cr(CO)_5^-$ frequencies are taken as those of the corresponding 27 (out of 33) vibrational modes of $Cr(CO)_6$, except that the high-frequency CO stretching frequencies are adjusted downward by 100 cm^{-1} to account for the decrease in CO bond order due to additional π-backbonding from the extra electron on the metal center. These assumptions are supported by the extensive literature on the infrared and Raman spectroscopy of transition metal carbonyl complexes, including both ionic (condensed-phase) and coordinatively unsaturated (gas- and condensed-phase) species. The vibrational frequencies used for this work are listed below:[7.4]

TABLE 7.1: $Cr(CO)_5^-$ Vibrational Frequencies

$\bar{\nu}$, cm^{-1}	deg.	Description	$\bar{\nu}$, cm^{-1}	deg.	Description
67	3	δ(CCrC)	440	2	ν(CrC)
89	3	δ(CCrC)	510	3	δ(CrCO)
97	1	δ(CCrC)	532	3	δ(CrCO)
364	3	δ(CrCO)	668	1	δ(CrCO)
379	1	ν(CrC)	1900	3	ν(CO)
390	2	ν(CrC)	1966	2	ν(CO)

Ultimately, the results of this Chapter are not sensitive to the precise frequencies used in these models; the same qualitative conclusions would be made even if the frequencies were collected into three or four groups.

The scarcity of vibrational frequency data for aluminum clusters (neutral or ionic) with more than a few atoms forces the use of an entirely different approach to estimate the vibrational frequencies of Al_{16}^-. Jarrold has used a modified Debye model to select aluminum cluster cation vibrational frequencies for RRKM calculations;[7.5] this method was duplicated here and is described below. Recall that the bulk Debye model invokes a density of vibrational modes that is a quadratic function of frequency up to a cutoff or "Debye" frequency, $\bar{\nu}_D$. The solid-state literature generally reports the "Debye temperature" θ_D, which is equal to $h\bar{\nu}_D/k$. For aluminum, $\theta_D = 428$ K ($\bar{\nu}_D = 297.48$ cm^{-1}).[7.6]

The following equation is used to express the Debye frequency for the Al_n cluster in terms of the bulk Debye frequency:

$$\bar{\nu}_{Dn} = \bar{\nu}_D (1 - n^{-1/3})^a \qquad (7.7)$$

in which $\bar{\nu}_{Dn}$ is the cutoff frequency for the Al_n cluster, $\bar{\nu}_D$ is the bulk Debye frequency, and a is selected so that $\bar{\nu}_{D2}$ equals the (known) frequency of the dimer, 350.01 cm^{-1}.[7.7] Consecutive solutions to this equation yield $a = -0.10302$ and $\bar{\nu}_{D16} = 313.38$ cm^{-1}. The individual vibrational frequencies $\bar{\nu}_i$ are then found from:

$$\bar{\nu}_i = \left(\frac{i - 1/2}{3n - 6} \bar{\nu}_{Dn}^3 \right)^{1/3} \qquad (7.8)$$

Jarrold has already discussed the nature of this approximation for similar calculations.[7.5] Again, the precise frequencies are unimportant; all that is really needed is a frequency distribution that yields approximately correct sums and densities of states. It is certain that this model does not accurately describe the frequency distribution of an intermediate-sized cluster, given that it is not rigorously correct for the bulk. It is anticipated that the frequency distribution for a cluster would be far less smooth, but the Debye model will be used here in lieu of either a better model or actual frequency data. Table 7.2 lists the calculated frequencies:

TABLE 7.2: Al_{16}^- Vibrational Frequencies from the Debye Model, cm^{-1}

71.6	176.5	219.8	250.7	275.4	296.3
103.2	184.0	224.8	254.5	278.6	299.1
122.4	190.9	229.5	258.2	281.7	301.8
136.9	197.4	234.1	261.8	284.7	304.4
148.8	203.5	238.4	265.4	287.7	307.0
159.1	209.2	242.7	268.8	290.6	309.6
168.3	214.7	246.7	272.1	293.5	312.1

Figure 7.1, below, shows that these frequencies indeed follow a quadratic distribution.

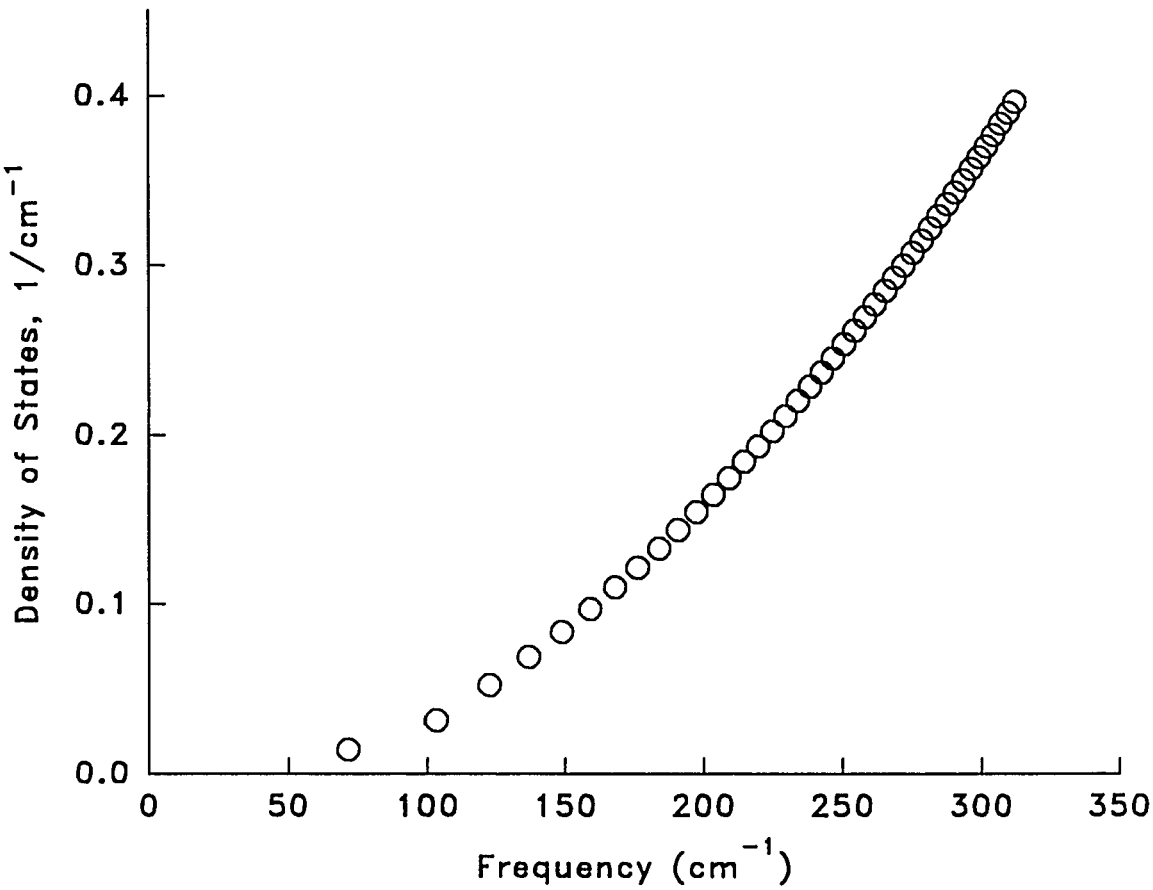

FIGURE 7.1: Density of Al_{16}^- Vibrational Modes from the Debye Model

Relaxation Efficiency Matrices

Once a molecule's vibrational frequencies have been chosen, the average number of quanta in each vibrational mode as a function of internal energy may be calculated using the modification of the Beyer-Swinehart algorithm developed in Appendix B. While harmonic oscillators have been assumed here for the sake of simplicity, the extended Beyer-Swinehart algorithm readily accommodates anharmonic degrees of freedom if the energy level spacing (potential surface) is known. However, anharmonic oscillator capabilities have not been coded in the program included in Appendix B, since essentially no quantitative information is available for the relevant potential surfaces.

Figures 7.2 through 7.4 depict the results of these state-counting calculations for $Cr(CO)_5^-$ and Al_{16}^-. Figure 7.2 shows graphically that the occupation probability for a mode (in this case the 668 cm^{-1} mode of $Cr(CO)_5^-$) is approximately equal to the average number of quanta in the mode for energies below which levels higher than the first are significantly populated. This figure also shows that, once there is enough energy in the molecule for a given mode to be competitively populated, the average number of quanta in the mode is roughly proportional to the molecules internal energy. In each of Figures 7.3 and 7.4, the average number of quanta in each vibrational mode is plotted as a function of internal energy. In Figure 7.3, the plots for three lowest frequencies of $Cr(CO)_5^-$ are compressed by a factor of four and those of the two highest frequencies expanded by a factor of twenty in order to display the entire range of mode occupation behavior in $Cr(CO)_5^-$on the same axes. Note that the average number of quanta in the CO stretches is less than 0.2 for all energies

shown (up to about 140% of the dissociation threshold), and that the stretches do not become significantly occupied until three to five times the energy at which they may first be populated (this is because there are already about 5×10^6 other states available by 2000 cm^{-1}). Notice also that the average number of quanta in the lowest-frequency modes climbs very steeply until the intermediate-frequency modes begin to contribute to the sum of states, and has already exceeded the scale of the graph (but for the factor-of-four compression) by about 6000 cm^{-1}. Finally, no scale factor was required at all for the Al_{16}^- graph (Figure 7.4), since the lower, relatively closely-spaced frequencies of Al_{16}^- each make a significant contribution to the overall state count (which is also *fifteen orders of magnitude* higher than that of $Cr(CO)_5^-$ by 10,000 cm^{-1}) even at modest internal energies; the energy is therefore more evenly distributed throughout the molecule.

One last assumption has yet to be made—that concerning the relative squared transition dipole moment matrix elements. Again in the absence of data to the contrary, all of the $|\mu_{10}|_i^2$ values will be assumed equal and for convenience set to unity. This is clearly an unrealistic assumption, since not all vibrational modes will be infrared active. However, these species may possess low symmetry (as in the hypothesized Jahn-Teller distorted trigonal bipyramidal $Cr(CO)_5^-$ complex) and are at these internal energies highly stereochemically nonrigid, so it is likely that the infrared selection rules attributable to symmetric, rigid structures have completely broken down. The assumption of equal transition dipole moments is in any case a convenient basis of discussion; different modes can be turned on or off as appropriate to yet more detailed models.

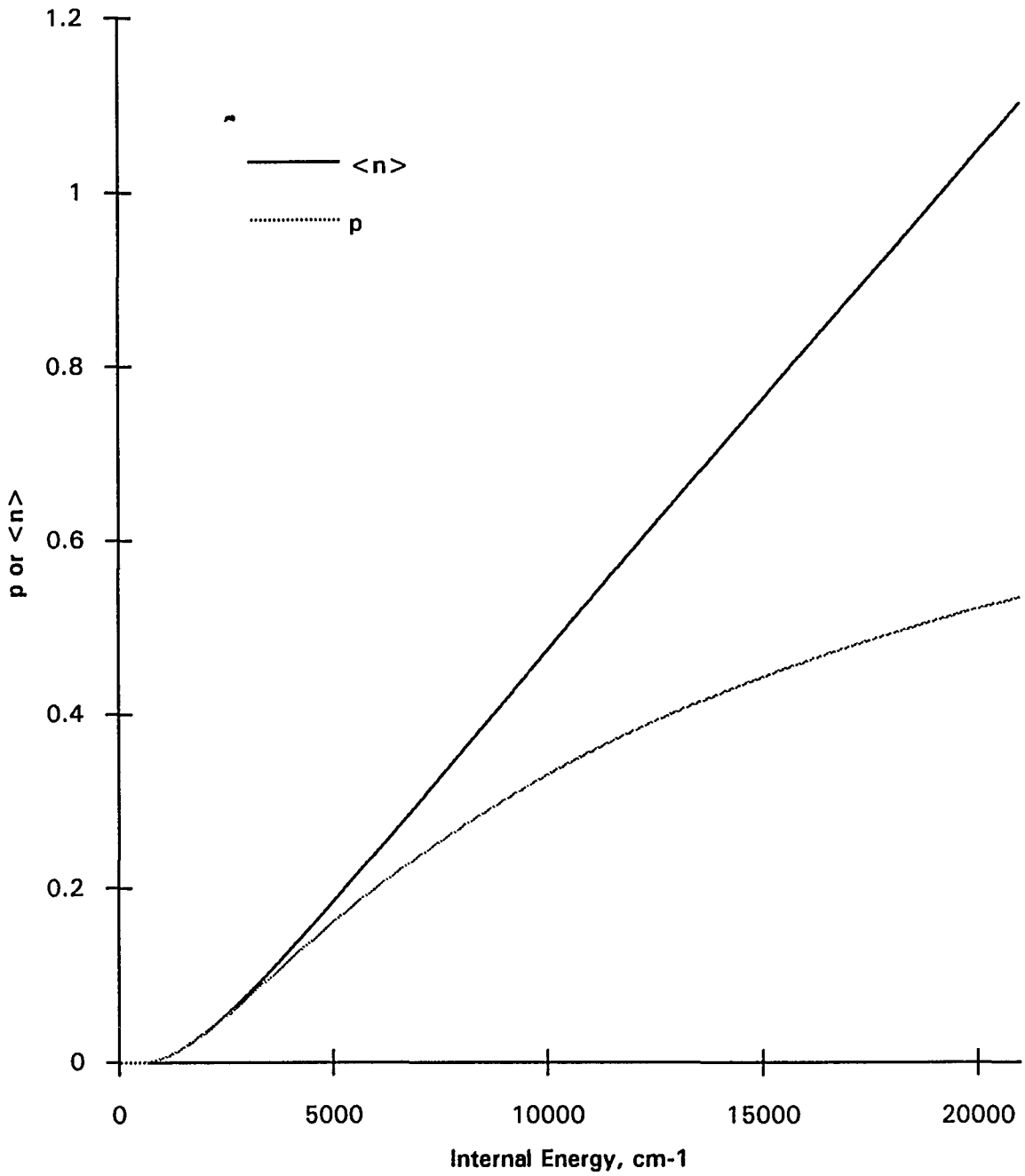

FIGURE 7.2: $Cr(CO)_5^-$ 668 cm^{-1} Mode Occupation Probability and Average Level

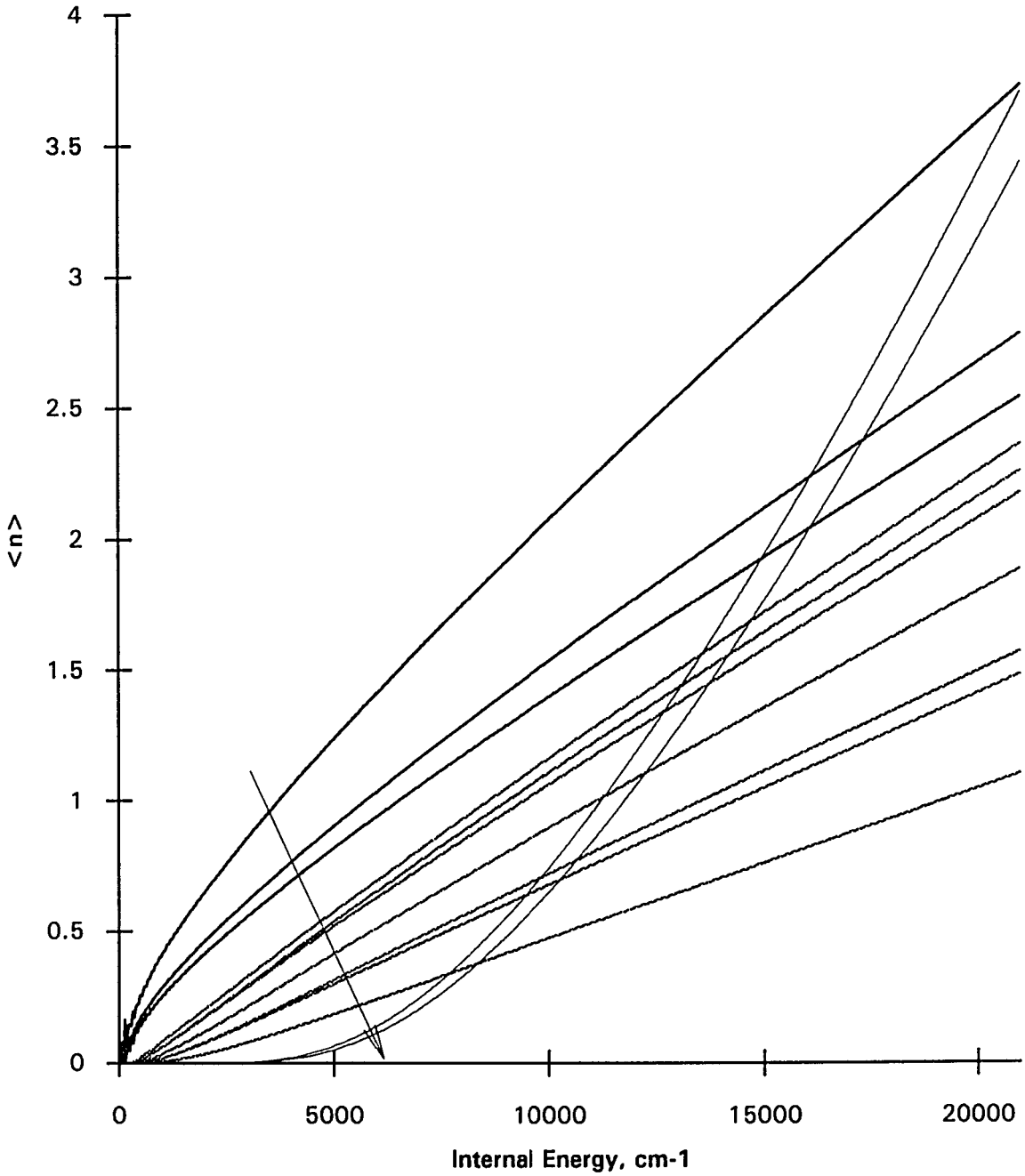

FIGURE 7.3: $Cr(CO)_5^-$ Mode Occupation versus Internal Energy
(The arrow points in the direction of increasing frequency.)

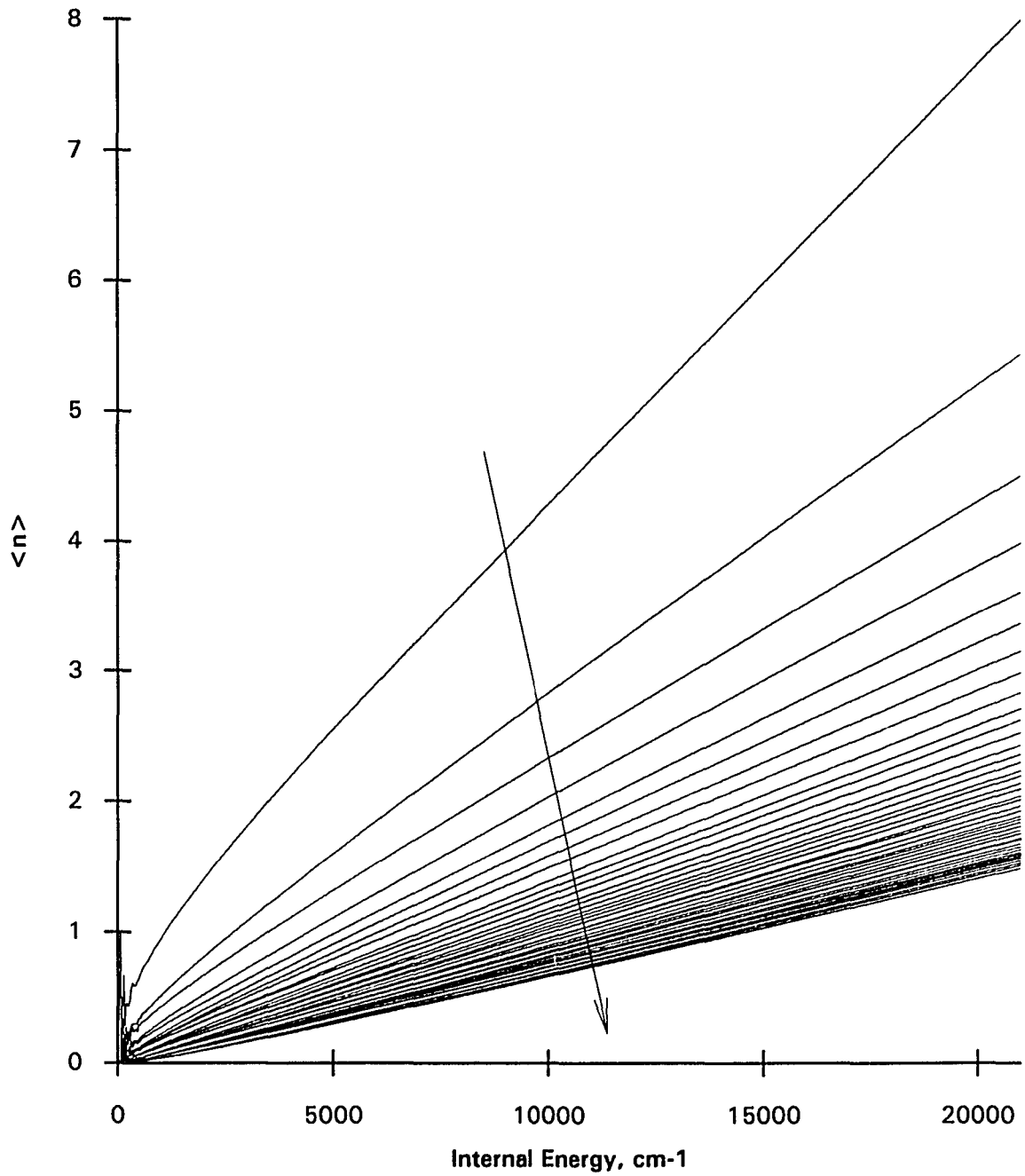

FIGURE 7.4: Al_{16}^- Mode Occupation versus Internal Energy
(The arrow points in the direction of increasing frequency.)

Once frequencies and transition dipole moments have been selected and the appropriate state-counting calculations have been made, the results can be plugged into what will be termed a "relaxation efficiency matrix," which is simply a tabular (spreadsheet) calculation, at a given internal energy, of the sums in Equations 7.4 through 7.6. Tables 7.3 and 7.4 give examples for $Cr(CO)_5^-$: one at 11,760 cm^{-1} (thermal plus one 1064 nm photon) and one at 7,875 cm^{-1} (one CO stretch emission above the one-photon threshold), and Table 7.5 gives an example for Al_{16}^- at 14,175 cm^{-1} (thermal plus one photon). The $Cr(CO)_5^-$ matrices have an extra column for the degeneracy at each frequency; otherwise, the tables are identical. In order, the columns of each table list the frequency, [the degeneracy], the relative squared transition dipole moment matrix element (assumed unity), the average number of quanta in the mode (calculated by the Beyer-Swinehart algorithm), the relative frequency cubed, the relative energy disposal rate (the product of all previous columns), the normalized energy disposal efficiency, the relative spontaneous emission rate constant (the product of all columns prior to the *d*E/*dt* column *except* the first), the normalized emission rate constant, and finally, the contribution of that mode to the average emitted photon energy (the emission fraction times the mode frequency).

The fractional contribution that each mode (or degenerate group of modes) makes to the overall energy disposal rate is shown in the columns labeled $X_{eff,\,i}$, and the probability that an emitted photon will have frequency $\bar{\nu}_i$ (the fraction of the time each mode or degenerate group of modes emits) is listed in the columns labeled $X_{em,\,i}$. These results clearly show that the highest frequency modes dominate both the emission spectrum and especially the disposal of excess internal energy, despite their much lower occupation

probability compared to their lower-frequency counterparts. The energy disposal rate drops sharply when the excess internal energy is too low for the highest frequency modes to be "adequately" populated. (However, even 1% is usually sufficient—see $Cr(CO)_5^-$ at 7875 cm^{-1}, for which each CO stretch accounts for roughly 14-15% of the total energy disposal rate despite being populated only about 0.6-0.8% of the time.)

TABLE 7.3: $Cr(CO)_5^-$ Relaxation Efficiency Matrix at 11,760 cm^{-1}

(4.74×10^{16} total states)

$\tilde{\nu}_i$	deg_i	rel $\lvert\mu_{10}\rvert_i^2$	$\langle n_i \rangle$	rel $\tilde{\nu}_i^3$	rel $(dE/dt)_i$	X_{eff}	rel $k_{em,i}$	$X_{em,i}$	$\langle \tilde{\nu}_i \rangle$
67	3	1	9.4096	1.0	1.00	0.0001	1.00	0.0025	0.17
89	3	1	6.9721	2.3	2.31	0.0003	1.74	0.0043	0.38
97	1	1	6.3555	3.0	0.99	0.0001	0.68	0.0017	0.16
364	3	1	1.3601	160.4	125.92	0.0162	23.18	0.0576	20.96
379	1	1	1.2983	181.0	47.09	0.0061	8.32	0.0207	7.84
390	2	1	1.2451	197.2	101.27	0.0131	17.40	0.0432	16.86
440	2	1	1.0596	283.2	139.63	0.0180	21.26	0.0528	23.23
510	3	1	0.8599	441.0	306.80	0.0396	40.30	0.1001	51.06
532	3	1	0.8090	500.6	341.76	0.0441	43.04	0.1069	56.88
668	1	1	0.5747	991.1	201.17	0.0260	20.18	0.0501	33.48
1900	3	1	0.0561	22805.3	3855.73	0.4975	135.96	0.3377	641.70
1966	2	1	0.0500	25265.4	2626.29	0.3389	89.50	0.2223	437.09
				sums =	7749.97	1.0000	402.58	1.0000	1289.82

TABLE 7.4: $Cr(CO)_5^-$ Relaxation Efficiency Matrix at 7875 cm^{-1}

(7.44×10^{13} total states)

$\tilde{\nu}_i$	deg_i	rel $\lvert\mu_{10}\rvert_i^2$	$\langle n_i \rangle$	rel $\tilde{\nu}_i^3$	rel $(dE/dt)_i$	X_{eff}	rel $k_{em,i}$	$X_{em,i}$	$\langle \tilde{\nu}_i \rangle$
67	3	1	6.9258	1.0	1.00	0.0003	1.00	0.0039	0.26
89	3	1	5.1012	2.3	2.29	0.0006	1.73	0.0068	0.60
97	1	1	4.6415	3.0	0.98	0.0002	0.68	0.0027	0.26
364	3	1	0.9174	160.4	115.40	0.0292	21.24	0.0832	30.29
379	1	1	0.8706	181.0	42.90	0.0108	7.58	0.0297	11.26
390	2	1	0.8357	197.2	92.35	0.0233	15.87	0.0622	24.24
440	2	1	0.6946	283.2	124.36	0.0314	18.94	0.0742	32.64
510	3	1	0.5498	441.0	266.51	0.0673	35.01	0.1372	69.95
532	3	1	0.5181	500.6	297.37	0.0751	37.45	0.1467	78.05
668	1	1	0.3493	991.1	166.12	0.0420	16.66	0.0653	43.60
1900	3	1	0.0185	22805.3	1727.50	0.4365	60.92	0.2387	453.44
1966	2	1	0.0157	25265.4	1120.40	0.2831	38.18	0.1496	294.09
				sums =	3957.18	1.0000	255.26	1.0000	1038.69

TABLE 7.5: Al_{16}^- Relaxation Efficiency Matrix at 14,175 cm^{-1}

(3.47×10^{28} total states)

$\bar{\nu}_i$	rel $\lvert\mu_{10}\rvert_i^2$	$\langle n_i \rangle$	rel $\bar{\nu}_i^3$	rel $(dE/dt)_i$	X_{eff}	rel $k_{em,i}$	$X_{em,i}$	$\langle \bar{\nu}_i \rangle$
71.6	1	5.6944	1.000	1.00	0.0007	1.00	0.0026	0.18
103.2	1	3.8301	2.994	2.90	0.0021	2.01	0.0052	0.54
122.4	1	3.1583	4.996	4.74	0.0034	2.77	0.0072	0.88
136.9	1	2.7803	6.990	6.53	0.0047	3.41	0.0088	1.21
148.8	1	2.5011	8.976	8.19	0.0059	3.94	0.0102	1.52
159.1	1	2.3327	10.972	9.99	0.0072	4.49	0.0116	1.85
168.3	1	2.1802	12.987	11.69	0.0084	4.97	0.0129	2.16
176.5	1	2.0630	14.979	13.38	0.0096	5.43	0.0140	2.48
184.0	1	1.9394	16.971	14.85	0.0106	5.78	0.0150	2.75
190.9	1	1.8550	18.953	16.46	0.0118	6.17	0.0160	3.05
197.4	1	1.7917	20.956	18.18	0.0130	6.59	0.0171	3.37
203.5	1	1.7255	22.959	19.77	0.0142	6.96	0.0180	3.66
209.2	1	1.6538	24.943	21.17	0.0152	7.24	0.0187	3.92
214.7	1	1.6038	26.962	22.77	0.0163	7.59	0.0196	4.22
219.8	1	1.5565	28.930	24.28	0.0174	7.91	0.0205	4.50
224.8	1	1.5102	30.949	25.77	0.0185	8.21	0.0212	4.77
229.5	1	1.4826	32.931	27.48	0.0197	8.57	0.0222	5.09
234.1	1	1.4460	34.951	29.02	0.0208	8.88	0.0230	5.37
238.4	1	1.4137	36.913	30.51	0.0219	9.16	0.0237	5.65
242.7	1	1.3654	38.947	31.65	0.0227	9.34	0.0242	5.86
246.7	1	1.3563	40.904	33.57	0.0240	9.74	0.0252	6.22
250.7	1	1.3209	42.926	34.86	0.0250	9.96	0.0258	6.46
254.5	1	1.2868	44.908	36.07	0.0258	10.15	0.0262	6.68
258.2	1	1.2598	46.895	37.41	0.0268	10.37	0.0268	6.93
261.8	1	1.2491	48.884	39.21	0.0281	10.72	0.0277	7.26
265.4	1	1.2280	50.929	40.71	0.0292	10.98	0.0284	7.54
268.8	1	1.2075	52.911	42.12	0.0302	11.22	0.0290	7.80
272.1	1	1.1826	54.884	43.32	0.0310	11.40	0.0295	8.02
275.4	1	1.1647	56.905	44.77	0.0321	11.64	0.0301	8.29
278.6	1	1.1377	58.912	45.80	0.0328	11.77	0.0304	8.48
281.7	1	1.1369	60.901	47.84	0.0343	12.16	0.0315	8.86
284.7	1	1.1122	62.867	48.82	0.0350	12.28	0.0318	9.04
287.7	1	1.0960	64.875	50.17	0.0359	12.48	0.0323	9.29
290.6	1	1.0753	66.857	51.24	0.0367	12.62	0.0327	9.49
293.5	1	1.0625	68.879	52.68	0.0377	12.85	0.0332	9.76
296.3	1	1.0561	70.869	54.39	0.0390	13.14	0.0340	10.07
299.1	1	1.0386	72.897	55.54	0.0398	13.30	0.0344	10.29
301.8	1	1.0327	74.889	57.25	0.0410	13.58	0.0351	10.60
304.4	1	1.0209	76.841	58.57	0.0419	13.78	0.0356	10.85
307.0	1	1.0015	78.827	59.44	0.0426	13.86	0.0359	11.01
309.6	1	0.9875	80.847	60.62	0.0434	14.02	0.0363	11.23
312.1	1	0.9712	82.821	61.57	0.0441	14.12	0.0365	11.40
			sums =	1396.31	1.0000	386.61	1.0000	258.60

If these calculations are repeated at a series of internal energies, the relative overall energy disposal rate and the relative overall spontaneous emission rate constant (both in arbitrary units), and the absolute average emitted photon may be plotted as a function of internal energy. Such plots are shown for $Cr(CO)_5^-$ in Figure 7.5 and for Al_{16}^- in Figure 7.6. The most striking difference between these graphs is the compound shape of the $Cr(CO)_5^-$ average emitted photon curve contrasted to the nearly flat curve for Al_{16}^-. Also prominent is the curvature of the $Cr(CO)_5^-$ dE/dt plot. The slope of this dE/dt versus E curve (shown in arbitrary units Figure 7.5 as a light line) is the radiative relaxation rate constant k_{rad}, which is still increasing with internal energy beyond 15,000 cm^{-1} (or roughly the dissociation threshold of 44 kcal/mol[7,8])! On the other hand, the radiative rate constant for Al_{16}^- (the slope of the dE/dt versus E curve in Figure 7.6) is almost entirely independent of energy. Again, the reason for this difference lies in the population of the efficiently-quenching high-frequency CO stretching modes of $Cr(CO)_5^-$, which only begin to be populated competitively above about 15,000 cm^{-1}, in the same region that the average emitted photon curve levels off. Since these modes (when "turned on") are responsible for the majority of the radiative energy disposal from $Cr(CO)_5^-$ (over 80% at 11,760 cm^{-1} as per Table 7.3), the energy disposal rate falls off at lower energies.

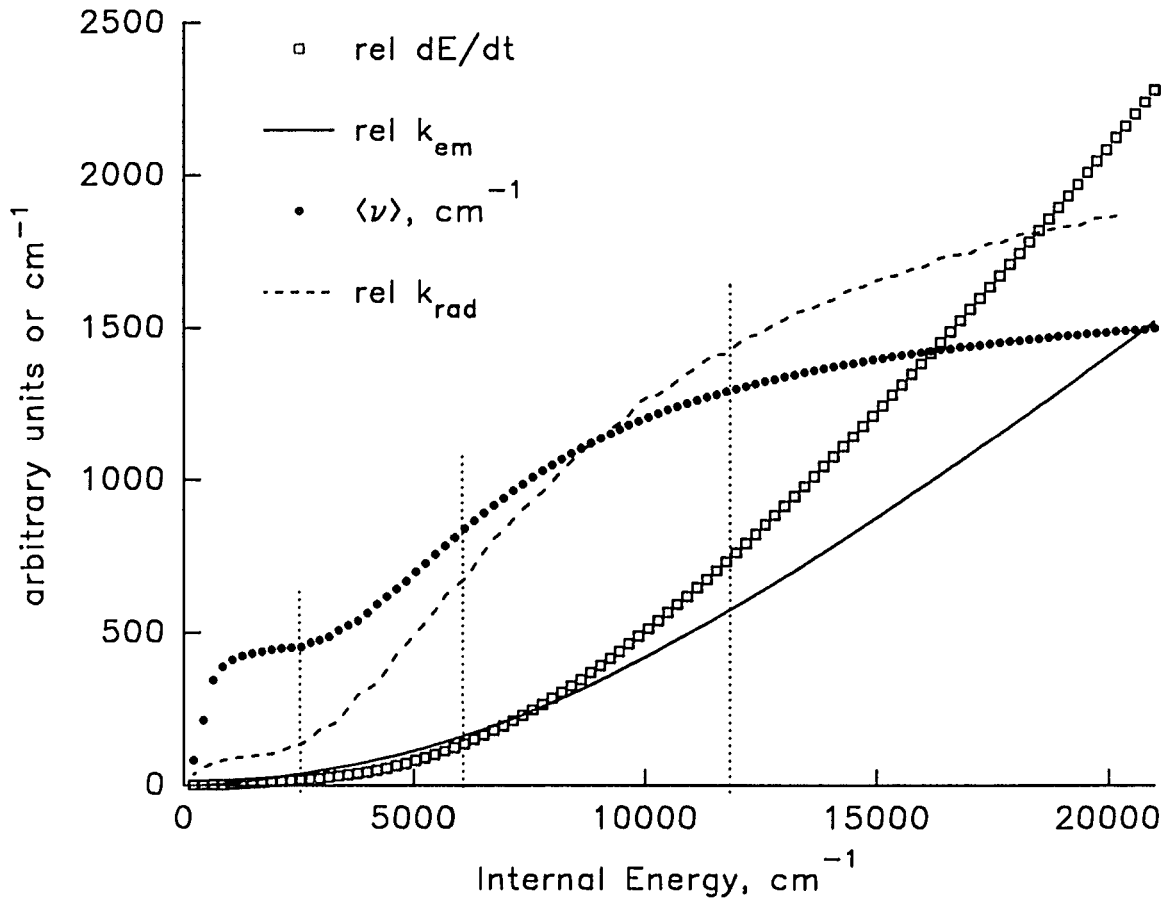

FIGURE 7.5: $Cr(CO)_5^-$ Relaxation Efficiency Graph

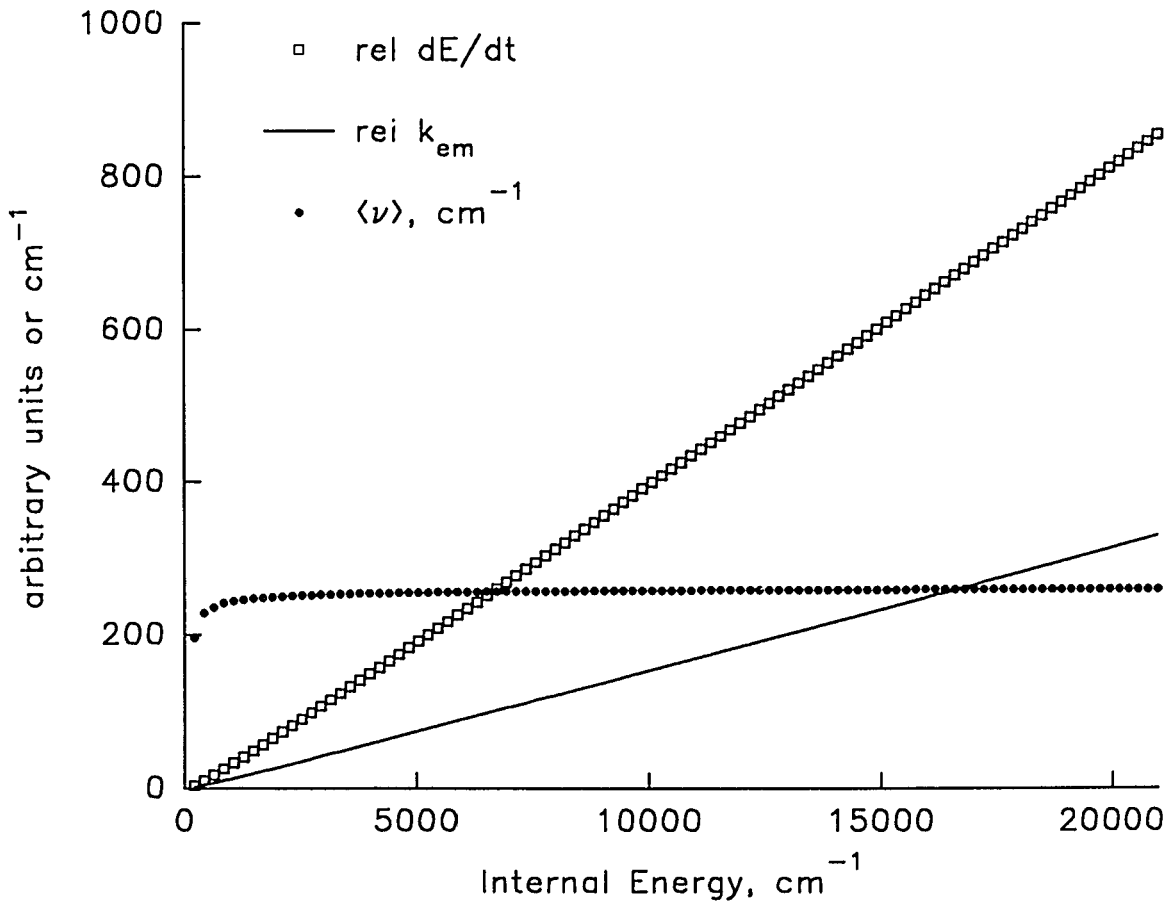

FIGURE 7.6: Al_{16}^- Relaxation Efficiency Graph

At this point it is worth making explicit the difference between the overall rate constant for spontaneous emission and the rate constant for radiative relaxation.[7.3] Since:

$$-\frac{dE}{dt} = k_{rad}(E)\cdot E = k_{em}(E)\cdot\langle\bar{\nu}(E)\rangle \qquad (7.9)$$

it is seen that the radiative rate constant describes the macroscopic energy disposal while the spontaneous emission rate constant accounts for the quantitized nature of energy disposal. Equation 7.9 can be rearranged so that an absolute value for k_{em} may be found from an experimental $k_{rad}(E)$ value:

$$k_{em}(E) = k_{rad}(E)\cdot\frac{E}{\langle\bar{\nu}(E)\rangle} \qquad (7.10)$$

This spontaneous emission rate constant may in turn be used to make an order-of-magnitude estimate of the transition dipole moment (using Equation 7.2) or the integrated cross section (using Equation 7.11, below) for the "average" transition:[7.9]

$$\int_{\nu}\sigma_i\,d\nu = \frac{k_{em,i}}{8\pi\bar{\nu}_i^2} \qquad (7.11)$$

For example, the average integrated cross section for a CO stretch in $Cr(CO)_5^-$ is on the order of 1×10^{-7} $cm^2\cdot s^{-1}$, depending somewhat on what energy region of the calculation. (This number was obtained from the two-pulse photodissociation measurement, using the emission fractions for the CO stretches and the average emitted frequency predicted from an 8855 cm^{-1} relaxation efficiency matrix.) Similarly, the "average" transition dipole moment for the vibrational modes of Al_{16}^- was found by adjusting the relative squared transition dipole

moment matrix elements (still assuming they are all equal) until the slope of the absolute dE/dt versus internal energy curve (analogous to Figure 7.6) equalled the experimentally-determined radiative rate constant. The transition dipole moment determined in this matter might be typical of a bulk aluminum phonon mode: it corresponds to one electron charge moving 2.29 Å, or about 80% of the nearest-neighbor distance for bulk aluminum.

Numerical Cascade Kinetic Models for $Cr(CO)_5^-$ Relaxation

As shown in Figure 5.1, the relaxation data obtained by two-pulse photodissociation experiments for $Cr(CO)_5^-$ cannot be adequately described by a single exponential fit. Instead, a numerical fit to a multi-step cascade relaxation model was used. Since $Cr(CO)_5^-$ must radiate about 5775 cm^{-1} (16.5 kcal/mol) of internal energy to relax below the one-photon threshold, three-step and higher cascade models were used. Briefly, the total experiment time is broken down into small, evenly-spaced increments, and the total internal energy difference to be traversed is divided into three or more equally-spaced steps (levels). A small probability (rate constant) is set for the step ("emission") from one energy level to the next within a single time increment. To simplify the fitting procedure, these rate constants are assumed to be proportional to the internal energy, so that only this proportionality constant must be iteratively determined. (This is approximately valid because these are spontaneous emission, and not radiative, rate constants as discussed above.) The rate of emission within each time step is then equal to the number of species in the emitting level times the emission rate constant for that step. If the time increments are small enough, the exponential and multiexponential curves representing the number of species in each level can be approximated by a series of straight-line emission rates. Best-fit results for three- through six-step cascade models are shown in Figures 7.6 through 7.9.

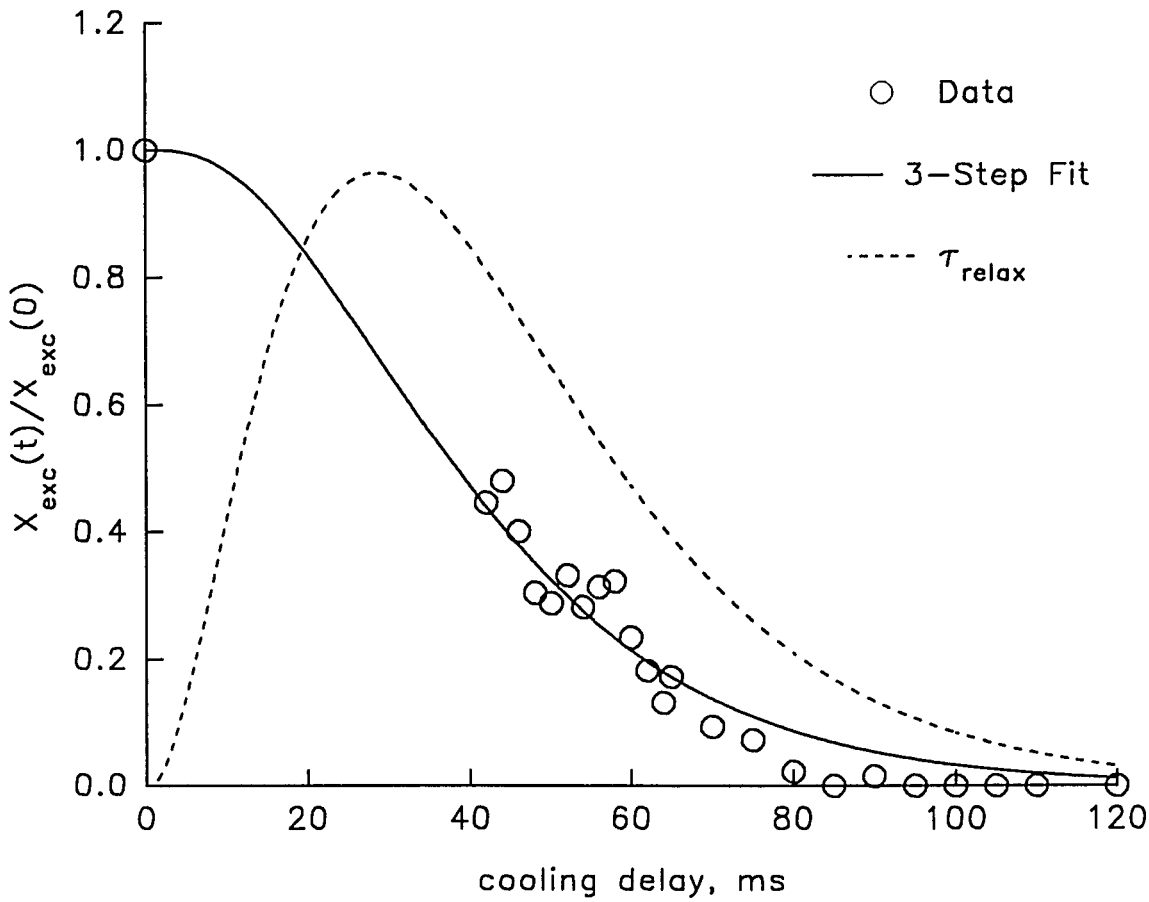

FIGURE 7.7: Three-Step Cascade Relaxation of $Cr(CO)_5^-$

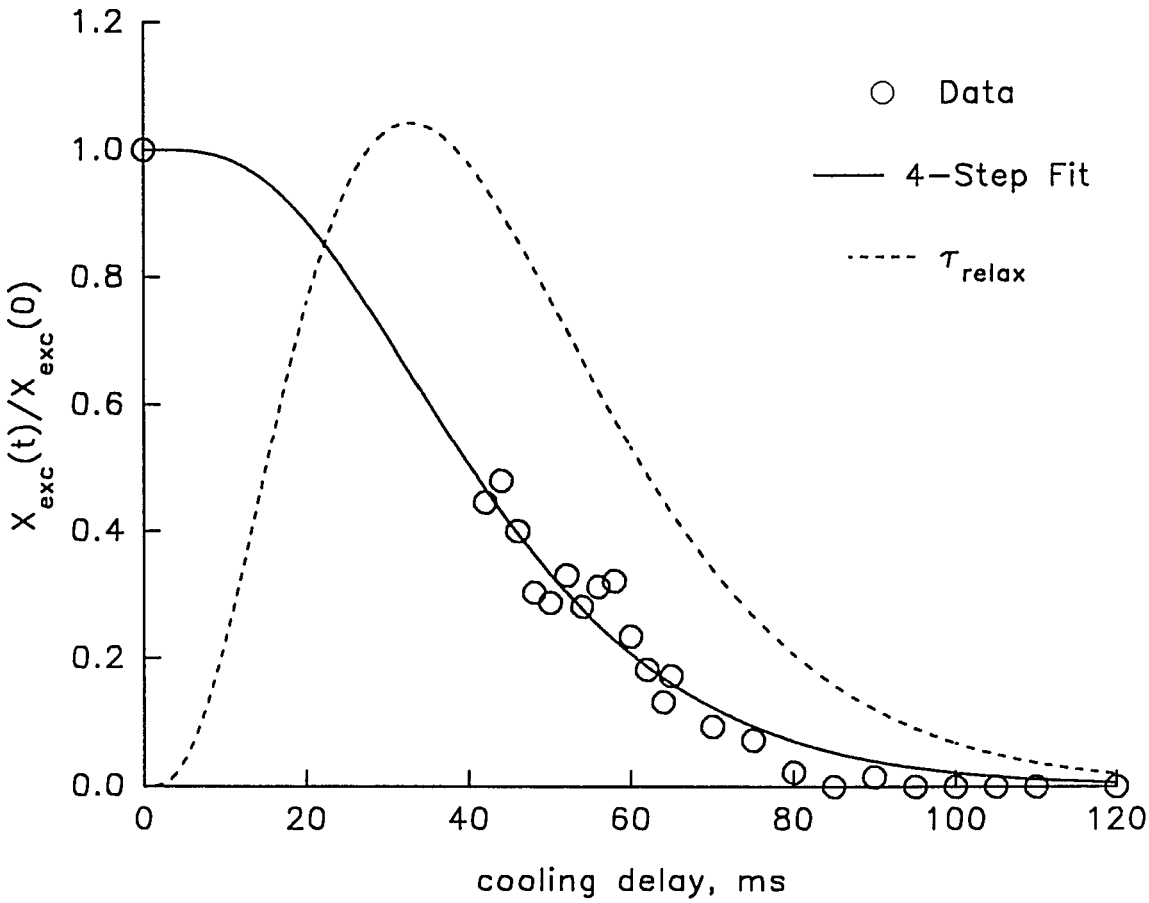

FIGURE 7.8: Four-Step Cascade Relaxation of $Cr(CO)_5^-$

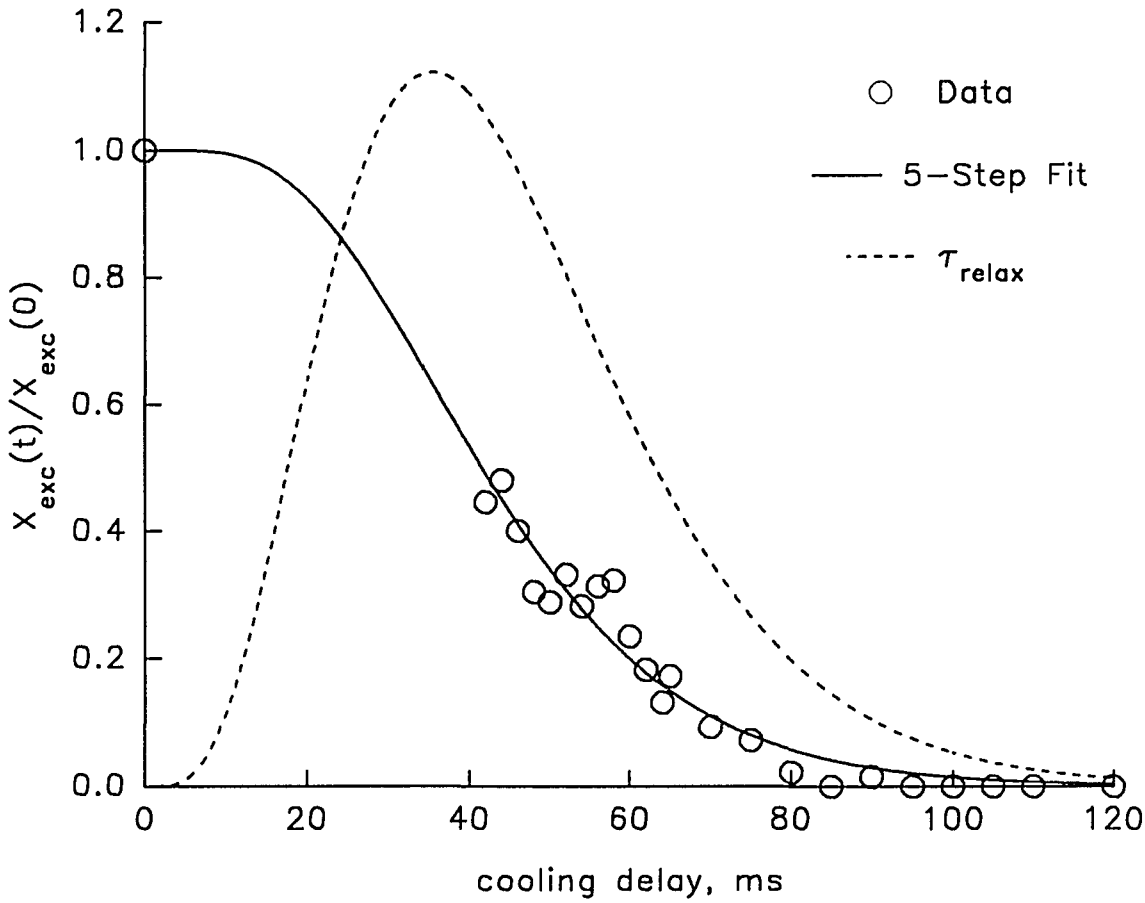

FIGURE 7.9: Five-Step Cascade Relaxation of $Cr(CO)_5^-$

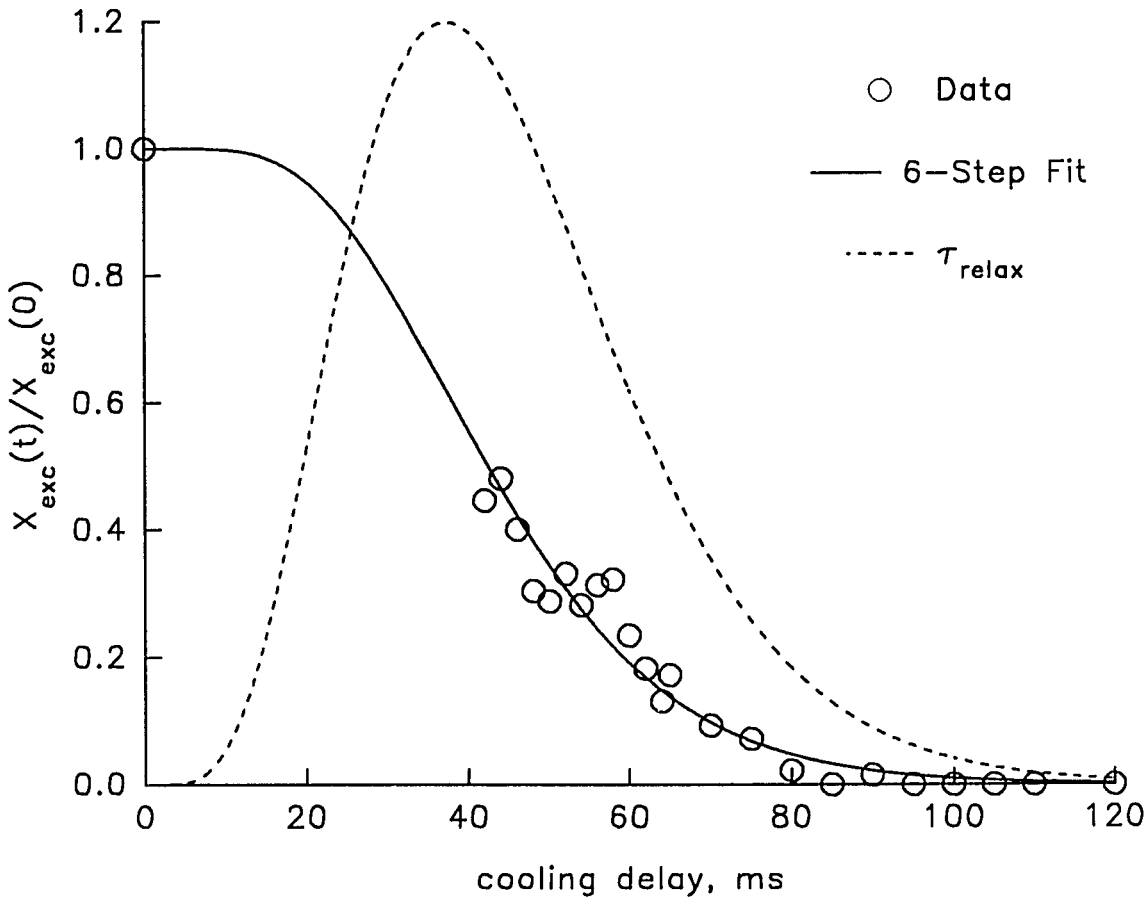

FIGURE 7.10: Six-Step Cascade Relaxation of $Cr(CO)_5^-$

In addition to the numerical fit, the time distribution with which the molecules cross the one-photon threshold, (also obtained from this fit as the difference in the number of species reaching the terminal level from one time increment to the next), is plotted as well. The mean of this distribution is designated τ_{relax}, the average relaxation time.

The best fit to the experimental data is obtained (by a small margin with respect to the four-step fit) by the five-step cascade model, which yields an approximate average emitted photon (step size) of 1155 cm^{-1}, consistent with the relaxation efficiency matrices shown above. The value of τ_{relax} determined for this fit is 44.7 ms, although this value is not very sensitive to the number of steps in the model. The average spontaneous emission rate constant found from all steps of this model (115 s^{-1}) may be converted to a radiative rate constant using a rearranged form of Equation 7.10. Assuming that E = 8872 cm^{-1} and $\langle\bar{\nu}\rangle$ = 1155 cm^{-1} in the middle of this energy range, the radiative rate constant found to be 15±2 s^{-1}, for which the error bars are set conservatively from the uncertainty in the energy. This agrees with the value determined in Chapter 5 from an eyeballed estimate of τ_{relax}, but with somewhat better precision. Very similar values are determined for k_{rad} from the four- and six-step models, since the emission rate constants for each model are adjusted to best fit the intrinsic 45 ms τ_{relax} value of the data. Therefore, the spontaneous emission rate constants for each small step of a six-step model will be much larger than those for each large step of a four-step model; each case yields approximately the same value of dE/dt.

Discussion of Experimental Considerations

It is important to the following discussion to recognize that the internal energy distributions of these anions are quite broad. Figures 7.11 and 7.12, below, plot the probability density functions for $Cr(CO)_5^-$ and Al_{16}^- calculated using the following equation and the state counts (g_j) obtained from the BS algorithm computations.

$$\frac{n_j}{N} = \frac{g_j e^{-E_j/kT}}{\sum_j g_j e^{-E_j/kT}} \qquad (7.12)$$

Also shown in each plot is the distribution corresponding to thermal plus one photon. It is encouraging that the means (first moments) of the thermal distributions are very near the average vibrational internal energy predicted from a quantum mechanical partition function. The Al_{16}^- distribution is significantly wider than the $Cr(CO)_5^-$ distribution because of the much larger density of states for the cluster. Figure 7.11 shows the dissociation and one-photon thresholds for $Cr(CO)_5^-$ as dotted vertical lines on the energy axis. This illustrates why non-integral photodissociation power dependencies are occasionally observed (for example, Al_9^-, Al_{12}^-, and Al_{21}^-—see Table 6.1), since a significant fraction of even a legitimately thermal ion population may possess internal energy already in excess of the one-photon threshold (depending of course on the dissociation energy).

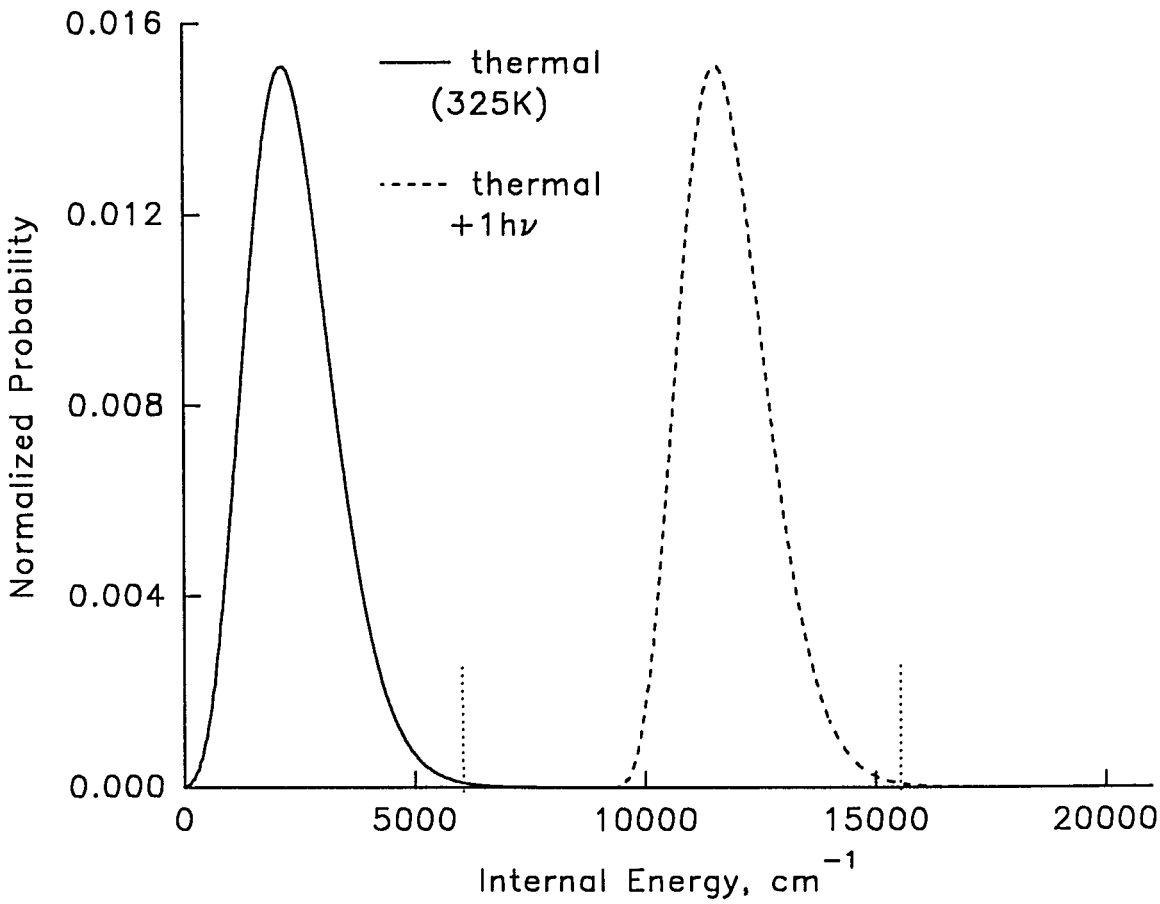

FIGURE 7.11: Vibrational Energy Distribution for $Cr(CO)_5^-$

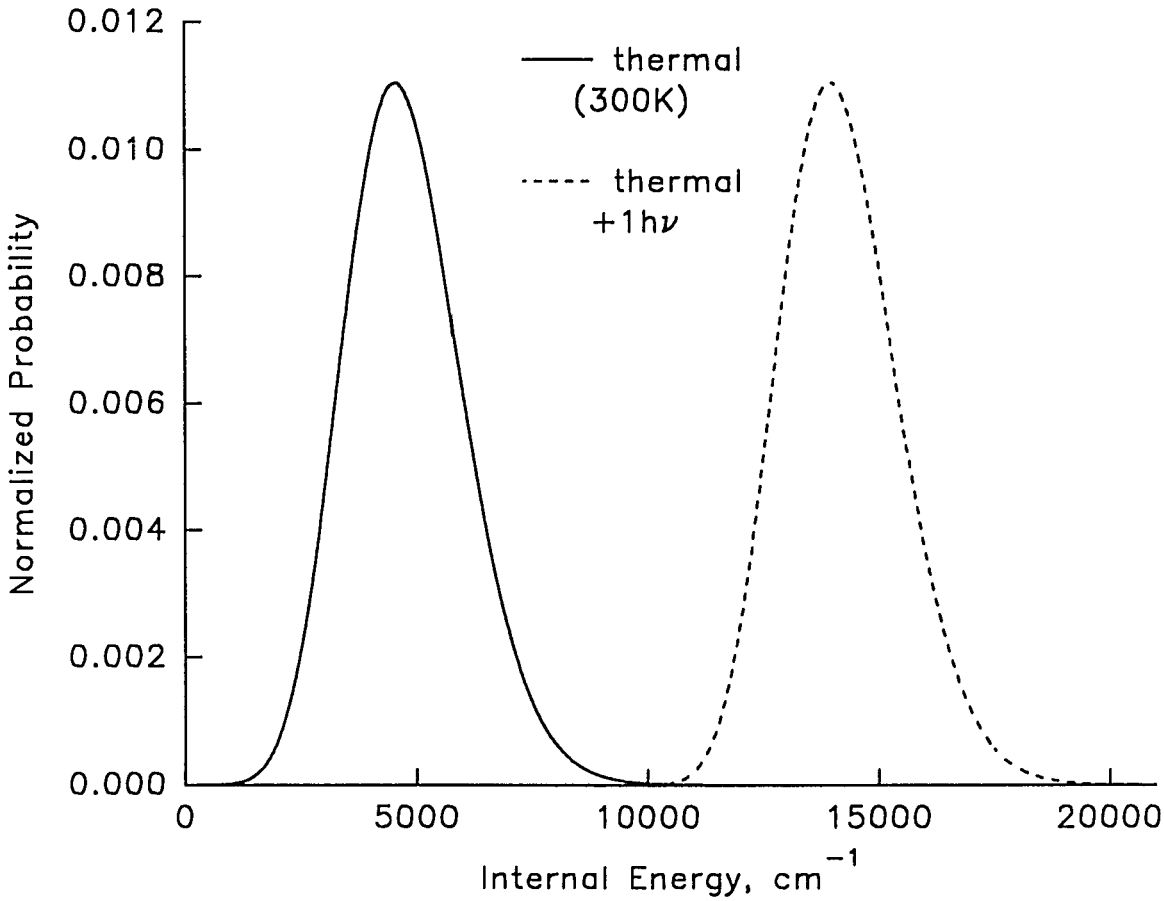

FIGURE 7.12: Vibrational Energy Distribution for Al_{16}^-

It is easy to see why the radiative rate constant determined from the two-pulse photodissociation experiment is greater than that determined from the competitive branching ratio experiment. The former measures the radiative rate constant over a narrower, higher-energy range (no response is observed below about 6000 cm^{-1}), while the oxidation branching ratio presumably is influenced by relatively small amounts of excess vibrational excitation. As seen in Figure 7.5, the radiative rate constant drops quite sharply in the vicinity of the one-photon threshold.

Last, recall that the exponential curves that were fit to the oxidation branching behavior of $Cr(CO)_5^-$ and Al_{16}^- were introduced in an *ad hoc* fashion, and there is not necessarily any reason to believe as a matter of first principles that the observed behavior is in fact exponential. There is a subtle difference between these branching ratio measurements that also needs to be discussed. The branching between loose and tight channels in the $Cr(CO)_5^-$ oxidation reactions is in fact competitive, while the "branching" observed in the aluminum cluster oxidation reactions is actually a sequential process. If the nascent Al_{n-4}^- cluster formed upon loss of 2 Al_2O molecules from the ion-molecule collision complex possesses residual internal energy in reasonable excess of the dissociation threshold, it will dissociate. The aluminum cluster relaxation experiments therefore represent *threshold* measurements, just like the two-pulse photodissociation experiments performed for $Cr(CO)_5^-$, and therefore ought to exhibit cascade kinetics. There is only one plausible explanation for the (approximately, at least) exponential behavior observed: the internal energy distribution of thermal Al_{16}^- is sufficiently broad as to "smear out" any threshold behavior.

Finally, it remains uncertain whether or not the relaxation curves obtained from the oxidation branching ratio of $Cr(CO)_5^-$ ought to be exponential. It can be stated, however, that this will only be rigorously true if the branching ratio is proportional to internal energy. To test this, an approximate RRK model[7.10] (Equation 7.13) was used to create the plot shown below in Figure 7.13

$$k(E) \approx \nu \left(\frac{E - E_0}{E} \right)^{n-1} \tag{7.13}$$

The parameters for this model, whose numerical values were chosen to fit data observed here and elsewhere, are the frequency factor ν (an approximate index of the "looseness" of the reaction, usually varying from 1 to 10), the activation energy E_0, and the number of vibrational degrees of freedom, n.

It is seen that the branching fraction for this model increases rapidly at moderate internal energies and then levels off; it is highly nonlinear. This is obviously because of the exponential dependence on the number of oscillators n. The relaxation measurements of Chapter 5 were fit to the branching ratio, which is not quite as nonlinear. Nevertheless, it is apparent from this model that the branching ratio experiment favors the lower energy region, because it is there that the response (change in branching ratio) varies most strongly with internal energy. Thus, the two-pulse photodissociation and oxidation branching ratio experiments yield complementary radiative relaxation rate constants: the former in the 1 eV region, and the latter in the near-thermal region.

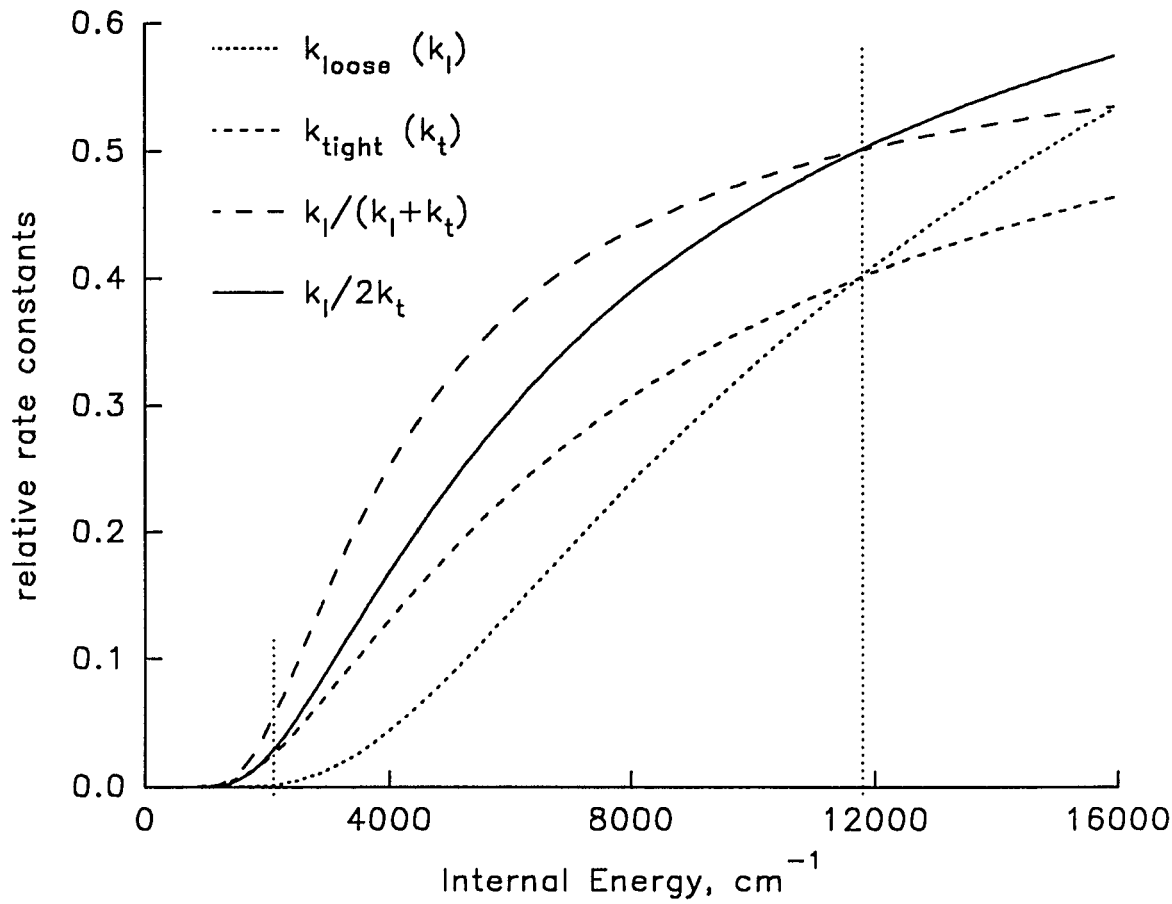

FIGURE 7.13: RRK Branching Model for the Oxidation of $Cr(CO)_5^-$

In conclusion, the use of photoexcited bimolecular reactions to obtain relaxation data has been demonstrated. The primary advantage of photoexcitation is the large, well-defined excess internal energy that may be deposited in an ion by the absorption of a photon. While further work needs to be done to obtain ion thermometric data, the branching ratio or initial rate of an ion-molecule reaction is often approximately proportional to internal energy, allowing a much more straightforward data interpretation than in the two-pulse photodissociation measurements. The modelling work discussed above, along with the experimental results of Chapters 5 and 6, illustrate the importance of high-frequency vibrational modes to the efficiency of radiative energy disposal from a vibrationally excited molecule. Species with high-frequency modes radiatively relax more rapidly than similar-sized species with only low-frequency modes. The latter also have a higher heat capacity than the former, as illustrated above in Figures 7.11 and 7.12. While the radiative relaxation model described in this Chapter considers in detail the contribution of each vibrational mode to the overall radiative relaxation behavior of an excited species, it is still quite approximate. For example, at present it neglects all effects of anharmonicity: on the frequency of the emitted photons, on the state count, on transition dipole moments, and on overtone transitions. It is encouraging, however, that useful results may still be obtained. A similar but reverse approach may soon find application to the prediction of radiative relaxation rates for large biomolecules, to estimate the "intrinsic" shifts expected in the dissociation thresholds for such large species.

APPENDIX A:

MATHEMATICAL DESCRIPTION OF SEQUENTIAL TWO-PHOTON DISSOCIATION: DISSOCIATED AND EXCITED FRACTIONS

Any polyatomic ion that requires the sequential absorption of two photons in order to dissociate can be prepared as a highly vibrationally excited species by the absorption of a single photon from a laser pulse. The laser pulses used here are sufficiently short that ion relaxation during a pulse is negligible, but are spatially and temporally diffuse enough that multiphoton processes also are unimportant: all absorptions are sequential. Also, internal conversion is much faster than subsequent absorption, so that absorption occurs only from the ground electronic state. Since absorption is a probabalistic process, it is experimentally impossible to prepare a population consisting entirely of ions that have absorbed exactly one photon. Some fraction of the ion population will not absorb any photons from the laser pulse, some will absorb one, and some will absorb two and therefore dissociate. The fragment ions also can absorb, although the relatively long and highly variable time scale for ion dissociation makes it extremely difficult to obtain an accurate mathematical description of absorption beyond the first two photons. As this Appendix is concerned with determining only those fractions of the ion population having absorbed zero, one, or two or more photons, it is not necessary to consider the time scale for dissociation as long as it is faster than subsequent ion isolation or detection procedures. This criterion is easily met by all predissociative ions except those with internal energies barely above the dissociation threshold. The purpose of this Appendix is to develop expressions for the fraction of the

total ion population that has dissociated (the "dissociated fraction," X_{diss}), the fraction of the undissociated ions having absorbed a photon (the "excited fraction," X_{exc}), and the relationship between these quantities.

Probabalistic Approach

Immediately after the laser pulse, ions in the trap can be classified by the number of photons each has absorbed (including photons absorbed by precursors of dissociated species). The fraction of the total population that has absorbed zero photons is denoted X_0, the fraction that has absorbed one, X_1, etc., so that the total ion population is given by:

$$(X_0 + X_1 + X_2 + \cdots + X_m)N = N\sum_{n=0}^{m} X_n \equiv N \qquad \text{(A.1)}$$

in which N is the total number of ions in the trap and m is the practical maximum number of photons to be absorbed. (Fractions above X_m are vanishingly small.) The average number of photons absorbed per ion, $\bar{n}$, is:

$$0 \cdot X_0 + 1 \cdot X_1 + 2X_2 + \cdots + mX_m = \sum_{n=0}^{m} nX_n \equiv \bar{n} \qquad \text{(A.2)}$$

This quantity will be directly proportional to the laser pulse energy if all absorption probabilities are equal and dissociation time scale effects can be ignored. As this is surely never true, it is more practical to define $\bar{n}$ as a parameter that *is* proportional to the pulse energy and to interpret it as the average number of photons that *would* be absorbed if all absorption cross sections were equal and all dissociations were instantaneous. (Justification for this definition of $\bar{n}$ will be given below.) The undissociated fraction X_{und} of the original ion population is simply $X_0 + X_1$, and the dissociated and excited fractions X_{diss} and X_{exc} (as defined above) are:

$$X_{diss} = 1 - X_{und} = 1 - X_0 - X_1 \qquad \text{(A.3.a)}$$

$$X_{exc} = \frac{X_1}{X_{und}} = \frac{X_1}{X_0 + X_1} \qquad \text{(A.3.b)}$$

The total number of undissociated ions in the trap, N', is equal to $X_{und}N$. The total number of excited ions is given as either X_1N or $X_{exc}N'$.

While X_{und} and X_{diss} are readily measured from the mass spectrum, determination of X_{exc} requires knowledge of X_1 individually (rather than just the sum of X_0 and X_1). Since an excited ion is indistinguishable (at ordinary resolving powers) from an unexcited ion of the same nominal mass it is therefore not possible to directly measure X_{exc}. However, it will be shown that X_{exc} can be estimated from a Poisson distribution if $\bar{n}$ is known for the experimental laser pulse energy. The use of the Poisson distribution can be justified with the following heuristic argument: First, divide the laser pulse into an arbitrary number of "time slices." Assume that each ion may absorb only one photon during each time slice, and that the probability of absorption within a time slice, p, is equal for all time slices. (The length of time allotted to each slice can be arbitrarily adjusted to ensure this.) If a single time slice is used to represent the laser pulse, then each ion may absorb only one photon during the pulse, and $\bar{n}$ will be equal to p. Note that the single-time-slice model does not allow for multiple absorption within a laser pulse and therefore is only appropriate if the extent of absorption is "small."

If two or more time slices are used to represent the laser pulse the problem becomes combinatorial. At this point it is necessary to make the additional assumption that the time slices represent *random trials*: in other words, the absorption cross section must be

independent of the number of photons previously absorbed by an ion (just as a coin has no "memory" of its previous toss). This assumption is not rigorously correct for the second photon to be absorbed, since the Frank-Condon factor for the second absorption will be altered by the presence of the excess internal energy from the first photon. However, for a sufficiently large polyatomic molecule this difference will be slight, and it is assumed that all of the polyatomic ions studied here are "sufficiently large" in this sense. For the third or higher photons to be absorbed this assumption is completely invalid since an ion that has absorbed two photons either is predissociative or has dissociated entirely. Fortunately, (as will be shown), X_{diss} is the only quantity required to calculate X_{exc}. Slow dissociation rates or differences in cross section for the higher absorptions simply shift the distribution of dissociated species comprising X_{diss}, but do not change its magnitude if the dissociation reactions are complete and their products quantitatively measured. (If photodetachment occurs to a significant extent the detached electrons must be wholly and unambiguously scavenged and detected.) That only this far less stringent assumption is required both simplifies the mathematics and justifies the use of the "practical" definition of $\bar{n}$.

The above model may be described with the well-known binomial distribution.[A.1] The laser pulse is divided into s random trials (time slices). For each trial, the probability of a "success" (absorption) is p and the probability of a failure is $q = (1 - p)$. The probability of observing x total successes given the parameters s and p is:

$$P_B(x;s,p) = \binom{s}{x} p^x q^{s-x} = \frac{s!}{x!(s-x)!} p^x q^{s-x} \qquad \text{(A.4)}$$

The mean of the binomial distribution is the product *ps*, which here is the average number of photons absorbed per ion, $\bar{n}$. Since $\bar{n}$ is constant for a given laser pulse energy, as the number of time slices used to model the pulse is arbitrarily increased the probability of absorption within each time slice must decrease proportionately. To accurately model the possibility of multiple absorption it is necessary to use as many time slices as possible, since absorption may occur at any instant within the laser pulse. If the laser pulse is divided into an infinite number of infinitesimally short time slices, p approaches zero and it can be shown that the binomial distribution asymptotically approaches a Poisson distribution described by the single parameter $\bar{n}$:[A.1]

$$P_P(x;\bar{n}) = \frac{\bar{n}^x}{x!} e^{-\bar{n}} \tag{A.5}$$

The following expressions are readily obtained by substitution:

$$X_0 \equiv P_P(0;\bar{n}) = e^{-\bar{n}} \tag{A.6.a}$$

$$X_1 \equiv P_P(1;\bar{n}) = \bar{n} e^{-\bar{n}} \tag{A.6.b}$$

The dissociated and excited fractions therefore can be given explicitly in terms of the average number of photons absorbed:

$$X_{diss} \equiv 1 - X_0 - X_1 = 1 - e^{-\bar{n}} - \bar{n} e^{-\bar{n}} \tag{A.7.a}$$

$$X_{exc} \equiv \frac{X_1}{X_0 + X_1} = \frac{\bar{n}}{1 + \bar{n}} \tag{A.7.b}$$

The difficulty lies in determining $\bar{n}$, since it cannot be measured directly. However, X_{diss} is both directly measurable (with the appropriate precautions mentioned above) and expressible

in terms of $\bar{n}$. While Equation A.7.a cannot be rearranged to give an analytical expression for $\bar{n}$ in terms of X_{diss}, a lookup table may be constructed that allows $\bar{n}$ (and therefore X_0, X_1, and X_{exc}) to be found to any desired level of precision for any experimental value of X_{diss}. Alternately, $\bar{n}$ may be found from a given X_{diss} by solving Equation A.7.a numerically; lookup tables are more practical because the calculations are much simpler and have been performed in advance. Such a table (with much coarser precision than is typically used) is shown below:

TABLE A.1: Poisson Distribution Calculation of X_{exc}

$\bar{n}$	X_0	X_1	X_{diss}	X_{exc}
0	1.0000	.0000	.0000	.0000
.1	.9048	.0905	.0047	.0909
.2	.8187	.1637	.0175	.1667
.3	.7408	.2222	.0369	.2308
.4	.6703	.2681	.0616	.2857
.5	.6065	.3033	.0902	.3333
.6	.5488	.3293	.1219	.3750
.7	.4966	.3476	.1558	.4118
.8	.4493	.3595	.1912	.4444
.9	.4066	.3659	.2275	.4737
1	.3679	.3679	.2642	.5000
1.1	.3329	.3662	.3010	.5238
1.2	.3012	.3614	.3374	.5455
1.3	.2725	.3543	.3732	.5652
1.4	.2466	.3452	.4082	.5833
1.5	.2231	.3347	.4422	.6000

To determine X_{exc} for a given X_{diss}, simply find the tabular value of X_{diss} that most nearly matches the experimental number and look up the corresponding value of X_{exc}. Greater precision may be obtained by interpolation or (more accurately) by recomputing the lookup

table with a finer $\bar{n}$ increment; however, it is probably unrealistic to claim X_{exc} to better than ±0.01, especially at lower values of X_{diss} where X_{exc} changes more rapidly. Finally, note that X_1 and therefore N_{exc} both are maximized when $\bar{n}$ equals unity, and that at this point X_{exc} equals one half.

Kinetic Approach

There is another approach that may be used to calculate X_{exc} given X_{diss}, based not on the Poisson probability distribution but instead on the integrated rate equations for a consecutive irreversible reactions kinetic model. In this method, the product kt of the rate constant for absorption and the irradiation time is proportional to the laser pulse energy; kt is analogous to ps (or $\bar{n}$) of the Poisson distribution method. Again, only a two-step process need be considered since the distribution of dissociated fragments is unimportant:

$$\mathrm{A} \xrightarrow{k_1} \mathrm{A}^{*} \xrightarrow{k_2} \mathrm{D} \qquad \text{(A.8)}$$

The rate constant for absorption at a given wavelength is simply the photon flux (intensity) times the absorption cross section: k (s^{-1}) = σ (cm^2) · I ($cm^{-2} \cdot s^{-1}$). Unlike the Poisson distribution approach, the kinetic method does not require that the first and second absorption cross sections be assumed equal, although different integrated rate expressions from those given below must be used if they are not. As discussed in the final section of this Appendix, only the product $\sigma_1 \cdot \sigma_2$ of the absorption cross sections for a two-photon dissociation process can be determined from the observed extent of dissociation X_{diss}; the relative values of σ_1 and σ_2 cannot be measured. However, since the cross sections are at least approximately the same (as discussed earlier), the equal rate constant case will be used. The integrated rate expressions for the species A(t), A*(t), and D(t) of Reaction A.8, given $k_1 = k_2 = k$, are well known[A.2] (compare to Equations A.6):

$$X_0 \equiv \frac{A(t)}{A_0} = e^{-kt} \qquad \text{(A.9.a)}$$

$$X_1 \equiv \frac{A^*(t)}{A_0} = kte^{-kt} \qquad \text{(A.9.b)}$$

Therefore, X_{diss} and X_{exc} are given (compare to Equations A.7):

$$X_{diss} \equiv 1 - X_0 - X_1 = 1 - e^{-kt} - kte^{-kt} \qquad \text{(A.10.a)}$$

$$X_{exc} \equiv \frac{X_1}{X_0 + X_1} = \frac{kt}{1 + kt} \qquad \text{(A.10.b)}$$

These results are completely equivalent to those of the Poisson distribution method. Again, the difficulty lies in calculating kt for a given experimental value of X_{diss}, since Equation A.10.a cannot be solved analytically for kt. This problem is an excellent demonstration of the relationship between probability and first-order decay processes, although further discussion of this phenomenon is beyond the scope of this Appendix. Finally, the results for the unequal rate constant case[A.2] are given below without derivation. These equations are indeterminate if k_1 equals k_2 and therefore cannot be compared directly to those of the equal rate constant case, above:

$$X_{diss} = \frac{k_2(1 - e^{-k_1 t}) - k_1(1 - e^{-k_2 t})}{k_2 - k_1} \qquad \text{(A.11.a)}$$

$$X_{exc} = \frac{k_1(e^{-k_1 t} - e^{-k_2 t})}{k_2 e^{-k_1 t} - k_1 e^{-k_2 t}} \qquad \text{(A.11.b)}$$

Ion-Cloud Hole Burning

The additional complication of "ion-cloud hole burning" arises if the spatial overlap between the ion cloud and the laser beam is poor. In this case it is assumed that the laser beam overlaps a fraction f of the ions and does not interact at all with the remaining $(1\text{-}f)$ of the ions; the "hole-burning fraction" f will be unity for perfect overlap. Quantities determined for the overlapped fraction are enclosed in curly brackets; for example, $\{X_{diss}\}$ represents the dissociated fraction of the irradiated ions while X_{diss} represents the dissociated fraction of all ions. The quantities $\{X_n\}$ again can be expressed in terms of $\{\bar{n}\}$:

$$\{X_n\} = \frac{\{\bar{n}\}^x}{x!} e^{-\{\bar{n}\}} \tag{A.12}$$

The following relationships exist between the overlapped and total fractions:

$$X_0 = (1 - f) + f\{X_0\} \tag{A.13.a}$$

$$X_n\,(n \geq 1) = f\{X_n\} \tag{A.13.b}$$

Note that there are *two* contributions to X_0: the unirradiated fraction of the ions plus the fraction of the irradiated ions that did not absorb any photons. Consequently, X_{exc} is only linearly related to $\{X_{exc}\}$ when X_{diss} is "small," unlike X_{diss} to $\{X_{diss}\}$:

$$X_{diss} \equiv 1 - X_0 - X_1 = 1 - (1 - f + f\{X_0\}) - f\{X_1\} = f\{X_{diss}\} \tag{A.14.a}$$

$$X_{exc} \equiv \frac{X_1}{X_0 + X_1} = \frac{f\{X_1\}}{(1 - f + f\{X_0\}) + f\{X_1\}} = \frac{f\{X_1\}}{1 - f\{X_{diss}\}} = \frac{f\{X_1\}}{1 - X_{diss}} \tag{A.14.b}$$

If X_{diss} is near zero, then $\{X_{exc}\}$ is approximately equal to $\{X_1\}$ and X_{exc} approaches $f\{X_{exc}\}$.

Measurement of f is not easy, but it can be done with a two-pulse photodissociation experiment (as described in the next section of this Appendix) for favorable cases in which ion relaxation is much slower than ion cloud redistribution. Once an estimate of f is obtained, a lookup table may be constructed to evaluate X_{exc} as a function of X_{diss} at that particular value of f. An example of such a table, for $f = 0.9$, is given below:

TABLE A.2: Poisson Distribution Calculation of X_{exc}, with Hole-Burning ($f = 0.9$)

$\{\bar{n}\}$	$\{X_0\}$	$\{X_1\}$	$\{X_{diss}\}$	X_{diss}	$\{X_{exc}\}$	X_{exc}
0	1.0000	.0000	.0000	.0000	.0000	.0000
.1	.9048	.0905	.0047	.0042	.0909	.0818
.2	.8187	.1637	.0175	.0158	.1667	.1497
.3	.7408	.2222	.0369	.0332	.2308	.2069
.4	.6703	.2681	.0616	.0554	.2857	.2555
.5	.6065	.3033	.0902	.0812	.3333	.2971
.6	.5488	.3293	.1219	.1097	.3750	.3329
.7	.4966	.3476	.1558	.1402	.4118	.3639
.8	.4493	.3595	.1912	.1721	.4444	.3908
.9	.4066	.3659	.2275	.2048	.4737	.4141
1	.3679	.3679	.2642	.2378	.5000	.4344
1.1	.3329	.3662	.3010	.2709	.5238	.4520
1.2	.3012	.3614	.3374	.3036	.5455	.4671
1.3	.2725	.3543	.3732	.3359	.5652	.4801
1.4	.2466	.3452	.4082	.3674	.5833	.4911
1.5	.2231	.3347	.4422	.3980	.6000	.5003

Note that all fractions for the irradiated ions are the same as the entries in Table A.1, as would be expected.

Two-Pulse Photodissociation Relaxation Measurements

This section describes the application and extension of the Poisson distribution method of excited fraction estimation to the two-pulse photodissociation relaxation measurements discussed in Chapter 5. Here, the Poisson distribution is used to predict the extent of excess dissociation due to excited-ion carryover as a function of the fraction of ions remaining above the one-photon threshold. Like before, a lookup table is constructed that allows this excited fraction to be determined from the experimentally observed dissociated fraction. In addition, the effect of ion-cloud hole burning on this experiment is considered for the limiting case in which the ion cloud has completely redistributed (randomized) itself by the second photodissociation pulse.

The excited fraction X_{exc} was previously defined as the fraction of the undissociated ion population X_{und} that had absorbed a photon, but the ultimate fate of this excess internal energy was not considered. A stricter definition is adopted here: only those ions remaining above the "one-photon threshold" (that have enough energy to dissociate upon absorption of a second photon) are considered part of X_{exc}. Also, the time dependence of X_{exc} is shown explicitly: the fraction of X_{und} that has absorbed a photon is designated $X_{exc}(0)$ and the fraction remaining above the one-photon threshold at time t is designated $X_{exc}(t)$. A prime is used to distinguish the second laser pulse from the first. For example, the dissociated fraction due to the first pulse, X_{diss}, is used to estimate $X_{exc}(0)$ and the dissociated fraction observed from the second pulse (after ejection of dissociated ions from the first pulse and a delay t), $X'_{diss}(t)$, is used to estimate $X_{exc}(t)$. Finally, recall that the quantities X_n refer to

the fractions of the ion population having absorbed n photons in the first pulse; the corresponding fractions for the second pulse are designated X'_n.

The possibility of imperfect overlap between the ion cloud and the laser beam will again be modeled with the single parameter f, the hole-burning fraction. It is assumed that the two photodissociation pulses represent random trials, so the probability that an individual ion belongs to the irradiated fraction in the second pulse is independent of its belonging to the irradiated fraction in the first pulse and is for both pulses equal to f. This approximation is most valid for second-pulse delays much longer than the period of the randomizing ion motion (the trapping oscillation for electromagnet geometries). Each ion will belong to one of four distinct subpopulations, as shown below:

TABLE A.3: Ion-Cloud Hole-Burning Fractions

Ion Irradiation Probabilities		Overlap in First Pulse	
		Yes = f	No = 1 - f
Overlap in Second Pulse	Yes = f	f^2	$(1-f)f$
	No = 1 - f	$f(1-f)$	$(1-f)^2$

These probabilities sum to unity for any valid nonzero value of f.

The dissociated fraction after the second laser pulse, X'_{diss}, consists of both one- and two-photon components, the former due to excited-ion carryover between the pulses. Only those ions irradiated in the second pulse (top row of entries in Table A.3) will contribute to $X'_{diss}(t)$. The fraction that was also irradiated in the first pulse, f^2, can make both one- and two-photon contributions, while the fraction that was irradiated solely in the second pulse,

$(1-f)f$, can make only a two-photon contribution. It is tempting at this point to try to account for these contributions individually and write:

$$\begin{aligned} X'_{diss}(t) &= f^2[\{X_{exc}(t)\}\cdot(1-\{X'_0\}) + (1-\{X_{exc}(t)\})\cdot(1-\{X'_0\}-\{X'_1\})] \\ &\quad + (1-f)f(1-\{X'_0\}-\{X'_1\}) \\ &= f^2[\{X_{exc}(t)\}\cdot\{X'_1\} + (1-\{X'_0\}-\{X'_1\})] \\ &\quad + (1-f)f(1-\{X'_0\}-\{X'_1\}) \\ &= f^2\{X_{exc}(t)\}\cdot\{X'_1\} + f(1-\{X'_0\}-\{X'_1\}) \end{aligned} \tag{A.15}$$

However, this equation ignores the ejection of dissociated ions after the first laser pulse and therefore is correct only for the limiting case that X_{diss} is "small" (compare Equation A.15 to Equation A.17, below, recalling from Equation A.14.b that X_{exc} approximates $f\{X_{exc}\}$ only as X_{diss} approaches zero.) The value of X'_{diss} expected for a given $X_{exc}(t)$ is more accurately expressed as:

$$\begin{aligned} X'_{diss}(t) &= X_{exc}(t)\cdot(1-X'_0) + (1-X_{exc}(t))\cdot(1-X'_0-X'_1) \\ &= X_{exc}(t)\cdot X'_1 + (1-X'_0-X'_1) \end{aligned} \tag{A.16}$$

Accounting for hole burning in the second pulse yields:

$$\begin{aligned} X'_{diss}(t) &= f[X_{exc}(t)\cdot(1-\{X'_0\}) + (1-X_{exc}(t))\cdot(1-\{X'_0\}-\{X'_1\})] \\ &= f[X_{exc}(t)\cdot\{X'_1\} + (1-\{X'_0\}-\{X'_1\})] \end{aligned} \tag{A.17}$$

If the relative pulse energy E_2/E_1 equals a, then $\{\bar{n}'\} = a\cdot\{\bar{n}\}$ and by substitution one obtains:

$$X'_{diss}(t) = f[X_{exc}(t)\cdot(1 - e^{-a\{\bar{n}\}}) + (1 - X_{exc}(t))\cdot(1 - e^{-a\{\bar{n}\}} - a\{\bar{n}\}e^{-a\{\bar{n}\}})]$$
$$= f[X_{exc}(t)\cdot a\{\bar{n}\}e^{-a\{\bar{n}\}} + (1 - e^{-a\{\bar{n}\}} - a\{\bar{n}\}e^{-a\{\bar{n}\}})] \quad \text{(A.18)}$$

The correction for relative pulse energy in Equation A.18 makes this treatment completely general in case it is experimentally impossible to generate laser pulses of equal energy. In each of Equations A.16 through A.18, the first equality divides the ion population into excited and unexcited terms, and the second equality is a simplified form. The former shows explicitly that dissociation requires the absorption of two or more photons for an unexcited ion but only one or more additional photons for an excited ion. The latter expresses the total dissociation as the fraction of all ions absorbing two or more photons plus the "excess dissociation:" the fraction of the excited ions absorbing only one.

While the excited fraction remaining after a delay t depends on the extent of ion relaxation, the initial excited fraction $X_{exc}(0)$ can be determined from X_{diss} and can then be used to compute $X'_{diss}(0)$:

$$X'_{diss}(0) = f\left[\frac{f\{X_1\}}{1 - X_{diss}}\cdot\{X'_1\} + (1 - \{X'_0\} - \{X'_1\})\right]$$
$$= \frac{f^2 a\{\bar{n}\}^2 e^{-(a+1)\{\bar{n}\}}}{1 - X_{diss}} + f(1 - e^{-a\{\bar{n}\}} - a\{\bar{n}\}e^{-a\{\bar{n}\}}) \quad \text{(A.19)}$$

In order to determine $X_{exc}(t)$ from an experimentally observed value of $X'_{diss}(t)$, a lookup table is constructed based on the parameters f, a, and X_{diss}. While a and X_{diss} can be measured directly, f can usually only be measured if ion relaxation is slow enough that the second photodissociation pulse can be introduced before the ions have relaxed significantly

but after they have redistributed (randomized) themselves. In such a favorable case the lookup table is iteratively recalculated as a function of f until the calculated value of $X'_{diss}(0)$ matches the experimental value. One such a table is shown below:

TABLE A.4: Two-Pulse Excited Fraction Determination
($f = 0.9$; $a = 1.0$; $X_{diss} = 0.2709$)

$\{\bar{n}\}$	$\{X_0\}$	$\{X_1\}$	$\{X_{diss}\}$	X_{diss}	$\{X_{exc}\}$	X_{exc}	$X'_{diss}(t)$
0	1.0000	.0000	.0000	.0000	.0000	.0000	.2709
.1	.9048	.0905	.0047	.0042	.0909	.0818	.2978
.2	.8187	.1637	.0175	.0158	.1667	.1497	.3202
.3	.7408	.2222	.0369	.0332	.2308	.2069	.3391
.4	.6703	.2681	.0616	.0554	.2857	.2555	.3551
.5	.6065	.3033	.0902	.0812	.3333	.2971	.3688
.6	.5488	.3293	.1219	.1097	.3750	.3329	.3806
.7	.4966	.3476	.1558	.1402	.4118	.3639	.3908
.8	.4493	.3595	.1912	.1721	.4444	.3908	.3996
.9	.4066	.3659	.2275	.2048	.4737	.4141	.4073
1	.3679	.3679	.2642	.2378	.5000	.4344	.4140
1.1	.3329	.3662	.3010	.2709	.5238	.4520	.4198
1.2	.3012	.3614	.3374	.3036	.5455	.4671	.4248
1.3	.2725	.3543	.3732	.3359	.5652	.4801	.4291
1.4	.2466	.3452	.4082	.3674	.5833	.4911	.4327
1.5	.2231	.3347	.4422	.3980	.6000	.5003	.4358

The calculated value of $X'_{diss}(0)$ expected for this experimental value of X_{diss} is 0.4198. To determine $X_{exc}(t)$, find the tabular value of $X'_{diss}(t)$ that most nearly matches the experimentally observed value and look up the corresponding value of X_{exc}. For example, if $X'_{diss}(t) = 0.391$, then $X_{exc}(t) \approx 0.364$, or about 80% of the value of $X_{exc}(0)$ (= 0.4520) determined from X_{diss}. The $X_{exc}(t)$ values are normalized to $X_{exc}(0)$ and plotted versus t, so

that the resulting graph represents the fraction of the originally-excited ions still above the one-photon threshold as a function of time, the most "natural" way to present the data.

Absorption Cross Sections

The laser-fluence dependence of X_{diss} will be derived from Equation A.11.a after its correction for ion-cloud hole burning:

$$X_{diss} = f\left[\frac{\{k_2\}(1 - e^{-\{k_1\}t}) - \{k_1\}(1 - e^{-\{k_2\}t})}{\{k_2\} - \{k_1\}}\right] \qquad \text{(A.20)}$$

Following a three-term expansion of the two exponential terms (each expansion valid to within five percent for $\{k_n\}t$ less than 0.58), Equation A.20 simplifies to:

$$X_{diss} \approx \frac{f\{k_1\}\{k_2\}t^2}{2} = \frac{f\,\sigma_1\sigma_2(\{I\}t)^2}{2} \qquad \text{(A.21)}$$

Recall that k (s^{-1}) = σ (cm^2) · I ($cm^{-2}{\cdot}s^{-1}$). Note that within this approximation X_{diss} is no longer indeterminate when the cross sections (rate constants) are equal. Simple propagation of error considerations can be used to show that Equation A.21 approximates X_{diss} within five percent if both $\{k_1\}t$ and $\{k_2\}t$ are less than 0.52, corresponding an upper limit for $\{X_{diss}\}$ of roughly fourteen percent—but potentially much lower if the cross sections differ substantially. The logarithmic form of Equation A.21 is:

$$\ln(X_{diss}) = \ln\left(\frac{f\,\sigma_1\sigma_2}{2}\right) + 2\ln(\{I\}t) \qquad \text{(A.22)}$$

A plot of $\ln(X_{diss})$ versus $\ln(\{I\}t)$ should have a slope of two (indicative of a two-photon dissociation) and an intercept of $\ln(f\sigma_1\sigma_2/2)$. As this intercept is a function of the *product* of the absorption cross sections, no conclusion can be drawn about the individual values of

σ_1 or σ_2. (Unlike the pulsed laser experiments described here, the ratio σ_1/σ_2—or σ_2/σ_1—may be measured kinetically with a continuous irradiation experiment.[A.3] While individual cross sections may be determined in this manner, the symmetry of this problem prevents identification of one of them as σ_1 and the other as σ_2.) Also, a non-integral photon dependence (slope) might be observed for some dissociations, even at small extents of dissociation. This usually means that the thermal distribution of ion internal energies allows an appreciable fraction of the ion population to dissociate upon absorbing only one photon. Such a situation is difficult to model reliably and is not treated here.

For practical cross section measurements in which the extent of dissociation may be larger than the above approximation allows, Equation A.22 is first used with data taken at lower laser fluences to verify that the dissociation indeed requires two photons. Dissociated fractions measured for higher laser fluences are then fit (typically using a lookup table) to a modified version of Equation A.10.a:

$$X_{diss} = f(1 - e^{-\sigma\{I\}t} - \sigma\{I\}te^{-\sigma\{I\}t}) \qquad \text{(A.23)}$$

The first and second absorption cross sections are assumed to be equal for convenience and in the absence of evidence to the contrary. The broad thermal internal energy distributions of typical "large" polyatomic ions blur the distinction between σ_1 and σ_2; indeed, a truly accurate description of the extent of dissociation demands that the cross sections be expressed as functions of internal energy. Practically, however, there is little to be gained from this, especially since an order-of-magnitude estimate is usually both all that is required to determine the nature of the transition and all that the data support.

APPENDIX B:

VIBRATIONAL MODE OCCUPATION CALCULATIONS USING THE EXTENDED BEYER-SWINEHART STATE-COUNTING ALGORITHM

The probability that a given vibrational mode of a polyatomic molecule will be occupied by one or more quanta is readily computed as a function of internal energy using the long-established Beyer-Swinehart state-counting algorithm.[B.1] Briefly, the user specifies the "grain" (energy resolution increment) and maximum energy for the calculation and estimates of all vibrational (or internal rotational) frequencies of the molecule. The maximum energy and the frequencies are each rounded to the nearest grain multiple and divided by the grain, yielding integral "reduced" parameters. The algorithm then adds separately the contribution of each reduced frequency to the total sum of states. The sum of vibrational energy states falling within each grain multiple is enumerated exactly if the roundoff error in the reduced frequencies is small, which can be accomplished with a small and judiciously chosen grain.[B.2] Only two numbers are required at each internal energy in order to calculate the occupation probability as a function of energy for a given vibrational mode: the sums of states calculated without and with the given mode. The occupation probability p_i for the ith degree of freedom is simply the fractional contribution made by that mode to the total sum of states N_{tot}:

$$p_i = \frac{N_{tot} - N_{\sim i}}{N_{tot}} = 1 - \frac{N_{\sim i}}{N_{tot}} \qquad \text{(B.1)}$$

where N_{-i} is the sum of states calculated without the ith mode. Of course, this treatment makes the usual (contradictory) assumptions that the vibrational modes are both strongly coupled (a statement of the ergodic hypothesis) *and* harmonic (its energy levels are uniformly spaced); while an activated ion is very likely ergodic, its vibrations clearly are not harmonic. The sum of states for a system of anharmonic oscillators can be calculated using the extended Beyer-Swinehart algorithm,[B.3] but only if the energy-level spacing is known as a function of the number of quanta n in each mode, which requires detailed knowledge of the corresponding potential surfaces. In general, the energy-level spacing for a stretching mode decreases with n, while that for a bending mode increases with n. Therefore, a calculation that assumes harmonic oscillators will slightly underestimate the occupation probability of a stretch and overestimate that of a bend.

In order to compute the average number of quanta in an occupied mode, the occupation probability of each individual energetically accessible *level* must be calculated using the extended Beyer-Swinehart algorithm, which adds separately the contribution of each level to the total sum of states. While the extended algorithm was developed and is normally used only to compute sums for the anharmonic degrees of freedom of a molecule, it is perfectly general and also may be used for harmonic vibrations. In fact, its use for harmonic modes avoids the accumulation of roundoff errors inherent in the use of reduced frequencies at large grains, allowing accurate calculations to be performed with larger grains for a substantial reduction in computational effort. The occupation probability $p_{i,n}$ for the nth level of the ith vibrational mode is again simply the fractional contribution made by that level to the total sum of states N_{tot}:

$$p_{i,n} = \frac{N_{tot} - N_{\sim(i,n)}}{N_{tot}} = 1 - \frac{N_{\sim(i,n)}}{N_{tot}} \qquad \text{(B.2)}$$

where $N_{\sim(i,n)}$ is the sum of states calculated without the nth level of the ith mode. The following identities are relevant to the ensuing discussion (m is the highest energetically accessible level and $p_{i,0}$ is the probability that the ith mode is *not* occupied):

$$p_i = \sum_{n=1}^{m} p_{i,n} \qquad \text{(B.3.a)}$$

$$1 \equiv p_{i,0} + p_i = \sum_{n=0}^{m} p_{i,n} \qquad \text{(B.3.b)}$$

$$\sum_{n=0}^{m} n p_{i,n} = \sum_{n=1}^{m} n p_{i,n} \qquad \text{(B.3.c)}$$

Once the occupation probability has been calculated for each energetically accessible level, the average number of quanta present when the mode is occupied is given by :

$$\langle n_{i,occ} \rangle = \frac{\sum_{n=1}^{m} n p_{i,n}}{\sum_{n=1}^{m} p_{i,n}} = \frac{\sum_{n=1}^{m} n p_{i,n}}{p_i} \qquad \text{(B.4)}$$

This weighted average accounts for the number of quanta present in the mode when each level is occupied: two quanta are present when the second level is occupied, and so on. The *overall* average occupation of a mode (including the possibility that the mode is unoccupied) is:

$$\langle n_i \rangle = p_i \langle n_{i,occ} \rangle \qquad \text{(B.5)}$$

It can be proven using the above identities that this expression is equivalent to the weighted average calculated with the probability $p_{i,0}$ that the mode is unoccupied, as is to be expected:

$$\langle n_i \rangle \equiv \frac{\sum_{n=0}^{m} n p_{i,n}}{\sum_{n=0}^{m} p_{i,n}} = \frac{\sum_{n=0}^{m} n p_{i,n}}{1} = p_i \left(\frac{\sum_{n=1}^{m} n p_{i,n}}{p_i} \right) = p_i \langle n_{i,occ} \rangle \qquad \text{(B.6)}$$

The following source code is for a program that calculates as a function of energy either the occupation probability or the average occupied level for all vibrational modes of a given molecule. While the original published description of this algorithm implies that the array of vibrational frequencies must be placed in ascending order, it is not in fact necessary to do so; the frequencies may be input in any order.

```
C     BSARRW  (BS algorithm ARRay calculation using Windows).
C
C  Windows program to calculate sums of internal energy states as a
C  function of energy, using the extended Beyer-Swinehart algorithm.
C  These sums are used to calculate either the occupation probability
C  or the average number of quanta (<n>) for each vibrational mode of a
C  given polyatomic molecule.  These data may then be used to model
C  radiative relaxation or other vibrational energy processes.
C
C  Input may be either interactive (Unit 1) or batch (Unit 3).  Input
C  files must be in the working directory at run time.  The required
C  batch input format is:
C
C    DIFREQS [+INT: The number of DIFFERENT (distinct) frequencies.]
C    DEGEN [Y|N: Y if some frequencies are degenerate.]
C    GRAIN [+REAL: Energy resolution of calculation, in cm-1.]
C    EMAX [+REAL: Maximum energy, cm-1.  EMAX/GRAIN must be <1000.]
C    DIFREQ(1),DEG(1)
C    DIFREQ(2),DEG(2)
C    ... [+/-REAL,+INT: Frequencies (cm-1), degeneracies iff DEGEN='Y']
C    DIFREQ(DIFREQS),DEG(DIFREQS)
C
C  A negative DIFREQ(I) indicates that only the occupation probability,
C  but not the average level, should be computed for the Ith mode.
C  This can be used for very low frequency modes (such as internal
C  rotors) to reduce the computation time.  It is rarely important to
C  calculate the average level for these modes because they will
C  contribute almost nothing to the overall radiative relaxation rate.
C
C  Any error in the batch input file will automatically return the
C  program to interactive input mode.
C
C  Output may include the input parameters (recommended if interactive
C  input is used) and is in array format:  The first column lists the
C  energies (grain multiples), the second column lists the overall sum
C  of states at each energy, and the third and subsequent columns list
C  either the occupation probability or average occupied level for each
C  mode at each energy.  Output will always be written to the terminal
C  (Window), from where it can be copied into the clipboard for pasting
C  into other applications, and it may optionally be written to an ASCII
C  (space-delimited) output file (Unit 2) as well.  Output files will be
C  written to the working directory.
C
C  This program was written, compiled, and linked using Microsoft
C  FORTRAN version 5.1.  Microsoft-specific FORTRAN statements
C  (including functions using nonstandard options) are labeled "!NOT77"
C  (itself a nonstandard construct).  Statements required for Microsoft
C  FORTRAN QuickWin are labelled !NOT77_W.  This program was tested with
C  Microsoft Windows 3.1 and will run under Windows 3.0 or later.
C
      INCLUDE 'FLIB.FI'                                          !NOT77_W
C
      PROGRAM BSARRW
C
      INCLUDE 'FLIB.FD'                                          !NOT77_W
      LOGICAL OK,EXISTS
      INTEGER DEG(54)
      INTEGER U,DIFREQS,GO,REDMAX,DOF,LEVELS,DL,D,REDLEV,ENERGY
      REAL DIFREQ(54),ABFREQ(54)
      REAL GRAIN,EMAX,DEFNEW,DEFDEG,OPS
      DOUBLE PRECISION TOT(0:54,0:1000)
```

```
      DOUBLE PRECISION ATOT(0:1000),LNUM(0:1000),LDEN(0:1000)
      RECORD /QWINFO/ WINFO                                    !NOT77_W
      CHARACTER*2 ORD(0:54)
      CHARACTER*24 DEFFILE
      CHARACTER*12 INFILE,OUTFILE
      CHARACTER*8 INNAME,OUTNAME
      CHARACTER*3 INEXT,OUTEXT
      CHARACTER IN,DEGEN,OUT,INCL,OVER,CHANGE,EXIT
      CHARACTER DEFIN,DEFDEGEN,DEFOUT,DEFINCL,DEFOVER
      COMMON U,DIFREQS,I,DIFREQ,EMAX,DEFNEW
C
C  Variable Naming Conventions
C
C    "RED-" = "REDuced" [parameter divided by grain]
C    "DEF-" = "Use DEFault?" [<Return> (=0 or space) accepts default]
C    "DI-" = "DIstinct"
C    "-S" = "number of..."
C    "L-" = "Level"
C    IN/OUT FILE NAME.EXT
C
C    Arrays dimensioned 0 or 1 to 54 are for FREQUENCIES
C    Arrays dimensioned 0 to 1000 are for ENERGY
C
C    D is an index for DEGENERACY
C    I,J are indices for FREQUENCIES
C    K,L are indices for LEVELS
C    N is an index for ENERGY
C
C      Labels:
C    Input section < 200            ASSIGNed have the form "n9"
C    200 <= Main section < 400      400 <= Output section < 1000
C    1000 <= Input format < 2000    2000 <= Output format < 3000
C
C  Initialization
C
      U=1
C..(Default input from Unit 1=interactive terminal)
C
      DIFREQS=0
      GRAIN=35.0
      EMAX=3500.0
      DATA (DEG(I),I=1,54) /54*1/
C
C..Set strings for ordinal numbers:
      DATA (ORD(I),I=0,3) /'th','st','nd','rd'/
      DO 10 I=4,54
        ORD(I)=ORD(0)
        IF (MOD(I,10) .LT. 4 .AND. MOD(I,100)/10 .NE. 1)
     + ORD(I)=ORD(MOD(I,10))
   10 CONTINUE
C
C..Set file defaults:
      IN='N'
      INNAME='   BSARR'
      INEXT='IN '
      OUT='Y'
      INCL='Y'
      OUTNAME='   BSARR'
      OUTEXT='OUT'
      OUTFILE=OUTNAME//'.'//OUTEXT
C
```

```
      OVER='N'
      DEGEN='N'
      DO 20 I=1,54
        DIFREQ(I)=0.0
   20 CONTINUE
C
C  Open Window and Maximize
C
      OPEN(1,BLOCKSIZE=0,FILE='USER',TITLE='BS')              !NOT77_W
      WINFO.TYPE=QWIN$MAX                                     !NOT77_W
      dummy=SETWSIZEQQ(1,WINFO)                               !NOT77_W
      dummy=ABOUTBOXQQ('BS Algorithm\r Version 1.0'C)         !NOT77_W
C
C  Batch/Interactive Input
C
   30 WRITE (1,1000) 'Use Batch Input File? [',IN,'] '
      READ (1,'(A1)') DEFIN
      IF (DEFIN .NE. ' ') THEN
        IF (DEFIN .EQ. 'Y' .OR. DEFIN .EQ. 'y') IN='Y'
      ENDIF
      IF (IN .EQ. 'Y') THEN
   35   WRITE (1,1000) 'Input File Name? [',INNAME//'.'//INEXT,'] '
        READ (1,'(A12)') DEFFILE
        CALL FNAMEVER(DEFFILE,INNAME,INEXT,OK)
        IF (.NOT. OK) GOTO 35
        INFILE=INNAME//'.'//INEXT
        INQUIRE(FILE=INFILE,EXIST=EXISTS)
        IF (.NOT. EXISTS) THEN
          WRITE (1,1100) 'File Does Not Exist.'
          GOTO 30
        ELSE
          OPEN(3,FILE=INFILE,MODE='READ')                     !NOT77
          U=3
        ENDIF
      ENDIF
C
   40 WRITE (1,*) ' '
   49 WRITE (1,1200) 'Number of Distinct Frequencies? [',DIFREQS,'] '
      ASSIGN 49 TO GO
   50 READ (U,'(F10.0)',ERR=900) DEFNEW
      IF (DEFNEW .GE. 1 .AND. DEFNEW .LE.54) THEN
        DIFREQS=DEFNEW
        IF (U .EQ. 3) WRITE (1,'(I2)') DIFREQS
      ELSEIF (DEFNEW .NE. 0.0 .OR. DIFREQS .EQ. 0) THEN
        IF (U .EQ. 3) WRITE (1,'(F8.0)') DEFNEW
        U=1
        WRITE (1,1300)
     + 'Please Enter between 1 and 54 Distinct Frequencies. '
        GOTO 50
      ENDIF
C
      WRITE (1,1000)
     + 'Are Some Frequencies Degenerate? [',DEGEN,'] '
      READ (U,'(A1)') DEFDEGEN
      IF (U .EQ. 3) WRITE (1,'(A1)') DEFDEGEN
      IF (DEFDEGEN .NE. ' ') THEN
        DEGEN='N'
        IF (DEFDEGEN .EQ. 'Y' .OR. DEFDEGEN .EQ. 'y') DEGEN='Y'
      ENDIF
C
   59 WRITE (1,1400) 'Grain (cm-1)? [',GRAIN,'] '
```

```
      ASSIGN 59 TO GO
      READ (U,'(F10.0)',ERR=900) DEFNEW
      IF (U .EQ. 3) WRITE (1,'(F8.1)') DEFNEW
      IF (DEFNEW .NE. 0.0) THEN
        IF (DEFNEW .LT. 0.0) THEN
          U=1
          WRITE (1,1100) 'Please Enter Positive Grain. '
          GOTO 59
        ELSE
          GRAIN=DEFNEW
        ENDIF
      ENDIF
C
   69 WRITE (1,1400) 'Maximum Energy (cm-1)? [',EMAX,'] '
      ASSIGN 69 TO GO
      READ (U,'(F10.0)',ERR=900) DEFNEW
      IF (U .EQ. 3) WRITE (1,'(F8.1)') DEFNEW
      IF (DEFNEW .NE. 0.0) EMAX=DEFNEW
      REDMAX=EMAX/GRAIN+0.5
      IF (EMAX .LT. GRAIN) THEN
        U=1
        WRITE (1,1100)
     + 'Maximum Energy Must Be Greater than Grain.  Please Reenter. '
        GOTO 59
      ELSEIF (REDMAX .GT. 1000) THEN
        U=1
        WRITE (1,1100)
     + 'Maximum Energy/Grain too Large.  Please Reenter. '
        GOTO 59
      ENDIF
      WRITE (1,*) ' '
C
      WRITE (1,1000) 'Write output to file? [',OUT,'] '
      READ (1,'(A1)') DEFOUT
      IF (DEFOUT .NE. ' ') THEN
        OUT='N'
        IF (DEFOUT .EQ. 'Y' .OR. DEFOUT .EQ. 'y') OUT='Y'
      ENDIF
      NOUT=1
      IF (OUT .EQ. 'Y') THEN
        WRITE (1,1000)
     + 'Include Input Parameters with Output? [',INCL,'] '
        READ (1,'(A1)') DEFINCL
        IF (DEFINCL .NE. ' ') THEN
          INCL='N'
          IF (DEFINCL .EQ. 'Y' .OR. DEFINCL .EQ. 'y') INCL='Y'
        ENDIF
   70   WRITE (1,1000) 'Output File Name? [',OUTNAME//'.'//OUTEXT,'] '
        READ (1,'(A24)') DEFFILE
        CALL FNAMEVER(DEFFILE,OUTNAME,OUTEXT,OK)
        IF (.NOT. OK) GOTO 70
        INQUIRE (FILE=OUTNAME//'.'//OUTEXT,EXIST=EXISTS)
        IF (EXISTS) THEN
          WRITE (1,1000)
     + 'File already exists.  OK to overwrite? [',OVER,'] '
          READ (1,'(A1)') DEFOVER
          IF (DEFOVER .NE. ' ') OVER=DEFOVER
          IF (OVER .EQ. 'Y' .OR. OVER .EQ. 'y') THEN
            OVER='Y'
          ELSE
            OVER='N'
```

```
            DEFFILE=OUTFILE
            CALL FNAMEVER(DEFFILE,OUTNAME,OUTEXT,OK)
            GOTO 70
          ENDIF
        ENDIF
        OUTFILE=OUTNAME//'.'//OUTEXT
        NOUT=2
      ENDIF
C
C  Read and Verify Frequencies and Degeneracies
C
      WRITE (1,*) ' '
      WRITE (1,1500)
     + 'Average Occupied Level Calculated for Positive Frequencies.',
     + 'Occupation Probability Calculated for Negative Frequencies.'
      IF (DEGEN .EQ. 'Y') THEN
        WRITE (1,1500) 'Use a Comma to Delimit the Values.',
     + 'A Null Value in Either Position Accepts that Default.'
        DO 80 I=1,DIFREQS
   79     WRITE (1,1600) I,ORD(I),DIFREQ(I),DEG(I)
          ASSIGN 79 TO GO
          READ (U,'(2F10.0)',ERR=900) DEFNEW,DEFDEG
          IF (MOD(DEFDEG,1.0) .EQ. 0.0 .AND. DEFDEG .GE. 0.0) THEN
            IF (DEFDEG .NE. 0.0) DEG(I)=DEFDEG
            IF (U .EQ. 3) WRITE (1,'(F8.1,'','',I3)') DEFNEW,DEG(I)
          ELSE
            IF (U .EQ. 3) WRITE (1,'(2F8.1)') DEFNEW,DEFDEG
            U=1
            WRITE (1,1100)
     + 'Please Enter a Positive, Integral Degeneracy.'
            GOTO 79
          ENDIF
          CALL FREQVER
   80   CONTINUE
C
      ELSE
        DO 90 I=1,DIFREQS
          DEG(I)=1
   89     WRITE (1,1700) I,ORD(I),DIFREQ(I)
          ASSIGN 89 TO GO
          READ (U,'(F10.0)',ERR=900) DEFNEW
          IF (U .EQ. 3) WRITE (1,'(F8.1)') DEFNEW
          CALL FREQVER
   90   CONTINUE
      ENDIF
C
      DO 100 I=1,DIFREQS
        ABFREQ(I)=ABS(DIFREQ(I))
  100 CONTINUE
C
C  Calculate Number of Atoms in Molecule
C
      WRITE (1,*) ' '
      DOF=0
      DO 110 I=1,DIFREQS
        DOF=DOF+DEG(I)
  110 CONTINUE
      IF (DOF .EQ. 1) THEN
        WRITE (1,1100) 'There is 1 Internal Degree of Freedom.'
        WRITE (1,1100) 'This Molecule is Diatomic'
      ELSE
```

```
        WRITE (1,1800) 'There are ',DOF,' Internal Degrees of Freedom.'
        IF (MOD(DOF,3) .EQ. 0) THEN
          WRITE (1,1800) 'This Molecule has ',(DOF+6)/3,' Atoms.'
        ELSE
          WRITE (1,1800)
     + 'Warning: ',DOF,' Degrees of Freedom not a Real Molecule.'
        ENDIF
      ENDIF
C
C  Estimate Length of Calculation
C
      OPS=0
      DO 140 I=0,DIFREQS
        OPS=OPS+REDMAX
        DO 130 J=1,DIFREQS
          LEVELS=EMAX/ABFREQ(J)
          DL=DEG(J)
          IF (J .EQ. I) DL=DEG(J)-1
          DO 120 D=1,DL
            OPS=OPS+LEVELS+(LEVELS+3)/2*REDMAX
  120     CONTINUE
  130   CONTINUE
        IF (I .NE. 0 .AND. DIFREQ(I) .GT. 0.0) THEN
          LEVELS=EMAX/ABFREQ(I)
          OPS=OPS+(LEVELS-1)*LEVELS
          OPS=OPS+(LEVELS+5)*(LEVELS+1)/2*REDMAX
        ELSEIF (I .NE. 0) THEN
          OPS=OPS+REDMAX
        ENDIF
  140 CONTINUE
      WRITE (1,'(2X,A,F8.2)')
     + 'Millions of Assignment Statements to be Executed: ',OPS/1000000
C
      IF (OUT .EQ. 'Y') WRITE (1,'(2X,A,A)')
     + 'Output Will Be Written to ',OUTFILE
C
      WRITE (1,*) ' '
      WRITE (1,1300) 'Any Changes? [N] '
      READ (1,'(A1)') CHANGE
      IF (CHANGE .EQ. 'Y' .OR. CHANGE .EQ. 'y') THEN
        U=1
        GOTO 40
C
C  Open Output File if Specified (Store Input Now in Case of Crash)
C
      ELSEIF (NOUT .EQ. 2) THEN
        OPEN (2,FILE=OUTFILE,MODE='WRITE')
        IF (INCL .EQ. 'Y') THEN
          WRITE (2,2000) DIFREQS,DEGEN,GRAIN,EMAX
          DO 150 I=1,DIFREQS
            IF (DEGEN .EQ. 'Y') THEN
              WRITE (2,'(2X,F8.1,'','',I3)') DIFREQ(I),DEG(I)
            ELSE
              WRITE (2,'(2X,F8.1)') DIFREQ(I)
            ENDIF
  150       CONTINUE
          WRITE (2,*) ' '
        ENDIF
      ENDIF
      WRITE (1,*) ' '
C
```

```
C  Initialize (Frequency,Energy) Data Matrix
C
      DO 170 I=0,DIFREQS
        TOT(I,0)=1.0D+0
        DO 160 N=1,REDMAX
          TOT(I,N)=0.0D+0
  160   CONTINUE
  170 CONTINUE
C
C  Calculate Partition Sums; Mode and Level Occupation
C
      DO 340 I=0,DIFREQS
C..I=0 for total sum; I=1 to DIFREQS for individual frequencies
C
        CALL YIELDQQ                                                !NOT77_W
C
C..Initialize temporary array for extended algorithm calculation
        ATOT(0)=1.0D+0
        DO 200 N=1,REDMAX
          ATOT(N)=0.0D+0
  200   CONTINUE
C
C..Calculate sum using all modes except one (Jth freq. = Ith freq.)
        DO 250 J=1,DIFREQS
          LEVELS=EMAX/ABFREQ(J)
          DL=DEG(J)
          IF (J .EQ. I) DL=DEG(J)-1
          DO 240 D=1,DL
            DO 220 K=1,LEVELS
C
C..Extended algorithm avoids accumulated grain multiple roundoff errors
              REDLEV=REAL(K)*ABFREQ(J)/GRAIN+0.5
              DO 210 N=0,REDMAX-REDLEV
                ATOT(REDLEV+N)=TOT(I,N)+ATOT(REDLEV+N)
  210         CONTINUE
  220       CONTINUE
C
C..Assign temporary array to total before continuing to next mode
            DO 230 N=0,REDMAX
              TOT(I,N)=ATOT(N)
  230       CONTINUE
  240     CONTINUE
C
C..Continue to next frequency
  250   CONTINUE
C
C..Calculate average occupied level if specified for Ith frequency
        IF (I .NE. 0 .AND. DIFREQ(I) .GT. 0.0) THEN
          LEVELS=EMAX/ABFREQ(I)
C
C..Reset numerator and denominator for weighted average calculation
          DO 260 N=0,REDMAX
            LNUM(N)=0.0D+0
            LDEN(N)=0.0D+0
  260     CONTINUE
C
C..Calculate occupation of the Kth level
          DO 310 K=1,LEVELS
            CALL YIELDQQ                                            !NOT77_W
C
C..Reset temporary sum to that for excluded mode
```

```
            DO 270 N=0,REDMAX
              ATOT(N)=TOT(I,N)
  270       CONTINUE
C
C..Calculate sum including all but the Kth level
            DO 290 L=1,LEVELS
              IF (L .NE. K) THEN
                REDLEV=REAL(L)*ABFREQ(I)/GRAIN+0.5
                DO 280 N=0,REDMAX-REDLEV
                  ATOT(REDLEV+N)=TOT(I,N)+ATOT(REDLEV+N)
  280           CONTINUE
              ENDIF
  290       CONTINUE
C
C..Add Kth term to both numerator and denominator of weighted average
            DO 300 N=0,REDMAX
              IF (TOT(0,N) .NE. 0.0) THEN
                LNUM(N)=LNUM(N)+REAL(K)*(1.0-ATOT(N)/TOT(0,N))
                LDEN(N)=LDEN(N)+1.0-ATOT(N)/TOT(0,N)
              ENDIF
  300       CONTINUE
C
C..Continue for next level
  310     CONTINUE
C
C..Evaluate weighted average for this frequency...
          DO 320 N=0,REDMAX
            IF (LDEN(N) .EQ. 0.0) LDEN(N)=1.0
            IF (TOT(0,N) .NE. 0.0)
     + TOT(I,N)=(1.0-TOT(I,N)/TOT(0,N))*LNUM(N)/LDEN(N)
  320     CONTINUE
C
C..Or evaluate occupation probability if specified for Ith frequency
        ELSEIF (I .NE. 0) THEN
          DO 330 N=0,REDMAX
            IF (TOT(0,N) .NE. 0.0) TOT(I,N)=1-TOT(I,N)/TOT(0,N)
  330     CONTINUE
        ENDIF
C
C..Indicate progress before continuing to next frequency
        WRITE (1,1900) I,DIFREQS
  340 CONTINUE
C
C  Output
C
      WRITE (1,*) ' '
C
C..Header
      DO 430 M=NOUT,1,-1
        WRITE (M,2100)
        DO 400 I=1,DIFREQS-1
          WRITE (M,2200) DIFREQ(I)
  400   CONTINUE
        WRITE (M,2300) DIFREQ(DIFREQS)
        WRITE (M,*) ' '
C
C..Tabular Data
        DO 420 N=0,REDMAX
          ENERGY=N*GRAIN
          WRITE (M,2400) ENERGY,TOT(0,N)
          DO 410 I=1,DIFREQS-1
```

```
            WRITE (M,2500) TOT(I,N)
  410     CONTINUE
          WRITE (M,2600) TOT(DIFREQS,N)
  420   CONTINUE
  430 CONTINUE
C
C  Exit Gracefully
C
      IF (NOUT .EQ. 2) THEN
        ENDFILE 2
        CLOSE (2)
      ENDIF
C
      WRITE (1,*) ' '
      WRITE (1,1300) 'Type ''Q'' when finished examining output.'
  440 WRITE (1,'(A,\)') '  '                                          !NOT77
      READ (1,'(A1)') EXIT
      IF (EXIT .NE. 'Q' .AND. EXIT .NE. 'q') GOTO 440
      GOTO 9999
C
C  Error Catching
C
  900 IF (U .EQ. 3) WRITE (1,*) 'ERR'
      U=1
      GOTO GO
C
C  Formats
C
 1000 FORMAT (2X,A,A,A,\)                                            !NOT77
 1100 FORMAT (2X,A)
 1200 FORMAT (2X,A,I2,A,\)                                           !NOT77
 1300 FORMAT (2X,A,\)                                                !NOT77
 1400 FORMAT (2X,A,F8.1,A,\)                                         !NOT77
 1500 FORMAT (2(2X,A,/))
 1600 FORMAT (2X,I3,A2,' Frequency (cm-1)/Degeneracy? [',
     +        F8.1,',',I3,'] ',\)                                    !NOT77
 1700 FORMAT (2X,I3,A2,' Frequency (cm-1)? [',F8.1,'] ',\)           !NOT77
 1800 FORMAT (2X,A,I5,A)
 1900 FORMAT (2X,I2,'/',I2)
C
 2000 FORMAT (5X,I3,/,7X,A1,/,2X,F8.1,/,2X,F8.1)
 2100 FORMAT (2X,'Energy',2X,'  Total  ',\)                          !NOT77
 2200 FORMAT (1X,F7.1,\)                                             !NOT77
 2300 FORMAT (1X,F7.1)
 2400 FORMAT (2X,I6,2X,E9.4,\)                                       !NOT77
 2500 FORMAT (1X,F7.4,\)                                             !NOT77
 2600 FORMAT (1X,F7.4,' ')
C
 9999 END
C
C
      SUBROUTINE FNAMEVER(VERFILE,FNAME,EXT,OK)
C
C  Subroutine for determining the validity of a DOS filename.
C
      LOGICAL OK
      INTEGER BEG,END,DOT,PER
      CHARACTER*79 VALID
      CHARACTER*24 VERFILE
      CHARACTER*8 FNAME
      CHARACTER*3 EXT
```

```
C
      OK=.TRUE.
      VALID='ABCDEFGHIJKLMNOPQRSTUVWXYZ'//'abcdefghijklmnopqrstuvwxyz'
     + //'1234567890'//'~`!@#$%^&()_-{}'''//'.'
C
C..Identify beginning and end of string
      BEG=VERIFY(VERFILE,' ')                                    !NOT77
      IF (BEG .EQ. 0) GOTO 9999
      END=VERIFY(VERFILE,' ',.TRUE.)                             !NOT77
C
C..Make sure there is only one (or no) dot in string
      DOT=INDEX(VERFILE,'.')
      PER=INDEX(VERFILE,'.',.TRUE.)                              !NOT77
      IF (DOT .NE. PER) GOTO 999
C
C..Check that substrings do not exceed maximum length
      IF (DOT .NE. 0) THEN
        IF (DOT-BEG .GT. 8 .OR. END-DOT .GT. 3) GOTO 999
      ELSE
        IF (END-BEG .GE. 8) GOTO 999
      ENDIF
C
C..Ensure all string characters are allowed for DOS filenames
      IF (VERIFY(VERFILE(BEG:END),VALID) .NE. 0) GOTO 999        !NOT77
C
C..Assign parsed substrings; accept defaults if indicated
      IF (DOT .NE. 0) THEN
        IF (DOT .NE. BEG .AND. DOT .NE. END) THEN
          FNAME='        '
          FNAME(9-DOT+BEG:8)=VERFILE(BEG:DOT-1)
          EXT=VERFILE(DOT+1:END)
        ELSEIF (DOT .EQ. BEG) THEN
          EXT=VERFILE(DOT+1:END)
        ELSEIF (DOT .EQ. END) THEN
          FNAME='        '
          FNAME(9-DOT+BEG:8)=VERFILE(BEG:END-1)
          EXT='   '
        ENDIF
      ELSE
        FNAME='        '
        FNAME(8-END+BEG:8)=VERFILE(BEG:END)
      ENDIF
      GOTO 9999
C
  999 WRITE (1,'(2X,A)') 'Please enter a valid DOS filename.'
      OK=.FALSE.
C
 9999 END
C
C
      SUBROUTINE FREQVER
C
C  Subroutine to verify the validity of an inputted frequency.
C
      INTEGER U,DIFREQS
      REAL DIFREQ(54)
      REAL EMAX,DEFNEW
      COMMON U,DIFREQS,I,DIFREQ,EMAX,DEFNEW
C
      IF (DEFNEW .NE. 0.0) THEN
        IF (DEFNEW .GT. EMAX) THEN
```

```
            U=1
            WRITE (1,'(2X,A,/,2X,A)')
     + 'This Frequency Will Never Contribute to the State Count.',
     + 'Please Enter a Smaller Value.'
            I=I-1
          ELSE
            DIFREQ(I)=DEFNEW
          ENDIF
        ELSE
C
          IF (DIFREQ(I) .EQ. 0.0) THEN
            U=1
            WRITE (1,'(2X,A)') 'Please Enter a Nonzero Frequency.'
            I=I-1
          ENDIF
        ENDIF
C
        END
```

REFERENCES

1.1. Marcus, Y. *Ion Solvation*; Wiley: New York, 1985.

1.2. McLafferty, F. W.; Tureček, F. *Interpretation of Mass Spectra*; University Science Books: Mill Valley, CA, 1993.

1.3. Cooks, R. G., ed. *Collision Spectroscopy*; Plenum: New York, 1978.

1.4. So, H. Y.; Dunbar, R. C. *J. Am. Chem. Soc.* **1988**, *110*, 3080.

1.5. Huang, F.-S.; Dunbar, R. C. *J. Am. Chem. Soc.* **1990**, *112*, 8167.

1.6. Smith, D.; Adams, N. G. In *Gas Phase Ion Chemistry*; Bowers, M. T., Ed.; Academic Press: New York, 1979, *v.* 1.

1.7. Dunbar, R. C. *J. Phys. Chem.* **1987**, *91*, 2801.

1.8. Dunbar, R. C. *J. Am. Chem. Soc.* **1971**, *93*, 4354.

1.9. Thorne, L. R.; Beauchamp, J. L. In *Gas Phase Ion Chemistry*; Bowers, M. T., Ed.; Academic Press: New York, 1984, *v.* 3.

1.10. Rosenfeld, R. N.; Jasinski, J. I.; Brauman, J. I. *J. Chem. Phys.* **1979**, *71*, 1030.

2.1. (a) Comisarow, M. B.; Marshall, A. G. *Chem. Phys. Lett.* **1974**, *25*, 282. (b) Comisarow, M. B.; Marshall, A. G. *Chem. Phys. Lett.* **1974**, *26*, 489.

2.2. Marshall, A. G.; Grosshans, P. B. *Anal. Chem.* **1991**, *63*, 215A.

2.3. Nibbering, N. M. M. *Mass Spectrom.* **1985**, *8*, 141.

2.4. McIver, R. T., Jr.; Fukuda, E. K. *Lect. Notes in Chem.* **1982**, *31*, 164.

2.5. Squires, R. R. *Chem. Rev.* **1987**, *87*, 623.

2.6. Beauchamp, J. L.; Dunbar, R. C. *J. Am. Chem. Soc.* **1970**, *92*, 1477.

2.7. Comisarow, M. B.; V. Grassi, V.; Parisod, G. *Chem. Phys. Lett.* **1978**, *57*, 413.

2.8. Wang, T.-C. L.; Marshall, A. G. *Int. J. Mass Spectrom. Ion Processes* **1986**, *68*, 287.

2.9. Ledford, E. B., Jr.; Ghaderi, S.; White, R. L.; Spencer, R. B.; Kulkarni, P. S.; Wilkins, C. L.; Gross, M. L. *Anal. Chem.* **1980**, *52*, 463.

2.10. Beauchamp, J. L. *Adv. Mass Spectrom.* **1974**, *6*, 717.

2.11. Huntress, W. T., Jr.; Simms, W. T. *Rev. Sci. Instr.* **1973**, *44*, 1274.

2.12. Ridge, D. P.; Beauchamp, J. L. *J. Chem. Phys.* **1969**, *51*, 470.

2.13. O'Malley, R. M.; Jennings, K. R. *Int. J. Mass Spectrom. Ion Phys.* **1969**, *2*, App 1.

2.14. Huang, Y.; Freiser, B. S. *J. Am. Chem. Soc.* **1990**, *112*, 5085.

2.15. Sharp, T. E.; Eyler, J. R.; Li, E. *Int. J. Mass Spectrom. Ion Phys.* **1972**, *9*, 421.

2.16. Dunbar, R. C.; Chen, J. H.; Hays, J. D. *Int. J. Mass Spectrom. Ion Processes* **1984**, *57*, 39.

2.17. van de Guchte, W. J.; van der Hart, W. J. *Int. J. Mass Spectrom. Ion Processes* **1990**, *95*, 317.

2.18. Hunter, R. L.; Sherman, M. G.; McIver, R. T., Jr. *Int. J. Mass Spectrom. Ion Phys.* **1983**, *50*, 259.

2.19. Grosshans, P. B.; Marshall, A. G. *Int. J. Mass Spectrom. Ion Processes* **1990**, *100*, 347. (Note that these authors define α to be a factor of two greater than the usual definition.)

2.20. Goode, G. C.; Jennings, K. R. *Adv. Mass Spectrom.* **1974**, *6*, 797.

2.21. Beauchamp, J. L.; Armstrong, J. T. *Rev. Sci. Instr.* **1969**, *40*, 123.

2.22. Johlman, C. L.; Wilkins, C. L. *J. Am. Chem. Soc.* **1985**, *107*, 327.

2.23. Allemann, M.; Kofel, P.; Kellerhals Hp.; Wanczek, K.-P. *Int. J. Mass Spectrom. Ion Processes* **1987**, *75*, 47.

2.24. Huang, S. K.; Rempel, D. L.; Gross, M. L. *Int. J. Mass Spectrom. Ion Processes* **1986**, *72*, 15.

2.25. van der Hart, W. J.; van de Guchte, W. J. *Int. J. Mass Spectrom. Ion Processes* **1988**, *82*, 17.

2.26. Kofel, P.; Allemann, M.; Kellerhals, Hp.; Wanczek, K.-P. *Int. J. Mass Spectrom. Ion Processes* **1986**, *74*, 1.

2.27. Laude, D. A., Jr.; Beu, S. C. *Anal. Chem.* **1989**, *61*, 2422 .

2.28. Hogan, J. D.; Laude, D. A., Jr., *Anal. Chem.* **1990**, *62*, 530.

2.29. Dunbar, R. C.; Weddle, G. H. *J. Phys. Chem.* **1988**, *92*, 5706.

2.30. Ijames, C. F.; Wilkins, C. L. *Anal. Chem.* **1990**, *62*, 1295.

2.31. Pignataro, S.; Foffani, A.; Grasso, F.; Cantone, B. *Z. Phys. Chem. (Frankfurt/Main)* **1965**, *47*, 106.

2.32. VanOrden, S. L.; Pope, R. M.; Buckner, S. W. *Org. Mass Spectrom.* **1991**, *26*, 1003.

2.33. Berberich, D. W.; Hail, M. E.; Johnson, J. V.; Yost, R. A. *Int. J. Mass Spectrom. Ion Processes* **1989**, *94*, 115.

2.34. Marshall, A. G.; Wang, T.-C. L.; Ricca, T. L. *J. Am. Chem. Soc.* **1985**, 107, 7893.

3.1. Dunbar, R. C. *J. Phys. Chem.* **1987**, *91*, 2801.

3.2. Simons, J. *J. Am. Chem. Soc.* **1981**, *103*, 3971.

3.3. Rosenfeld, R. N.; Jasinski, J. I.; Brauman, J. I. *J. Chem. Phys.* **1979**, *71*, 1030.

3.4. Wysocki, V. H.; Kenttämaa, H. I.; Cooks, R. G. *J. Phys. Chem.* **1988**, *92*, 6465.

3.5. McLafferty, F. W.; Tureček, F. *Interpretation of Mass Spectra*; University Science Books: Mill Valley, CA, 1993.

3.6. Benson, S. W. *Thermochemical Kinetics*; Wiley: New York, 1976.

3.7. Dunbar, R. C. *Mass Spectrom. Rev.* **1992**, *11*, 309.

4.1. (a) Poliakoff, M.; Weitz, E. *Adv. Organomet. Chem.* **1986**, *25*, 277. (b) Weiller, B. H.; Grant, E. R. In *Gas Phase Inorganic Chemistry*; Russell, D. H., Ed.; Plenum: New York, 1989.

4.2. (a) Eller, K.; Schwarz, H. *Chem. Rev.* **1991**, *91*, 1121. (b) Allison, J. *Prog. Inorg. Chem.* **1986**, *34*, 628. (c) Tecklenberg, R. E., Jr.; Bricker, D. L.; Russell, D. H. *Organometallics* **1988**, *7*, 2506.

4.3. Squires, R. R. *Chem. Rev.* **1987**, *87*, 623.

4.4. (a) Dunbar, R. C.; Ennever, J. F.; Fackler, J. P. *Inorg. Chem.* **1973**, *12*, 2734. (b) Richardson, J. H.; Stephenson, L. M.; Brauman, J. I. *J. Am. Chem. Soc.* **1974**, *96*, 3671. (c) Foster, R.; Beauchamp, J. L. *J. Am. Chem. Soc.* **1975**, *97*, 4808.

4.5. Geoffroy, G. L.; Wrighton, M. S. *Organometallic Photochemistry*; Academic Press: New York, 1979.

4.6. Parshall, G. W. *Homogeneous Catalysis*; Wiley-Interscience: New York, 1980.

4.7. (a) *Organic Synthesis Via Metal Carbonyls*; Wender, I.; Pino, P., Eds.; Wiley-Interscience: New York, 1968 (*v.* 1) and 1977 (*v.* 2). (b) Tsuji, J. *Organic Synthesis by Means of Transition Metal Complexes*; Springer-Verlag: New York, 1975.

4.8. (a) Sallans, L.; Lane, K. R.; Squires, R. R.; Freiser, B. S. *J. Am. Chem. Soc.* **1983**, *105*, 6352. (b) Sallans, L.; Lane, K. R.; Squires, R. R.; Freiser, B. S. *J. Am. Chem. Soc.* **1985**, *107*, 4379.

4.9. George, P. M.; Beauchamp, J. L. *J. Chem. Phys.* **1982**, *76*, 2959.

4.10. Cotton, F. A.; Hanson, E. B. In *Rearrangements in Excited and Ground States*; de Mayo, P., Ed.; Academic Press: New York, 1980, p. 379.

4.11. Michalopoulos, D. L.; Geusic, M. E.; Hansen, S. G.; Powers, D. E.; Smalley, R. E. *J. Phys. Chem.* **1982**, *86*, 3914.

4.12. Wronka, J.; Ridge, D. P. *J. Am. Chem. Soc.* **1984**, *106*, 67.

4.13. Leopold. D. G.; Lineberger, W. C. *J. Chem. Phys.* **1986**, *85*, 51.

4.14. *Collision Spectroscopy*; Cooks, R. G., Ed.; Plenum: New York, 1978.

5.1. Weitz, E. *J. Phys. Chem.* **1987**, *91*, 3945.

5.2. (a) Eller, K.; Schwarz, H. *Chem. Rev.* **1991**, *91*, 1121. (b) Allison, J. *Prog. Inorg. Chem.* **1986**, *34*, 628.

5.3. Squires, R. R. *Chem. Rev.* **1987**, *87*, 623.

5.4. Dunbar, R. C.; Hutchinson, B. B. *J. Am. Chem. Soc.* **1974**, *96*, 3816.

5.5 Sunderlin, L. S.; Wang, D.; Squires, R. R. *J. Am. Chem. Soc.* **1993**, *115*, 12060.

5.6. (a) McDonald, R. N.; Schell, P. L. *Organometallics* **1988**, *7*, 1806. (b) McDonald, R. N.; Schell, P. L. *Organometallics* **1988**, *7*, 1820.

5.7. Lane, K.; Sallans, L.; Squires, R. R. *J. Am. Chem. Soc.* **1984**, *106*, 2719.

5.8. Bricker, D. L.; Russell, D. H. *J. Am. Chem. Soc.* **1987**, *109*, 3910.

5.9. Hop, C. E. C. A.; McMahon, T. B. *J. Am. Chem. Soc.* **1992**, *114*, 1237.

5.10. Perutz, R. N.; Turner, J. J. *J. Am. Chem. Soc.* **1975**, *97*, 4791.

5.11. Freiser, B. S.; Beauchamp, J. L. *Chem. Phys. Lett.* **1975**, *35*, 35.

5.12. Orlowski, T. E.; Freiser, B. S.; Beauchamp. J. L. *Chem. Phys.* **1976**, *16*, 439.

5.13. (a) Dunbar, R. C.; Chen, J.-H. *J. Phys. Chem.* **1984**, *88*, 1401. (b) Asamoto, B.; Dunbar, R. C. *J. Phys. Chem.* **1987**, *91*, 2804. (c) Faulk, J. D.; Dunbar, R. C. *J. Phys. Chem.* **1989**, *93*, 7785.

5.14. (a) Dunbar, R. C. *J. Phys. Chem.* **1987**, *91*, 2801. (b) Dunbar, R. C. *J. Chem. Phys.* **1989**, *91*, 6080.

5.15. Faulk, J. D.; Dunbar, R. C. *J. Am. Chem. Soc.* **1992**, *114*, 8596.

5.16. Benson, S. W. *Thermochemical Kinetics*; Wiley: New York, 1976.

5.17. (a) Poliakoff, M.; Smith, K. P.; Turner, J. J.; Wilkinson, A. J. *J. Chem. Soc., Dalton Trans.* **1982**, 651. (b) Almond, M. J.; Crayston, J. A.; Downs, A. J.; Poliakoff, M.; Turner, J. J. *Inorg. Chem.* **1986**, *25*, 19.

5.18. Huang, F.-S.; Dunbar, R. C. *J. Am. Chem. Soc.* **1989**, *111*, 6497.

6.1. (a) Kroto, H. W.; Heath, R. J.; Smalley, R. E. *Nature* **1985**, *318*, 165. (b) Krätschmer, W.; Lamb, L. D.; Fostiropoulous, K.; Huffman, D. R. *Nature* **1990**, *347*, 354.

6.2. (a) Weltner, W., Jr.; van Zee, R. J. *Chem. Rev.* **1989**, *89*, 1713. (b) Parent, D. C.; Anderson, S. L. *Chem. Rev.* **1992**, *92*, 1541.

6.3. (a) Cox, D. M.; Trevor, D. J.; Whetten, R. L.; Kaldor, A. *J. Phys. Chem.* **1988**, *92*, 421. (b) Fuke, K.; Nonose, S.; Kikuchi, N.; Kaya, K. *Chem. Phys. Lett.* **1988**, *147*, 479.

6.4. (a) Hanley, L.; Ruatta, S. A.; Anderson, S. L. *J. Chem. Phys.* **1987**, *87*, 260. (b) Ruatta, S. A.; Anderson, S. L. *J. Chem. Phys.* **1988**, *89*, 273.

6.5. Jarrold, M. F.; Bower, J. E.; Kraus, J. S. *J. Chem. Phys.* **1987**, *86*, 3876.

6.6. Saunders, W. A.; Fayett, P.; Wöste, L. *Phys. Rev. A* **1989**, *39*, 4400.

6.7. Leuchtner, R. E.; Harms, A. C.; Castleman, A. W., Jr. *J. Chem. Phys.* **1991**, *94*, 1093.

6.8. Hettich, R. L. *J. Am. Chem. Soc.* **1989**, *111*, 8582.

6.9. Jarrold, M. F.; Bower, J. E. *J. Am. Chem. Soc.* **1988**, *110*, 6706.

6.10. (a) Ray, U.; Jarrold, M. F.; Bower, J. E.; Kraus, J. S. *J. Chem. Phys.* **1989**, *91*, 2912. (b) Ray, U.; Jarrold, M. F.; Bower, J. E.; Kraus, J. S. *Chem. Phys. Lett.* **1989**, *159*, 221.

6.11. Taylor, K. J.; Pettiette, C. L.; Craycraft, M. J.; Chesnovsky, O.; Smalley, R. E. *Chem. Phys. Lett.* **1988**, *152*, 347.

6.12. Ganteför, G.; Meiwes-Broer, K. H.; Lutz, H. O. *Phys. Rev. A* **1988**, *37*, 2716.

6.13. Lin, Y.; Nicol, G. R.; Ridge, D. P. In *Proceedings of the 40th ASMS Conference on Mass Spectrometry and Allied Topics*, Washington, D.C., 31 May-5 June 1992. p. 1743. American Society for Mass Spectrometry, 1992.

6.14. Batra, I. P.; Kleinman, L. *J. Electron Spectrosc. Relat. Phenom.* **1984**, *33*, 175.

6.15. Jarrold, M. F.; Bower, J. E. *J. Chem. Phys.* **1987**, *87*, 5728.

7.1. Dunbar, R. C. *Spectrochim. Acta. A* **1975**, *31*, 797.

7.2. Wilson, E. B., Jr.; Decius, J. C.; Cross, P. C. *Molecular Vibrations*; McGraw-Hill: New York, 1955.

7.3. Dunbar, R. C. *Mass Spectrom. Rev.* **1992**, *11*, 309.

7.4. Nakamoto, K. *Infrared and Raman Spectra of Inorganic and Coordination Compounds*; Wiley: New York, 1977.

7.5. Jarrold, M. F.; Bower, J. E. *J. Chem. Phys.* **1987**, *87*, 5728.

7.6. Kittel, K. P. *Introduction to Solid State Physics*; Wiley: New York, 1976.

7.7. Huber, K. P.; Herzberg, G. *Molecular Structure and Molecular Spectra IV: Constants of Diatomic Molecules*; Van Nostrand: New York, 1979.

7.8. Hop, C. E. C. A.; McMahon, T. B. *J. Am. Chem. Soc.* **1992**, *114*, 1237.

7.9. Svelto, O. *Principles of Lasers*; Plenum: New York, 1989.

7.10. Robinson, P. J.; Holbrook, K. A. *Unimolecular Reactions*; Wiley: New York, 1972.

A.1. Bevington, P. R.; Robinson, D. K. *Data Reduction and Error Analysis for the Physical Sciences*; McGraw-Hill: New York, 1992; Ch. 2.

A.2. Espenson, J. H. *Chemical Kinetics and Reaction Mechanisms*; McGraw-Hill: New York, 1981; Ch. 4.

A.3. van Velzen, P. N. T.; van der Hart, W. J. *Chem. Phys.* **1981**, *61*, 325.

B.1. Beyer, T.; Swinehart, D. F. *Commun. Assoc. Comput. Machin.* **1973**, *16*, 379.

B.2. Stein, S. E.; Rabinovitch, B. S. *Chem. Phys. Lett.* **1977**, *49*, 183.

B.3. Stein, S. E.; Rabinovitch, B. S. *J. Chem. Phys.* **1973**, *58*, 2438.